4-16-2019

# Design and Performance Evaluation of Linear and Axial-Flux Magnetic Gears

Mojtaba Bahrami Kouhshahi
*Portland State University*

# Design and Performance Evaluation of Linear and Axial-Flux Magnetic Gears

by

Mojtaba Bahrami Kouhshahi

A dissertation submitted in partial fulfillment of the
requirements for the degree of

Doctor of Philosophy
in
Electrical and Computer Engineering

Dissertation Committee:
Jonathan Bird, Chair
Robert Bass
Martin Siderius
Hormoz Zareh

Portland State University
2019

## Abstract

The conversion from low speed to high speed and vice versa in various forms, including rotary and linear motion, is a requirement for a wide range of applications. For example, wind power generation requires a conversion of low speed rotation of turbine blades to high speed generator rotation, and ocean wave power generation is achievable by conversion of low speed linear motion to either high speed rotation or high speed linear motion. Mechanical gearboxes, hydraulic and pneumatic actuators are commonly used to achieve these conversions. However, these systems suffer from reliability issues, high maintenance requirements, noise, and lack of overload protection.

As an alternative, electromagnetic actuators overcome most of the issues related to the mechanical, hydraulic and pneumatic mechanisms. However, magnetic shear stress is constraint by current density and magnetic saturation. Recently, magnetic gearboxes have been proposed, which rely only on magnetic loading. They provide speed and force conversion like their mechanical counterparts, but without thermal constraints (current density limits). Unlike mechanical gears, magnetic gear contact-less operation enables it to operate without lubrication and with low noise, and higher efficiency. Its reliance on magnetic loading also provides overload protection.

This dissertation focuses on investigating two new types of magnetic gears; first a magnetically-geared lead screw is proposed, which converts a low speed linear motion to a high speed rotary motion. The proposed actuator is a combination of two previously proposed actuators, the linear magnetic gear and the magnetic lead screw. Unlike these two topologies, the translator part of the proposed magnetically geared lead screw is made

entirely of low-cost ferromagnetic steel. Therefore, the translator stroke length can be long without requiring more magnet material.

In the second part of this dissertation, an axial flux magnetic gear is proposed that has an integrated outer stator. This axial flux magnetically-geared motor is unique in that the stator shares the high-speed rotor with the magnetic gear, so there is no need for a separate rotor. The high speed and low speed rotors use a flux-focusing typology. The stator is mounted outside the axial flux magnetic gear. This makes the design mechanically less complex. It also enables the stator to be cooled more easily.

In the last part of this dissertation, analytical-based models are proposed for a linear permanent magnet coupling and magnetic lead screw. These models help to find the upper bound of the similar devices, which require a scaling analysis. Numerical methods like finite element analysis are accurate and effective enough for modeling various electromechanical and electromagnetic devices. However, these simulations are usually computationally expensive; they require a considerable amount of memory and time, especially when considering 3D finite element simulation. The proposed analytical models offer exact field solution while significantly reducing the computational time.

Detailed analysis of two magnetic gears is given under their corresponding chapters. Preliminary experimental results are also provided. The analytical-based model is presented and verified by FEA results. A summary of research contributions and future works is outlined.

## Acknowledgments

More than four years ago, I started my professional graduate life journey. Beside my always supportive family, I have met many people who assisted me to finish this mission. Having a knowledgeable, patient and supportive leader like Dr. Jonathan Bird, I was able to defeat many obstacles in my way and add to my knowledge through learning, experimenting and inventing. For these and for countless other non-academic lessons that I learned from him I want to thank my advisor Dr. Bird. I cannot express how much I enjoyed working with him. I would also like to thank Dr. Wesley Williams for his guidance and support. I must thank Dr. Bass, Dr. Siderius and Dr. Zareh for accepting to be members of my advisory committee and taking their precious time to review my work. Their useful remarks helped me to refine my thesis.

In the last year of my journey, I met my beautiful and lovely wife, Sahel. Her endless patient and understanding presence in my life throughout that challenging and very stressful year helped me to finish all projects and at the same time enjoy living my life with her with the hope of an even brighter future. I must thank my supportive parents and siblings for all their positive energy from thousands of miles away. It was for their support that I was able to start this journey.

I want to thank my current lab mates and friends Hossein Baninajar, Danielle Vournas, David Ho and Emrad Hossain for all their help for assembling and testing work. I enjoyed working with them. I should also thank my former lab mates Kiran Uppalapati, Kang Li, Debarupa Som, Joshua Kadel, and Joel Pitchard. They have always been willing to help. Thanks for their kind support and help. I should also thank Vedanadam Acharya, Matthew Calvin, Sina Modaresahmadi for their support on my work.

Having wonderful friends is a priceless gift for anyone. I am grateful for having this fantastic gift throughout my whole life. I want to specially thank my kind and supportive friend Khalegh Mozafari for his always-valuable advice and support. I should also thank my friends in Charlotte, NC and my friends in Portland, OR for making my life full of happy moments.

Finally yet importantly, I would like to thank the National Science Foundation and North Carolina Coastal Studies Institute for their financial support. I want to also thank JMAG for the use of their software.

Table of Contents


Abstract ..... i

Acknowledgments ..... iii

List of Tables ..... viii

List of Figures ..... ix

List of Abbreviations ..... xv

List of Symbols ..... xvi

1 Chapter 1: Introduction ..... 1

1.1 Motivation ..... 1

1.2 Literature Review ..... 3

1.2.1 Hydraulic Actuators ..... 3

1.2.2 Pneumatic Actuators ..... 4

1.2.3 Electromechanical Linear Actuators ..... 5

1.2.4 Electromagnetic Linear Actuators (Direct Drive Actuators) ..... 6

1.2.5 Magnetic Gears ..... 13

1.2.5.1 Linear Magnetic Gears ..... 16

1.2.5.2 Magnetic Lead Screw ..... 20

1.2.6 Summary ..... 24

1.2.7 Problem Statement ..... 25

2 Chapter 2: Magnetically Geared Lead Screw ..... 26

2.1 Introduction ..... 26

2.2 Proof of Concept Design ..... 26

2.2.1 Structural Characteristics ..... 26

2.2.2 Operational Characteristics ..... 29

2.2.2.1 Translator Case ..... 30

2.2.2.2 Oscillator Case ..... 31

2.2.2.3 Power Conversion ..... 32

2.2.3 Analysis and Results ..... 33

2.3 Comparative Design ..... 35

2.3.1 Design Analysis ..... 36

2.3.2 Operational Analysis ..... 39

2.4 Prototype Design ..... 42

2.4.1 Design Analysis ........ 42
2.4.2 Simulation Results ........ 46
2.4.3 Experimental Results ........ 47
2.4.4 Lead Angle ........ 49
2.5 MGLS without Translator Skewing ........ 51
2.5.1 Design Analysis ........ 51
2.5.2 FEA Analysis ........ 53
2.5.3 Experimental Verification ........ 54
2.5.4 Conclusion ........ 58
3 Chapter 3: Axial Flux-Focusing Magnetically Geared Motor ........ 59
3.1 Introduction ........ 59
3.2 Brief Review of Axial Flux Magnetically Geared Motors ........ 60
3.3 Axial Flux-Focusing Magnetic Gear ........ 67
3.3.1 Field Analysis ........ 69
3.3.2 Performance Analysis ........ 70
3.3.3 Experimental Results ........ 72
3.4 Axial Flux-Focusing Magnetically Geared Motor ........ 75
3.4.1 Stator Slot Design ........ 76
3.4.2 Fractional Slot Winding Design for 45 Slot Stator ........ 79
3.4.3 Field Analysis ........ 81
3.4.4 Torque Analysis ........ 83
3.4.5 Experimental Results ........ 85
3.4.6 Conclusion ........ 88
4 Chapter 4: Analytical Model of a Linear Coupling and a Magnetic Lead Screw ........ 90
4.1 Introduction ........ 90
4.2 Analytical-Based Model for Halbach Linear Permanent Magnet Coupling ........ 91
4.2.1 Magnetic Flux Density for Linear Permanent Magnet Coupling ........ 101
4.2.2 Force on Linear Coupling ........ 104
4.2.2.1 General Surface Force Components ........ 106
4.2.2.2 Surface and Volume Force Components ........ 108
4.2.2.3 Volume Force Components ........ 110
4.2.3 Validation Using Finite Element Analysis ........ 112

4.2.4 Parameter Analysis ........ 114
4.3 Analytical Based Model for a Halbach Magnetic Lead Screw ........ 119
4.3.1 Magnetic Flux Density for the Magnetic Lead Screw ........ 126
4.3.2 Force on Magnetic Lead Screw ........ 128
4.3.2.1 General Surface Force Components ........ 129
4.3.2.2 Surface and Volume Force Components ........ 132
4.3.2.3 Volume Force Components ........ 134
4.3.3 Validation Using Finite Element Analysis ........ 136
5 Conclusions, Research Contributions and Future Works ........ 139
5.1 Conclusions ........ 139
5.2 List of Research Contributions ........ 140
5.3 Further Works ........ 141
References ........ 142

## List of Tables

Table 1-I. Performance Comparison of Various Linear Machines .................................. 24
Table 2-I. Summary of the Design Parameters ................................................................ 33
Table 2-II. Scaled-up Design; Fixed Geometric and Material Values ............................. 37
Table 2-III. Iteration of the radial parameters of the scaled-up MGLS ........................... 38
Table 2-IV. Comparison of the force capabilities ............................................................ 42
Table 2-V. Prototype Designs Geometric Parameters ...................................................... 43
Table 2-VI. Iteration of Radial Parameters ...................................................................... 43
Table 2-VII. Impact of Inner Rotor Lead Angle on Force ................................................ 50
Table 2-VIII. Geometric and material parameters ........................................................... 52
Table 3-I. Summary of the Design Parameters ............................................................... 68
Table 3-II. Performance comparison between the initial design and current design ....... 71
Table 3-III. Measured average torque and calculated power, loss and efficiency at each load step. ......................................................................................................... 75
Table 3-IV. Stator Specifications ...................................................................................... 77
Table 3-V. LCM, GCD, SPP, and SP for Different Combinations of Stator Slots and $p_1$ = 6 Pole-pair Rotor. ............................................................................................ 77
Table 3-VI. Average Torque for Each Part of Different Designs .................................... 79
Table 3-VII. Torque Ripple Comparison for Different Slot Combinations at Peak Torque Condition ........................................................................................................ 79
Table 3-VIII. Average Torque and Torque Ripple for Each Part .................................... 84
Table 4-I. Summary of geometric and material parameters .......................................... 113
Table 4-II. Summary of the ratios value for different values of $r_{IIo}$, while $\tau_p/r_{IIo}$ = 0.3.. 116
Table 4-III. Summary of geometric and material parameters ........................................ 136
Table 4-IV. Summary of the Fixed Parameter Values for Two Different Cases ........... 137

**List of Figures**


Fig. 1-1. a) Heidelberg pneumatic arm prosthesis [2], b) small hydraulic actuators with diameters of 2.3 mm and 9.6 mm for the application of prosthetic fingers [3]....... 1
Fig. 1-2. 6 DOF earthquake simulator built at the University of Minnesota [4] ................ 2
Fig. 1-3. Hydraulic Bramah Press [10] ................................................................................ 4
Fig. 1-4. a) basic hydraulic system, b) linear hydraulic actuator [11] ................................ 4
Fig. 1-5. Pneumatic system [11]. ........................................................................................ 5
Fig. 1-6. a) Exlar GSX series integrated motor/actuator with inverted roller screw, b) the standard roller screw [15]. .......................................................................................... 6
Fig. 1-7. Construction of linear motor's geometry; a) conventional motor, b) unrolled conventional motor, c) long stator motor, and d) short stator motor [20]. .............. 7
Fig. 1-8. A double sided linear induction motor topology [21] .......................................... 8
Fig. 1-9. A modular linear synchronous motor proposed by Lee *et al.* [22] ...................... 8
Fig. 1-10. Linear switched reluctance motor presented by D. Wang *et al.* [23] ; a) 3D FEA, and b) prototype. .......................................................................................... 9
Fig. 1-11. Parametric tubular machines with a) surface mounted, b) flux focusing, and c) Halbach PM translator arrangements investigated by J. Wang *et al*. [25]. ............. 9
Fig. 1-12. Three-phase tubular PM machine a) structure b) Slotted stator core for prototype [26]............................................................................................................ 10
Fig. 1-13. A modular linear PM Vernier motor [28]. ....................................................... 11
Fig. 1-14. Configuration of a linear PM Vernier motor [28]. .......................................... 11
Fig. 1-15. Spiral actuator proposed by Fujimoto *et al.* a) Structure, b and c) prototype [29] ............................................................................................................................ 12
Fig. 1-16. One phase of the multi-airgap actuator a) distributed, b) global coil [17]. ...... 13
Fig. 1-17. Multi-rod linear actuator proposed by Cavarec *et al.* [17]. .............................. 13
Fig. 1-18. Coaxial magnetic gear with $p_1 = 4$, $n_2 = 26$, and $p_3 = 22$. ............................... 14
Fig. 1-19. A LMG with $p_i$=15, $p_o$= 6 pole pairs and $n_t$ = 21 central ferromagnetic rings. 16
Fig. 1-20. Integration of LMG with linear tubular generator [44].................................... 18
Fig. 1-21. Schematic of a free-piston generator [45] ....................................................... 18
Fig. 1-22. Li's proposed magnetically geared linear generator [45]................................ 19
Fig. 1-23. Linear magnetic gear proposed by Holehouse *et al.* [43] ................................ 19
Fig. 1-24. Pole-piece translator of the Holehouse's linear magnetic gear [43] ................ 19
Fig. 1-25. An example of an MLS ................................................................................... 20
Fig. 1-26. CAD model of the proposed magnetic lead screw by Holm *et al.* [47] ........... 21
Fig. 1-27. Magnet retainer of the translator part of the magnetic lead screw by Holm *et al.* [47]............................................................................................................ 21
Fig. 1-28. a) Magnetic lead screw suspension system. b) Translator assembly procedure[49]............................................................................................ 22
Fig. 1-29. a) Lue's proposed electromagnetic lead screw. b) helical winding structure [51] ............................................................................................................................ 23
Fig. 1-30. PM machine integrated with a magnetic lead screw with Halbach pole arrangement [53]............................................................................................ 23

Fig. 1-31. Reluctance magnetic lead screw by Berg *et al.* [50] ........................................ 24
Fig. 2-1. MGLS proof of concept design; a) 3D view, b) cross-sectional parameters ..... 27
Fig. 2-2. Cut-through view of the magnetically geared lead screw showing the lead lengths for the inner outer and translator. ........................................................................ 27
Fig. 2-3. Side view of the helical lines of the inner rotor ................................................ 28
Fig. 2-4. Side view showing two consecutive skewed ferromagnetic translator rings. The definition for the translator rotor lead length $\lambda_r$ and translator lead $\lambda_t$ is also shown. ........................................................................................................................ 28
Fig. 2-5. One turn rotation of a translator ring (side view)............................................... 32
Fig. 2-6. Axial displacement of a translator ring as the function of translator angular position ........................................................................................................................ 32
Fig. 2-7 Radial flux densities and related spectrums: a) adjacent to inner rotor due to inner rotor magnets at $r$=17.55 mm), b) adjacent to outer rotor due to inner rotor magnets (at $r$=19.95 mm)........................................................................................................ 34
Fig. 2-8 Radial flux densities and related spectrums a) adjacent to outer rotor due to outer rotor (at $r$=19.95 mm), b) adjacent to inner rotor due to outer rotor (at $r$=17.55 mm) ........................................................................................................................ 34
Fig. 2-9. a) Force, and b) torque on different parts of the MGLS due to rotation of the inner rotor ........................................................................................................................ 35
Fig. 2-10. a) Force, and b) torque on different parts of the MGLS due to rotation of the inner rotor and translation of the translator at the same time ................................ 35
Fig. 2-11. Structure of the magnetically geared lead screw with $p_i$ =15 inner rotor pole-pairs, $p_o$ = 6 pole pairs and $n_t$ = 21 segments across the axial length. ................... 36
Fig. 2-12. Cut-through view of the magnetically geared lead screw showing the lead lengths for the inner outer and translator. ........................................................................ 36
Fig. 2-13. Cross-sectional dimensional parameters. ........................................................ 37
Fig. 2-14. Translation force as a function of inner rotor outer radius, $r_{io}$ and translator outer radius $r_{to}$ for iteration V. The curves for different $r_{to}$ are shown on the figure. ... 38
Fig. 2-15. The trade-off between maximizing volumetric force density and force-per-kg of magnet for iteration VI when ($r_{io}$ , $r_{to}$ ) = (48,54.5) mm. ...................................... 38
Fig. 2-16. Radial flux densities and related spectrums a) adjacent to outer rotor due to outer rotor (at $r$=54.9 mm), b) adjacent to inner rotor due to outer rotor (at $r$=48.1 mm) ........................................................................................................................ 39
Fig. 2-17. Radial flux densities and related spectrums: a) adjacent to inner rotor due to inner rotor magnets at $r$=48.1 mm), b) adjacent to outer rotor due to inner rotor magnets (at $r$=54.9 mm)........................................................................................................ 40
Fig. 2-18. Radial flux density in the outer air-gap due to magnets on both the inner and outer rotor. ........................................................................................................................ 40
Fig. 2-19. a) Force, and b) torque on different parts of the MGLS due to rotation of the inner rotor ........................................................................................................................ 41
Fig. 2-20. a) Force, and b) torque on different parts of the MGLS due to rotation of the inner rotor and translation of the translator at the same time ................................ 41
Fig. 2-21. Force per magnet volume as a function of $L_s/L_a$ ............................................. 42

Fig. 2-22. Trade-off between maximizing volumetric force density and force-per-kg of magnet material. Results shown for iteration IV .................................................. 43
Fig. 2-23. Translation force as a function of translator outer radius, $r_{to}$ and inner rotor outer radius $r_{io}$ for iteration V .......................................................................... 44
Fig. 2-24. One turn of the inner rotor helix using a) 4, b) 6, c) 12, and d) 24 magnet segments ............................................................................................................ 44
Fig. 2-25. a) Torque, and b) force when the inner rotor was rotated by 180 degrees for various designs with different inner rotor magnet arc length ................................ 45
Fig. 2-26. Side view of the segmented helical inner rotor with 60$^o$ magnet arcs ............. 46
Fig. 2-27. a) Force, and b) torque on different parts of the MGLS due to rotation of the inner rotor .................................................................................................. 47
Fig. 2-28. a) Force, and b) torque on different parts of the MGLS due to rotation of the inner rotor and translation of the translator at the same time ................................ 47
Fig. 2-29. a) Inner rotor and b) translator for the MGLS. ................................................ 47
Fig. 2-30. The MGLS on the testbed before testing. ....................................................... 47
Fig. 2-31. Radial flux density along z-axis at radial distance of 0.85 mm from the surface of the a) inner rotor and b) outer cylinder ............................................................ 48
Fig. 2-32. Translator force measurement using a load cell when it was pushing against an obstacle. ............................................................................................................ 48
Fig. 2-33. Measured and calculated translator force with and without 0.1 mm space between rings. .................................................................................................... 48
Fig. 2-34. Close up view (not to scale) of the translator pole-pieces and $w_g$ = 0.1 mm space between plastic (black) and steel rings (gray). ..................................................... 49
Fig. 2-35. Variation of the translator force as a function of space between two adjacent rings ................................................................................................................ 49
Fig. 2-36. Definition of the lead angle per ANSI/AGMA 1012-G05 [61] ...................... 50
Fig. 2-37. Parametric design to investigate the effect of the axial shift, $L_a$, between the top and bottom set of half rings ............................................................................ 51
Fig. 2-38. Maximum translator force versus axial shift, $L_a$ of the half rings .................... 52
Fig. 2-39. Proposed new MGLS ........................................................................... 52
Fig. 2-40. a) Radial flux density in the outer airgap ($r$=32.75 mm) when only inner rotor magnets present. b) Harmonic content with translator present.............................. 53
Fig. 2-41. a) Radial flux density in the inner airgap ($r$=26.25 mm) when only outer cylinder magnets. b) Harmonic content with translator presents ........................................ 53
Fig. 2-42. a) Force and b) torque on each MGLS part as a function of inner rotor phase angle................................................................................................................ 54
Fig. 2-43. a) Force and b) torque on each MGLS part due to rotation of the inner rotor and translation of the translator at the same time. ....................................................... 54
Fig. 2-44. MGLS components; a) outer cylinder, b) translator. ....................................... 55
Fig. 2-45. Calculated and measured flux density and the corresponding main harmonics at 0.85 mm above the surface of (a) inner rotor and (b) outer cylinder when they are surrounded by air. The corresponding harmonics for the inner rotor and (fixed) outer cylinder are compared in (c) and (d) respectively. ....................................... 55

Fig. 2-46. Test setup for force measurement ..................................................................... 55
Fig. 2-47. MGLS on the test bed connected to a spring load............................................ 56
Fig. 2-48. a) Measured translator force, b) measured inner rotor torque, when inner rotor was rotated while translator pushed against an obstacle. ...................................... 56
Fig. 2-49. 3D cut view of the MGLS showing the plastic rods and sleeve bearings........ 57
Fig. 2-50. Measured torque while inner rotor was rotated and translator was free to move. .............................................................................................................................. 57
Fig. 2-51. a) Measured translator force, b) measured inner rotor torque, when translator was pushed in using a mechanical actuator. .......................................................... 58
Fig. 3-1. Schematic of an AFMG [38]. ............................................................................ 60
Fig. 3-2. An axial flux magnetically geared machine proposed by Wang *et al* [67]....... 61
Fig. 3-3. Magnetic field distribution in coupled and decoupled designs [67] ................. 61
Fig. 3-4. AFMG proposed by Johnson *et al.* [69]............................................................ 63
Fig. 3-5. AFMGM proposed by Niguchi *et al.* [70].......................................................... 64
Fig. 3-6. Structure of the proposed AFMGM by Tong *et al.* [65] .................................. 64
Fig. 3-7. Exploded view of the axial flux magnetically geared machine proposed by Zaytoon *et al.* [72] ............................................................................................... 65
Fig. 3-8. Axial flux magnetically geared machine proposed by Khatab *et al.* [73]......... 66
Fig. 3-9. An axial flux magnetic gear with a flux-focusing typology proposed by Acharya *et al.* [76], [77]. a) Optimized design, b) assembly design with rectangular magnets and steel poles' lips. $p_1$= 6 $n_2$ = 25 and $p_3$ = 19. ................................................... 67
Fig. 3-10. Geometric parameters used for the axial flux magnetic gear with a flux-focusing typology [76], [77]. ........................................................................................... 68
Fig. 3-11. An axial flux magnetic gear with a flux-focusing typology based on [76], [77]. $p_1$= 6, $n_2$ = 25, and $p_3$ = 19.............................................................................. 69
Fig. 3-12. Generated mesh using JMAG FEA software .................................................. 70
Fig. 3-13. a) Axial flux density near fixed rotor 3 due to magnets only on the high-speed rotor (rotor 1) at a radius of $r$=137 mm and an axial distance of 0.5 mm. b) Corresponding harmonic contents. ........................................................................ 70
Fig. 3-14. a) Magnetic flux density near the high-speed rotor due to magnets only on the fixed rotor 3 at a radius of $r$=137 mm and an axial distance of 0.5 mm. b) Corresponding harmonic contents. ....................................................................... 70
Fig. 3-15. Torque on the low speed rotor (LSR), high speed rotor (HSR) and fixed rotor for the case when only the low speed rotor is rotating with practical design considerations. ...................................................................................................... 71
Fig. 3-16. Torque on the low speed rotor (LSR), high speed rotor (HSR) and fixed rotor for the case when both rotors were rotated with practical design considerations. 71
Fig. 3-17. Axial force characteristics of the AFMG for the case when both rotors were rotated with practical design considerations......................................................... 71
Fig. 3-18. The experimentally assembled axial flux focusing magnetic gear with a) high-speed rotor, b) low-speed rotor, and c) fixed rotor. ............................................... 72
Fig. 3-19. a) High speed rotor axial magnetic flux density at r = 135mm and 1.04mm above the axial rotor and b) corresponding spatial harmonic comparison showing the 6th,

18th, 30th, and 42nd harmonic for the measured and FEA calculated axial flux density (when surrounded by air). .......... 72
Fig. 3-20. a) Fixed rotor axial magnetic flux density field when the rotor surrounded by air at r = 135mm and z = 1.04mm above the rotor b) Corresponding harmonic analysis showing the 19th, 57th, 95th, and 133rd harmonic for measured and FEA calculated axial flux density for the fixed rotor (when surrounded by air). .......... 73
Fig. 3-21. Axial magnetic gear on the test bed .......... 73
Fig. 3-22. Measured torque on high speed and low speed rotors. .......... 73
Fig. 3-23. Measured no load torque on low speed and high-speed rotors .......... 74
Fig. 3-24. Power loss and efficiency as a function of the load torque at 50 r/min high speed rotor speed. .......... 74
Fig. 3-25. Torque ripple as a function of load for low speed rotor. .......... 75
Fig. 3-26. Torque ripple as a function of load for high-speed rotor. .......... 75
Fig. 3-27. Exploded view of the proposed AFMGM with 45 slot stator around the 6 pole-pair high speed rotor where $p_1$= 6, $n_2$ = 25, and $p_3$ = 19. .......... 76
Fig. 3-28. Stator and the high speed rotor of the proposed axial flux magnetically geared motor with a) 18, b) 36, c) 45, and d) 54 stator slots. .......... 78
Fig. 3-29. Star of slots phasor diagram of a 45slots/12poles motor. .......... 80
Fig. 3-30. Winding layout of the three phases over the first four poles. .......... 80
Fig. 3-31. Turns function of the three phases over the first four poles. .......... 81
Fig. 3-32. Winding function of the three phases over the first four poles. .......... 81
Fig. 3-33. Mesh plot for axial flux magnetically geared machine using JMAG .......... 82
Fig. 3-34. a) Axial flux density near fixed rotor 3 due to magnets only on the high-speed rotor (rotor 1) at a radius of $r$=137 mm and an axial distance of 0.5 mm. b) Harmonic contents of the modulated flux density. .......... 82
Fig. 3-35. a) Magnetic flux density near the high-speed rotor due to magnets only on the fixed rotor 3 at a radius of $r$=137 mm and an axial distance of 0.5 mm. b) Harmonic contents of the modulated flux density. .......... 82
Fig. 3-36. Normalized MMF using the winding function analysis and FEA. .......... 83
Fig. 3-37. Harmonic contents of the normalized MMF a) using FEA results b) using winding function analysis. .......... 83
Fig. 3-38. Torque on different parts. .......... 84
Fig. 3-39. Torque on the low-speed rotor and high- speed rotor as a function of stator current for the case when a fill factor of 0.3 was used. This lower fill factor was used as it was closer to the experimental value used in the prototype. A stator current of 25.4 $A_{rms}$ corresponds to a current density of 6.5A/mm$^2$ .......... 85
Fig. 3-40. The experimentally assembled stator a) lamination with winding, b) mounted on the AFMG. .......... 86
Fig. 3-41. Axial flux magnetically geared machine on the test bed. .......... 86
Fig. 3-42. Measured and calculated no-load three phase back-emf waveforms when the HSR is rotating at 50 r/min. .......... 87
Fig. 3-43. Harmonic spectrum of the a) calculated and b) measured no load back-emf voltage. .......... 87

Fig. 3-44. Simulated and measured peak back-EMF at different speeds.......................... 87
Fig. 3-45. Experimental no-load losses.............................................................................. 88
Fig. 3-46. Measured torque at HSR speed of 50 r/min at different loads. ........................ 88
Fig. 3-47. Measured loss and efficiency as a function of load ........................................ 88
Fig. 4-1. One period of the Halbach array ........................................................................ 92
Fig. 4-2. Magnetization plots of the Halbach array .......................................................... 93
Fig. 4-3. Harmonic spectrum of the magnetization ........................................................... 96
Fig. 4-4. Geometry definition for inner part of the linear coupling .................................. 96
Fig. 4-5. Point charge and related coordinate parameters................................................. 96
Fig. 4-6. Linear coupling, a) axial parameters, and b) cross sectional parameters ......... 105
Fig. 4-7. a) 3D FEA model of a Halbach linear coupling b) the mesh. .......................... 113
Fig. 4-8. FEA and analytically calculated magnetic flux density a) radial b) axial........ 113
Fig. 4-9. FEA and analytically calculated force ............................................................. 114
Fig. 4-10. A 2D cut-view of a Halbach cylinder............................................................. 114
Fig. 4-11. a) Volumetric force density, and b) mass force density as a function of $r_{Ii}/r_{Io}$ and $r_{Io}/r_{IIo}$, when $r_{IIo}$ = 30 mm and $\tau_p/r_{IIo}$ = 0.3. ........................................................ 115
Fig. 4-12. Volumetric force density versus mass force density for different configurations within the design space, when $r_{IIo}$ = 30 mm and $\tau_p/r_{IIo}$ = 0.3. ............................ 116
Fig. 4-13. a) Volumetric and b) Mass force density as a function of $r_{Ii}/r_{Io}$ for three different value of $r_{Io}/r_{IIo}$, when $r_{IIo}$ = 30 mm and $\tau_p/r_{IIo}$ = 0.3. .......................................... 117
Fig. 4-14. a) Volumetric force density, and b) mass force density as a function of $\tau_p/r_{IIo}$ and $r_{Io}/r_{IIo}$, when $r_{IIo}$ = 30 mm and $r_{Ii}/r_{Io}$ = 0.7......................................................... 117
Fig. 4-15. Mass force density while geometric parameters satisfy (4.111) for a) $r_{IIo}$ = 30 mm and b) $r_{IIo}$ = 100. .......................................................................................... 118
Fig. 4-16. Maximum mass force density for different values of $r_{IIo}$. ............................. 118
Fig. 4-17. Maximum mass force density for different values of $r_{IIo}$ as a function of $r_{Ii}$. 118
Fig. 4-18. One period of the Halbach array .................................................................... 120
Fig. 4-19. Magnetization plots of the Halbach array ...................................................... 120
Fig. 4-20. Geometry definition for inner part of the MLS .............................................. 123
Fig. 4-21. Point charge and related coordinate parameters............................................. 123
Fig. 4-22. Magnetic lead screw, a) axial parameters, and b) cross sectional parameters 128
Fig. 4-23. 3D FEA model of a Halbach MLS ................................................................. 136
Fig. 4-24. FEA and analytically calculated flux density a) radial b) axial ..................... 137
Fig. 4-25. Calculated force using FEA and analytical model ......................................... 137
Fig. 4-26. Case1: calculated force of LPMC and MLS a) using FEA and b) using analytical model ............................................................................................................... 138
Fig. 4-27. Case 2: calculated force of LPMC and MLS a) using FEA and b) using analytical model ............................................................................................................... 138

## List of Abbreviations

| | |
|---|---|
| AFMG | Axial flux magnetic gear |
| AFMGM | Axial flux magnetically geared machine |
| AFPM | Axial flux PM machine |
| DOF | Degrees of freedom |
| ELA | Electromagnetic linear actuator |
| EMA | Electromechanical linear actuators |
| EMLS | Electromagnetic lead screw |
| FEA | Finite element analysis |
| HEV | Hybrid electric vehicle |
| LCM | Least common multiple |
| LIM | linear induction motor |
| LMG | Linear magnetic gear |
| LSM | linear synchronous motor |
| LSRM | Linear switched reluctance motor |
| MG | Magnetic gear |
| MGLS | Magnetically geared lead screw |
| MGM | Magnetically geared machine |
| MLS | Magnetic lead screw |
| PM | Permanent magnet |
| PTO | Power take off |
| SPP | slot per pole per phase |
| WEC | Wave energy conversion |
| WFA | Winding function analysis |

## List of Symbols

| | |
|---|---|
| $B$ | Magnetic flux density |
| $C_T$ | Cogging factor |
| $F$ | Force |
| $f_e$ | Electrical frequency |
| $GCD$ | Greatest common devisor |
| $G_r$ | Gear ratio |
| $k$ | Wave number |
| $L$ | Active length |
| $n$ | Number of steel pole-pieces |
| $N(\theta)$ | winding function |
| $n(\theta)$ | Turns function |
| $\langle n(\theta) \rangle$ | Average of the turns function |
| $N_t$ | Number of turns per coil |
| $p$ | Number of pole-pairs |
| $P_L$ | Power loss |
| $Q$ | Number of slots |
| $q$ | Slot per pole per phase |
| $r$ | Radius |
| $T$ | Torque |
| $t$ | Machine periodicity |
| $v$ | Translational speed |
| $V_{Fd}$ | Volumetric force density |
| $\alpha$ | Lead angle |
| $\alpha^e{}_s$ | Electrical phase shift between slots |
| $\theta$ | Angular position |
| $\lambda$ | Lead length |
| $\omega$ | Angular speed |

# 1 Chapter 1: Introduction

## 1.1 Motivation

Actuators are devices that convert energy from an external source into mechanical energy [1]. Actuators have a wide range of applications in everyday life; from a small hand prosthetic to a giant excavator, from an active car suspension system to an ocean energy power take off, and from a simple lock system to a very complicated automation system.

Fig. 1-1-a shows the Heidelberg pneumatic arm prosthesis, which was the first practical externally-powered prosthesis [2]. Fig. 1-1-b shows two examples of small hydraulic actuators that have recently been developed for use in prosthetic fingers [3]. The diameters of these actuators are just 2.3 mm and 9.6 mm respectively. The 2.3 mm actuator provides 10.9 N of force and the 9.6 mm diameter actuator provides 89 N of force. As an example of a large-scale actuator, Fig. 1-2 shows the size of the eight hydraulic actuators used on a 6 degree-of-freedom earthquake simulator built at the University of Minnesota. Each actuator has the capability of applying a force of 3910 kN [4].

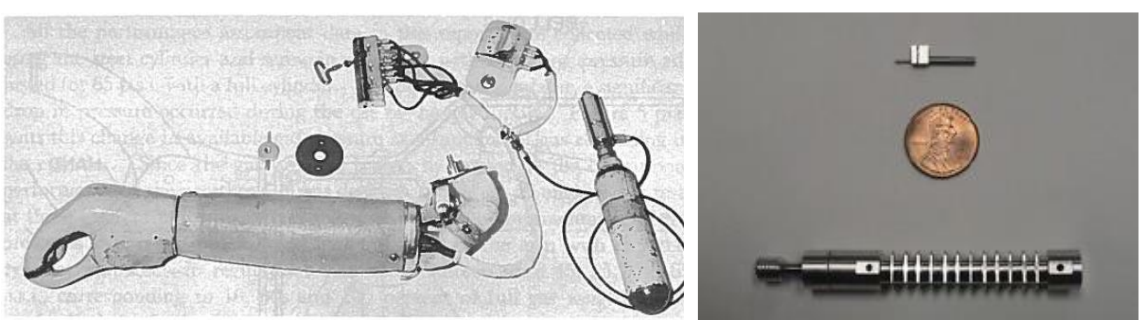

(a) (b)

Fig. 1-1. a) Heidelberg pneumatic arm prosthesis [2], b) small hydraulic actuators with diameters of 2.3 mm and 9.6 mm for the application of prosthetic fingers [3]

Fig. 1-2. 6 DOF earthquake simulator built at the University of Minnesota [4]

Actuators are characterized by their performance indices: maximum stress (normalized force), maximum strain (normalized displacement), maximum volumetric power density, maximum mass power density, bandwidth (responsiveness), resolution and stiffness (load holding ability) [1], [3]. Different kinds of technologies have been developed to satisfy application-specific requirements. They can be categorized based on mechanisms of energy transfer. Hydraulic, pneumatic, electromechanical, and electromagnetic actuators are the most conventional technologies, which are called macro-motion actuators. Other types of actuators termed micro-motion actuators include; piezoelectric, magnetostrictive, shape memory alloy, and polymeric actuators [5].

Due to the wide range of applications for actuators, achieving high performance actuation is important. One of the challenges in this area is the design of high force, long stroke, and compact actuators. The focus of this dissertation is on conventional macro-motion actuators.

## 1.2 Literature Review

In this section, characteristics, advantages and disadvantages of different kinds of actuators are given, and the most recent advancement in this area are discussed. This section also provides a comparison of different designs in terms of force density and shear stress.

### 1.2.1 Hydraulic Actuators

Hydraulic actuators are conventional fluid-powered actuators. These actuators convert the energy of a pressurized fluid to mechanical motion. One of the earliest machines using hydraulic actuators was a hydraulic press by Joseph Bramah in 1795, which was based on Pascal's Hydrostatic Paradox [6]. The Bramah press, shown in Fig. 1-3, used water as the fluid.

Oil is more commonly used as a fluid in modern hydraulic actuators. Since oil is almost impossible to compress, these actuators operate at very high force densities. For instance, an excavator hydraulic piston can routinely operate at a pressure of 38 MPa [7]. The maximum pressure of hydraulic actuators is in the range of 20-70 MPa [8]. A basic hydraulic system and a linear hydraulic actuator are shown in Fig. 1-4. A regular hydraulic actuator contains a cylinder, an accumulator, control valves, a pump and motor, filters, reservoir, hoses and fittings. These auxiliary components make them relatively bulky and complicated. They are also prone to leakage. The hydraulic fluid becomes contaminated with particles, requiring filtration. Noisy pumps make them loud. Due to the very complex physics behind fluid power, their modeling and control is also complicated [9].

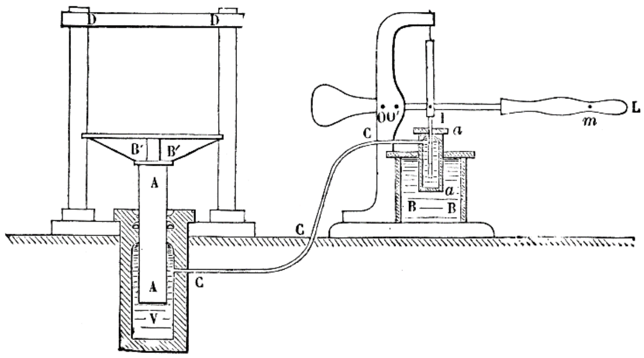

Fig. 1-3. Hydraulic Bramah Press [10]

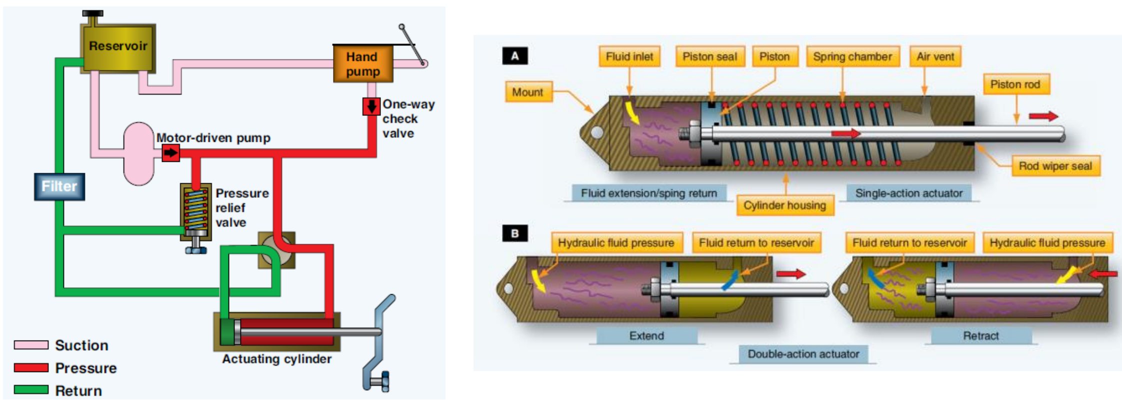


(a) (b)

Fig. 1-4. a) basic hydraulic system, b) linear hydraulic actuator [11]

### 1.2.2 Pneumatic Actuators

The operational principle of a pneumatic actuator is similar to that of a hydraulic actuator, except that they use compressed air instead of pressurized fluid as the actuation medium. The higher compressibility, lower viscosity and poor lubrication of air in comparison to oil results in lower force density, a higher leakage possibility, and lower efficiency relative to hydraulic counterparts [5]. Pneumatic actuator systems can be bulky because of the need for air compressors. In applications with limited space, their command valve needs to be placed relatively far away from the actuator, which causes a delay in response [12]. The main advantages of pneumatic actuators over hydraulic actuators are that they are cleaner, they respond faster, and they are lighter, because there is no need for a return line. An example of a pneumatic system used in an airplane is depicted in Fig. 1-5.

Ktesibios of Alexandria was known as the founder of pneumatics [13]. He invented a pneumatic catapult in 300 BC. The maximum pressure of a pneumatic actuator is in the range of 0.5-0.9 MPa, which is considerably lower than the working pressures used in hydraulic actuators [8].

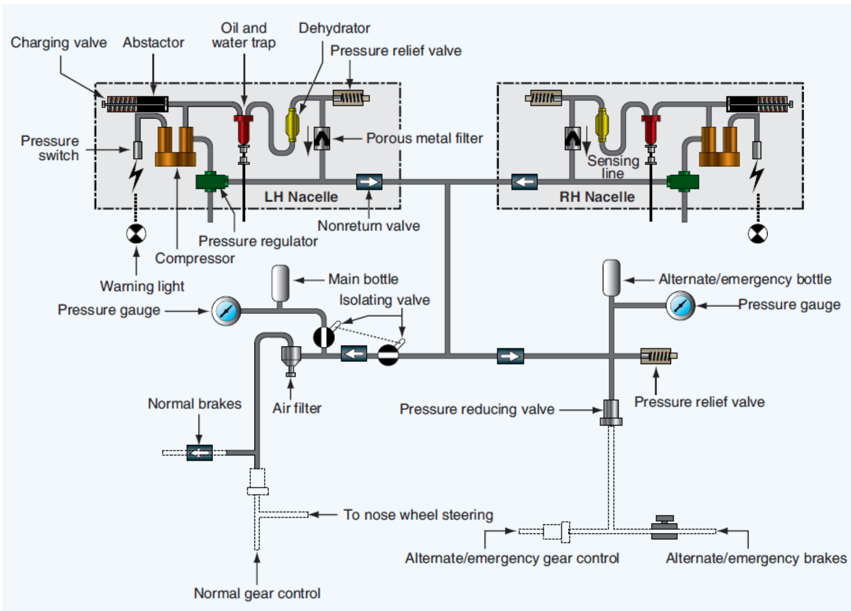


Fig. 1-5. Pneumatic system [11].

### 1.2.3 Electromechanical Linear Actuators

Electromechanical linear actuators (EMA) are usually constructed using a mechanical ball/roller screw driven by a rotary electric motor either directly or via a set of gears. They have several advantages over hydraulic and pneumatic actuators including simpler control due to the elimination of valves, pumps, filters and sensors; a longer operational lifetime, when maintained properly; lower maintenance requirements; lower noise; and, they do not use any hazardous fluids [14].

Fig. 1-6 shows an electromechanical linear actuator made by Exlar Company. It consists of two main components; a roller screw and a PM brushless motor. This Exlar GSX30 series actuator has a lead of 5.08 mm, and a maximum stroke of 457 mm [15]. It can provide a continuous force of 1995 N, which results in a force density of 730 kN/m$^3$.

Even if maintained properly, roller screws can still fail from metal fatigue or abrasion of the thread flanks. Proper lubrication and sealing from environmental contamination can prevent other failures and increase the life time of the roller screw. Lack of lubrication causes heat build-up, which can lead to failure. If metal chips get into the roller screw due to improper sealing, a failure might then happen [14].

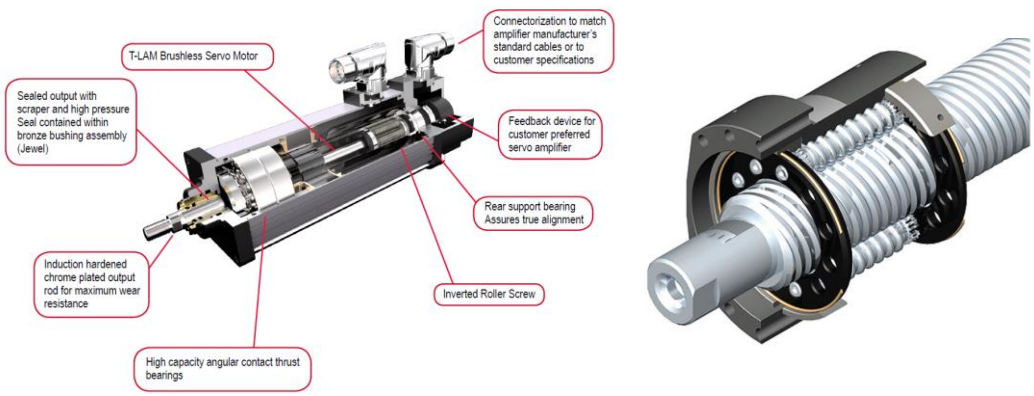


(a) (b)

Fig. 1-6. a) Exlar GSX series integrated motor/actuator with inverted roller screw, b) the standard roller screw [15].

### 1.2.4 Electromagnetic Linear Actuators (Direct Drive Actuators)

Electromagnetic linear actuators (ELA) convert electrical and/or magnetic energy to mechanical energy. ELAs have the advantage over hydraulic, pneumatic, and mechanical mechanisms of being able to operate with higher efficiency, and they are potentially more reliable [7]. Since computer-based controllers use electrical signals, they are ideal for computer control [16]. Replacing the mechanical gears results in cost saving, noise and maintenance reduction, and increased mechanical bandwidth [17].

ELAs are in fact linear motors. They can be abstracted as split and unrolled rotary motors, as illustrated in Fig. 1-7. Therefore, they have as many typologies as the rotary motor, including reluctance, induction, and synchronous linear motors [18]. The first linear motor was a reluctance type invented by Charles Wheatstone in 1845 [18]. Depending on the type of machine, two main force components exist; the Lorentz force, which is due to the interaction of a current carrying coil and a magnetic source field [19]; and reluctance force, which is due to the interaction of a magnetic source field and a salient ferromagnetic core. The magnetic source field can be created by either permanent magnets (PM) or a secondary coil. Either the stator or translator needs to be made longer, which results in a long stator and a short stator machine, respectively [20]. These are shown in Fig. 1-7 (c) and (d) respectively. Induction and synchronous machines with a long stator are expensive. Short stator versions on the other hand cause difficulty in sliding contact arrangement [20]. Linear motors suffer from two edge effects; longitudinal, and transversal. These edge effects are shown in Fig. 1-8.

The force density of ELAs is constrained by current density and magnetic saturation. Induced current in linear induction motor (LIM) structure causes additional thermal limitations, which further limits the generated force.

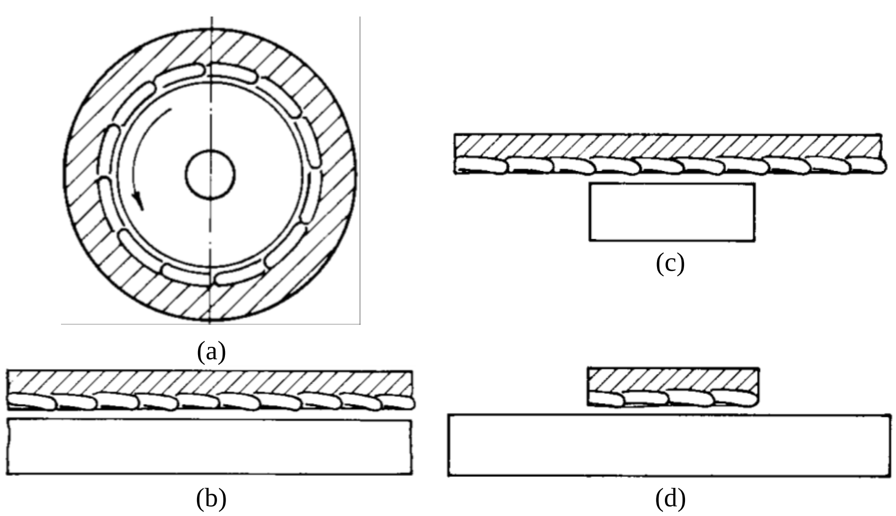


Fig. 1-7. Construction of linear motor’s geometry; a) conventional motor, b) unrolled conventional motor, c) long stator motor, and d) short stator motor [20].

An example of a double-sided LIM (DSLIM) investigated by Abdollahi *et al.* [21] for a transportation application is shown in Fig. 1-8. It consist of one aluminum or copper secondary sandwiched between two laminated primary stacks.

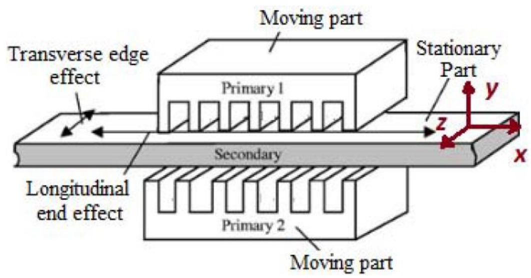


Fig. 1-8. A double sided linear induction motor topology [21]

The linear synchronous motor (LSM), like its rotary counterpart, has an armature winding, and a secondary magnetic source field created by PMs. An example of a modular LSM proposed by Lee *et al.* [22] is shown in Fig. 1-9. This motor was designed for an ultra-high speed tube train.

A Linear switched reluctance motor (LSRM) example is shown in Fig. 1-10. In this double-sided design, studied by D. Wang *et al.* [23], windings on one part provide the magnetic flux inside the machine, and the variation of the reluctance due to a relative displacement of the salient translator creates the reluctance force. The force density was reported to be 58 kN/m$^3$, with a shear stress of 8.6 kN/m$^2$.

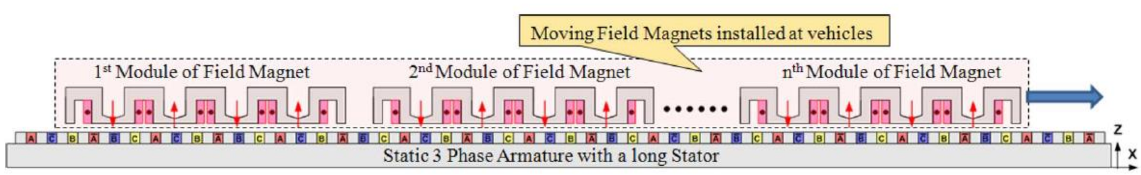


Fig. 1-9. A modular linear synchronous motor proposed by Lee *et al.* [22]

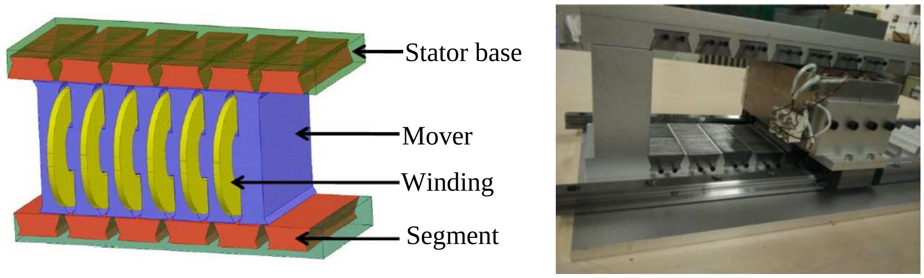


(a) (b)

Fig. 1-10. Linear switched reluctance motor presented by D. Wang *et al.* [23] ; a) 3D FEA, and b) prototype.

Tubular linear motors are another type of ELA, which can be formed by simply rolling up a conventional linear motor around its longitudinal axis [24].

A synchronous tubular linear motor with three different PM arrangements was investigated by J. Wang *et al.* [25]. The parametric designs are shown in Fig. 1-11. After completing a parametric optimization, Wang showed that the surface mounted, flux focusing, and Halbach PM translator arrangements had a volumetric force density of 225 kN/m$^3$, 258 kN/m$^3$ and 234 kN/m$^3$ respectively. An example of an interesting three-phase tubular PM machine with a modular stator is shown in Fig. 1-12, which was proposed by J. Wang *et al.* [26]. A Halbach PM arrangement was used on the translator. A maximum force density of 324 kN/m$^3$ was calculated.

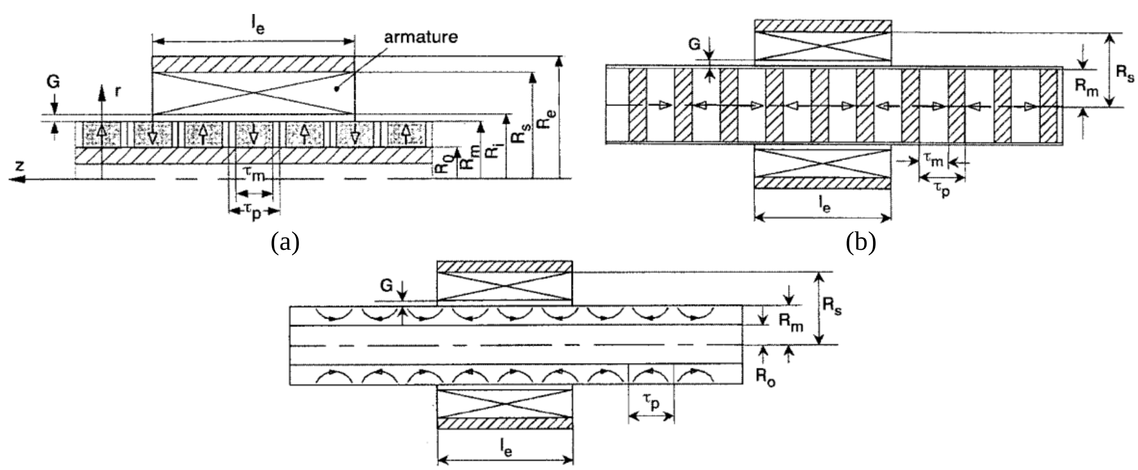


(c)

Fig. 1-11. Parametric tubular machines with a) surface mounted, b) flux focusing, and c) Halbach PM translator arrangements investigated by J. Wang *et al.* [25].

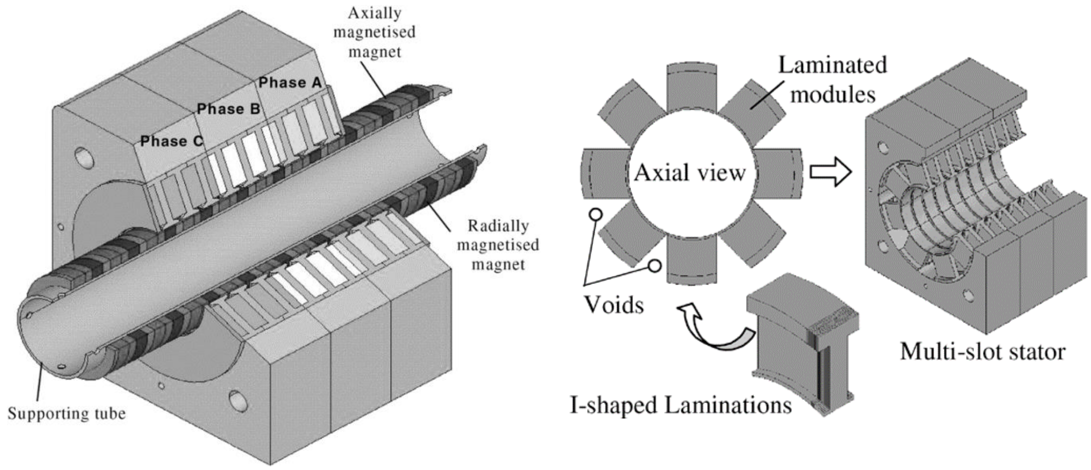


(a) (b)

Fig. 1-12. Three-phase tubular PM machine a) structure b) Slotted stator core for prototype [26]

It is challenging for an ELA to create a high force at low speed. ELAs are inherently better suited for operating at high power density rather than high force density. A linear Vernier motor concept was proposed by Lee (1963) in [27] to increase the force density of an ELA. It relied on harmonic modulation to increase the electrical speed. An example of a linear PM Vernier motor is shown in Fig. 1-13 [28]. The translator in this motor consist of a simple iron core with $n_t$ = 17 active salient teeth. The modular stator consists of a set of U-shaped laminated cores with additional magnets that have been placed on the teeth surface. The translator teeth modulate the magnetic field of the PMs to generate additional harmonics in the airgap, which then interact with the magnetic field of the stator winding to generate force. The relationship between the PM and stator pole-pairs and translator teeth must satisfy [28]:

$$P_{fe} = \left| P_{PM} - n_t \right| \tag{1.1}$$

where $P_{fe}$, $P_{PM}$, and $n_t$ are the number of pole-pairs of the effective magnetic field, PM pole-pairs, and translator teeth respectively. $P_{fe}$ is designed to be unity to achieve the highest thrust force. This results in $P_{PM}$ = 16 pole-pairs.

The operational principle of this machine is similar to the flux reversal PM machine [28]. The flux linkage in the coil is maximum when the PMs are aligned with the translator teeth. It goes to zero as the translator teeth move to the unaligned position, and then reverses polarity. The calculated force density for this design was reported to be 305 kN/m$^3$, with a shear stress of 27.4 kN/m$^2$.

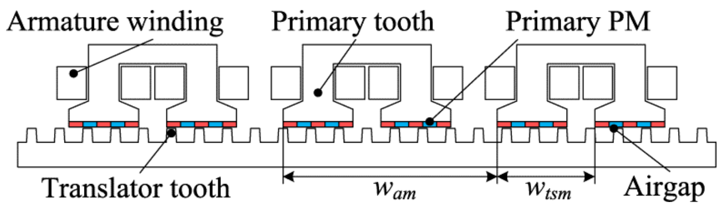


Fig. 1-13. A modular linear PM Vernier motor [28].

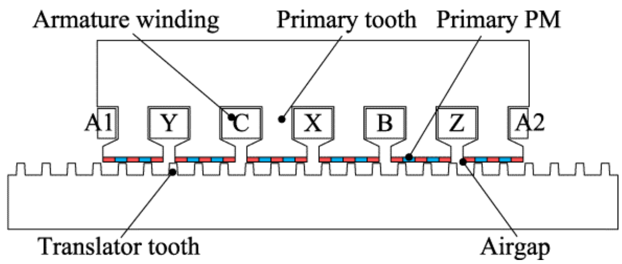


Fig. 1-14. Configuration of a linear PM Vernier motor [28].

Fig. 1-14 shows the configuration of a linear PM Vernier motor with a more traditional three-phase distributed winding. A force density of 285 kN/m$^3$, and a shear stress of 45 kN/m$^2$ were calculated for this design [28]. These results show that although the force density of the this Vernier motor is lower than that of previous Vernier motors, due to the thicker yoke of the iron core, this motor provides higher shear stress [28].

Fujimoto *et al.* proposed an axial-gap spiral linear actuator [29]. It consists of a spiral stator with a three-phase winding and a spiral mover, which contains PMs. The motor is shown in Fig. 1-15. Due to load fluctuation, the airgap of this device needs to be controlled. Two methods were proposed in [29]. First, the mover rotation angle were actively controlled by torque, which is similar to the concept of magnetic levitation control. Second, a ballscrew was used at the axis of the mover to control the airgap.

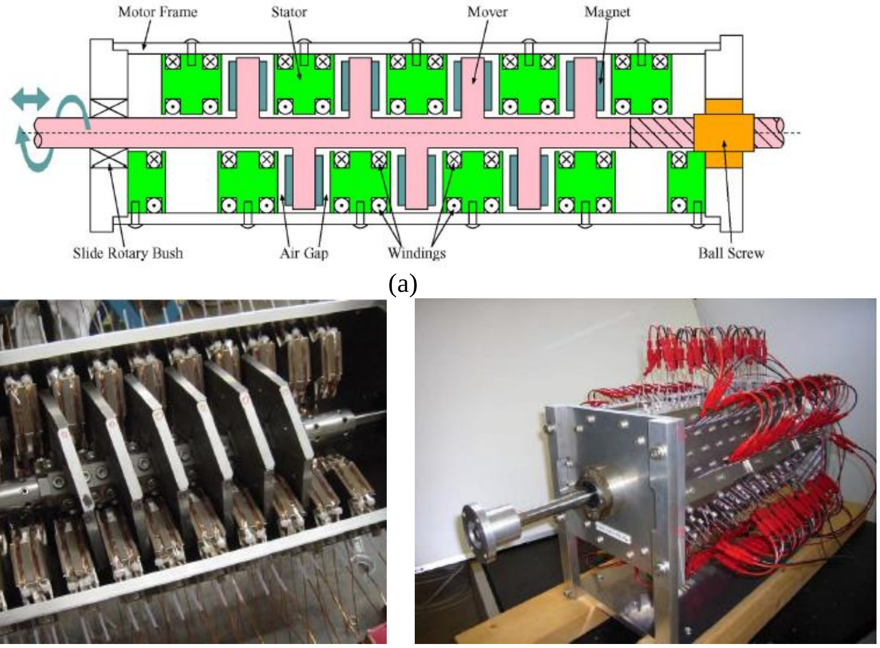


Fig. 1-15. Spiral actuator proposed by Fujimoto *et al.* a) Structure, b and c) prototype [29]

A calculated force density of 274 kN/m$^3$ and a shear stress of 18 kN/m$^2$ were reported for this machine [29]. This machine has a complicated structure and is costly to build, especially when a long stroke length is required. The airgap control also adds to the complexity of the proposed machine. A ball screw driven by a conventional rotary machine might result in a simpler design with even better performance than this machine.

Another approach to increase the effective airgap is to use a multi-airgap structure. Fig. 1-16 shows the structure of two types of multi-airgap actuators proposed by Cavarec *et al.* [17]. In the distributed stator design shown in Fig. 1-16-a, all the layers of the translator have a stator winding, while in Fig. 1-16-b one coil provides the magnetic field and surrounds all the layers [17]. The distributed coil structure can be considered as several parallel single-airgap actuators. A scaling analysis was completed in [17] for these two types of multi-airgap actuators and it was shown that the global winding structure shown in Fig. 1-16-b had the highest force density.

Based on the findings of this research, Cavarec *et al.* proposed a multi-rod linear actuator (MRLA) [17]. This topology is shown in Fig. 1-17. A force density of 1000 kN/m$^3$ was reported for this design. A summary of the performance of each of these ELAs is provided in Table 1-I on page 24.

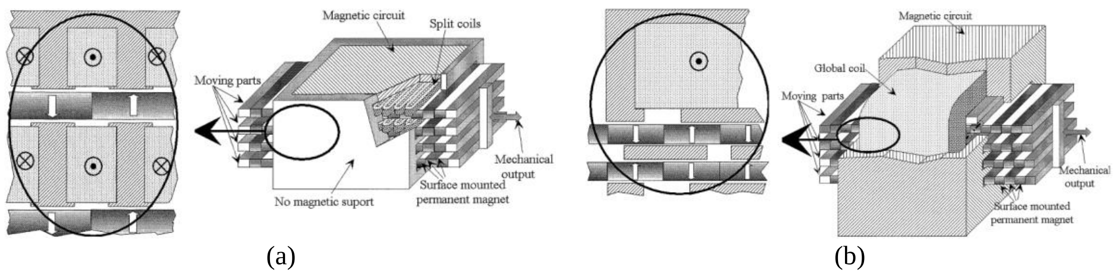


Fig. 1-16. One phase of the multi-airgap actuator a) distributed, b) global coil [17].

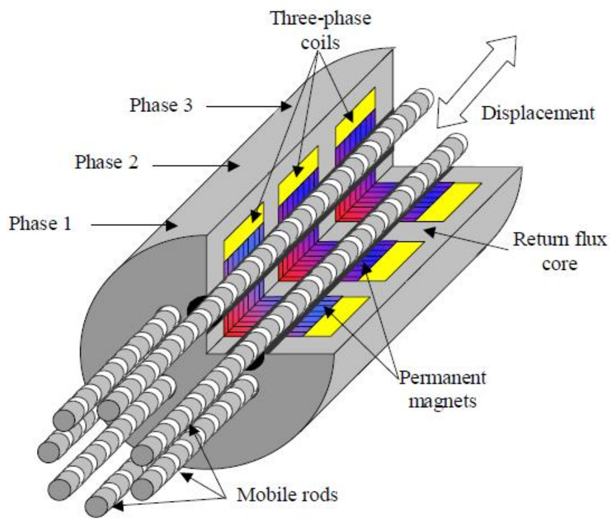


Fig. 1-17. Multi-rod linear actuator proposed by Cavarec *et al.* [17].

### 1.2.5 Magnetic Gears

With the advancement in PM material in recent years, various mechanically-inspired magnetic devices have been invented that exhibit high force density. MGs rely only on magnetic loading, and provide speed/motion and torque/force conversion like their mechanical counterparts, but without thermal constraints (current density limits). Unlike mechanical gears, a MG's contact-less operation enables it to operate without oil and it can operate with low noise, and higher efficiency. Its reliance on magnetic torque also provides overload protection. Furthermore, as MGs rely only on magnetic loading, they overcome the limitation of the ELAs.

Various kinds of MGs have been proposed to date, including a PM spur gear by Faus [30], a magnetic worm gear by Kikuchi [31], and a magnetic planetary gear by Haung *et al.* [32]. Although these mechanically-inspired devices could provide a contactless speed conversion, their torque densities are not comparable to their mechanical counterpart, because of a lack of strong PM materials, as well as their low active material usage. To solve the later problem, Neuland [33] proposed a coaxial MG, which was later improved by Reese [34] and then Martin [35]. Martin's design uses ferrite magnets. In 2001, Atallah [36] calculated that a coaxial MG using NdFeB magnets could achieve a higher torque density than a direct drive motor. Fig. 1-18 shows the structure of a coaxial MG, which contains three concentric parts; an inner rotor and outer rotor with $p_i$ and $p_o$ number of PM pole-pairs, which can rotate at the speed of $\omega_i$ and $\omega_o$ respectively, and a cage rotor with $n_t$ steel pole-pieces, which can rotate at the speed of $\omega_t$.

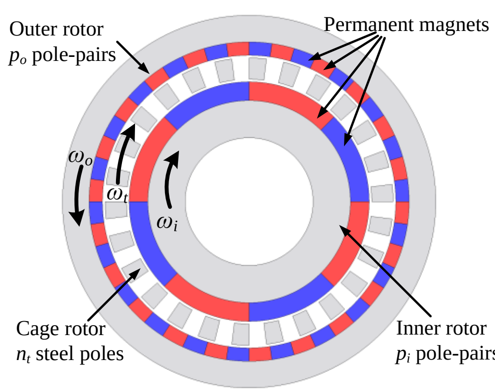


Fig. 1-18. Coaxial magnetic gear with $p_1$ = 4, $n_2$ = 26, and $p_3$ = 22.

The ferromagnetic pole-pieces of the cage rotor modulate the magnetic field within the two airgaps. The inner rotor field is modulated by the cage rotor and therefore generates additional spatial harmonics. In order to create coupling between the rotors, the number of pole-pairs of the space harmonics must satisfy [36]:

$$\begin{gathered} p_{m,k} = \left| m p_i + k n_t \right| \\ m = 1, 3, 5, \ldots, \infty;\ k = \pm 1, \pm 2, \pm 3, \ldots, \pm\infty \end{gathered} \tag{1.2}$$

By satisfying (1.2) the speed of the rotors is related by:

$$\omega_{m,k} = \frac{m p_i}{m p_i + k n_t} \omega_i + \frac{k n_t}{m p_i + k n_t} \omega_t \tag{1.3}$$

The highest asynchronous space harmonic field can be achieved by choosing $m$=1 and $k$=-1, resulting in:

$$p_{1,-1} = \left| p_i - n_t \right| \tag{1.4}$$

Therefore, $p_o = p_{1,-1}$ and (1.4) can be written as:

$$p_o = \left| p_i - n_t \right| \tag{1.5}$$

The force is maximized when

$$n_t = p_i + p_o \tag{1.6}$$

Substituting (1.6) into (1.3) and rearranging gives [37]

$$\omega_i = \frac{n_t}{p_i} \omega_t - \frac{p_o}{p_i} \omega_o \tag{1.7}$$

If $\omega_o = 0$, the speed relationship simplifies to:

$$\omega_i = \frac{n_t}{p_i} \omega_t \tag{1.8}$$

where the gear ratio is defined as $G_r = n_t / p_i$.

Mezani [38] proposed an axial flux MG (AFMG) based on the same concept as the coaxial MG. A harmonic MG by Rens [39], and cycloidal MG by Jorgensen [40] are two other types of MGs with non-uniform airgaps. However, these two types of MG are difficult to control, and the non-uniform airgap degrades bearing life. In all the aforementioned MGs, the speed conversion happens between two rotary motions.

The focus of this thesis is on linear and axial MG actuators, and therefore the rest of this chapter reviews these types of MG. Linear MG actuators can be categorized into two categories; linear magnetic gears (LMG), and magnetic lead screws (MLS). The LMG and MLS rely only on magnetic loading and therefore a higher magnetic air-gap shear stress can be sustained when compared to the ELAs.

#### 1.2.5.1 Linear Magnetic Gears

Atallah *et al.* in 2005 proposed a LMG [41]. An example of this actuator is shown in Fig. 1-19; it uses magnetic field heterodyning to create linear motion speed change without any physical contact.

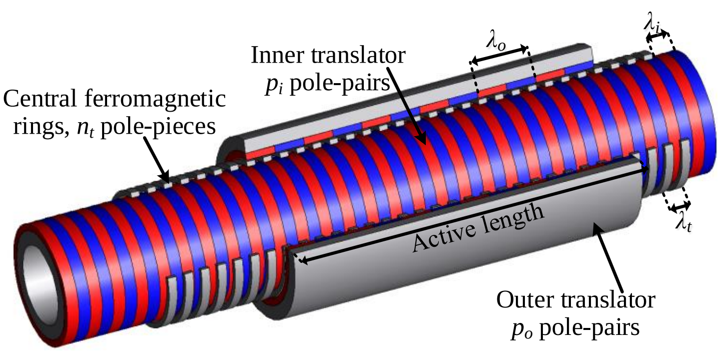


Fig. 1-19. A LMG with $p_i$=15, $p_o$= 6 pole pairs and $n_t$ = 21 central ferromagnetic rings.

The LMG, consists of three concentric tubular parts, an outer cylinder containing, $p_o$ pole-pairs that can move with a translational velocity $v_o$, an inner cylinder containing $p_i$ pole-pairs that can translationally move at velocity $v_i$, and a central section that contains $n_t$ ferromagnetic rings. The ferromagnetic rings can move at velocity $v_t$. The ferromagnetic rings modulate the magnetic fields within the two airgaps. The inner and outer translator fields are modulated by the ferromagnetic ring pieces and therefore create additional spatial harmonics within the outer and inner airgaps respectively. Due to the interaction of these magnetic fields with existing magnetic fields within the airgaps, a force is generated only if the relationship between pole pairs of the three parts satisfies the same condition as given by (1.6). With (1.6) satisfied the translational speed relationship is:

$$v_i = \frac{n_t}{p_i} v_t - \frac{p_o}{p_i} v_o \tag{1.9}$$

Unlike the rotary counterpart, the number of pole-pairs must fit within a fixed axial length, $L$. Therefore the following lead length can also be defined:

$$\lambda_i = L/p_i \tag{1.10}$$

$$\lambda_o = L/p_o \tag{1.11}$$

$$\lambda_t = L/n_t \tag{1.12}$$

These are shown on Fig. 1-19. If the outer translator is held stationary, then (1.9) shows that the translational speed can be increased by a gear ratio of $n_t/p_i$.

Atallah and Holehouse [41]–[43] demonstrated that a 3.25 gear ratio LMG with radially magnetized PMs is capable of operating with a force density of 1.89 MN/m$^3$, and Atallah *et al.* showed that employing Halbach magnetization increases the force density to 2

MN/m$^3$ [42]. This force density was achieved when the ratio of the radially-magnetized PMs to the pole-pitch was 0.7. The calculated shear stress for the Halbach design was 110 kN/m$^2$. And by combining a LMG with a linear motor, the system force density can increase by up to 100% in comparison with a direct drive system [42]. The integration of a LMG with a linear machine has been considered for various applications. Li *et al.* [44] proposed using a magnetically geared generator for use in an ocean power generation application. Fig. 1-20 shows Li's proposed machine. It consist of a linear PM tubular generator cascaded with a LMG. It is claimed that this machine offers higher efficiency, and higher power density than a conventional direct-drive machine [44].

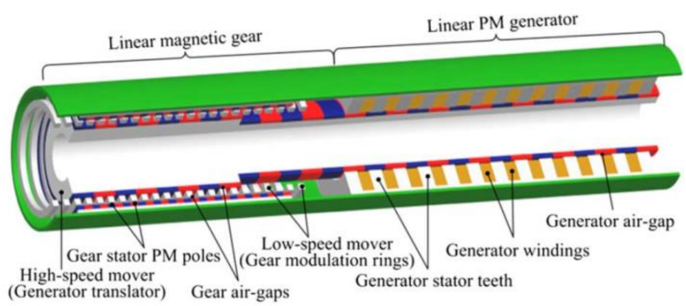


Fig. 1-20. Integration of LMG with linear tubular generator [44]

Li *et al.* [45] offered a different configuration of a magnetically geared linear generator as a free-piston generator (Fig. 1-21) for a series hybrid electric vehicle. Fig. 1-22 shows the structure of the proposed design. The stator winding of the linear generator is located around the LMG.

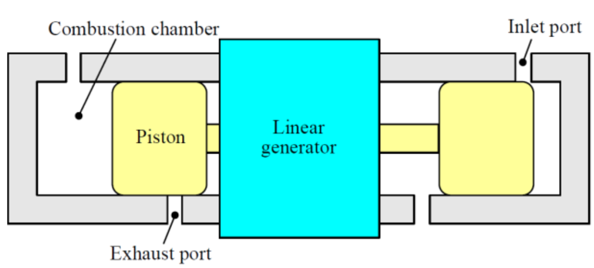


Fig. 1-21. Schematic of a free-piston generator [45]

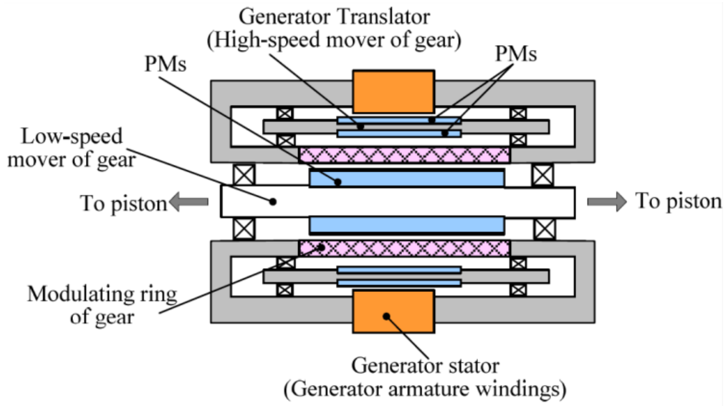

Fig. 1-22. Li’s proposed magnetically geared linear generator [45]

Holehouse *et al.* [43] experimentally tested the LMG shown in Fig. 1-23. They showed that the transmitted force is very sensitive to the spacing between the pole-piece rings of the translator. A 5% reduction in the axial length of the plastic spacer resulted in a 30% reduction in the generated thrust. Fig. 1-24 shows the pole-piece translator of this design.

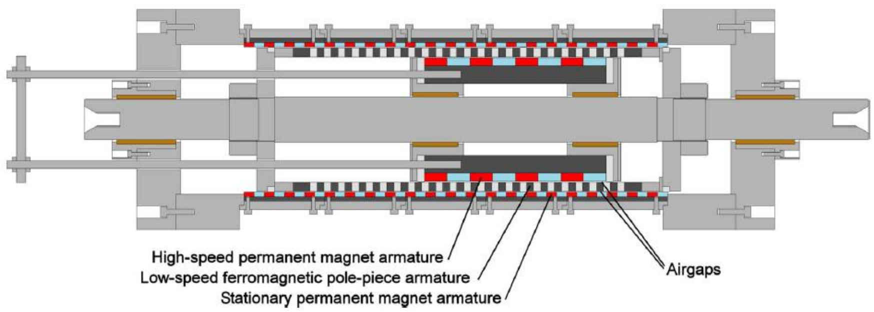

Fig. 1-23. Linear magnetic gear proposed by Holehouse *et al.* [43]

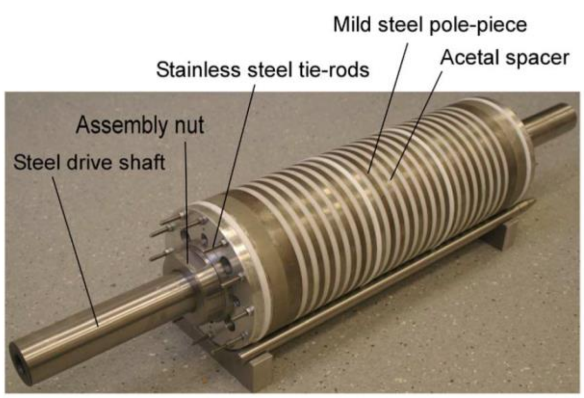

Fig. 1-24. Pole-piece translator of the Holehouse’s linear magnetic gear [43]

#### 1.2.5.2 Magnetic Lead Screw

The MLS converts linear motion to rotary motion using helically shaped magnets. An example of a MLS is shown in Fig. 1-25. The principle of operation of the MLS is analogous to a mechanical nut and screw but with a magnetic rotating "screw" and a magnetic translating "nut". Both parts are made of helically-disposed, radially-magnetized PMs on the inner and outer steel yokes.

The relationship between translating velocity, $v_i$, and outer angular velocity, $\omega_i$, is given by [46].

$$\omega_i = k_i v_i \tag{1.13}$$

where the inner rotor wave number is

$$k_i = 2\pi / \lambda_i \tag{1.14}$$

and $\lambda_i$ = inner rotor lead. This is twice the magnet pole-pitch for a double-start helical structure as shown in Fig. 1-25. The screw will travel by $\lambda_i$ when the inner rotor rotates by one turn. Depending on the number of helix starts, different values are possible for $k_i$, and consequently various gear ratios are possible. Assuming a no-loss system, the translator force and rotor torque relationship are calculated as [46]:

$$T_i = \frac{F_t}{k_i} \tag{1.15}$$

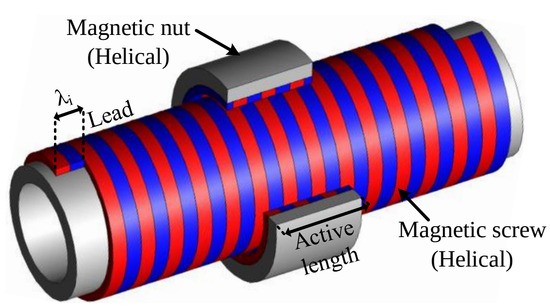


Fig. 1-25. An example of an MLS

Wang calculated that the MLS could achieve a force density of 10 $MN/m^3$ and shear stress in excess of 180 $kN/m^2$ for airgap lengths in the range or 0.4 mm to 0.8 mm and a lead $\lambda_i$ greater than 7 mm [46]. Recently, Holm *et al.* experimentally verified the performance of a 17 kN MLS for a wave energy converter [47], [48].

The calculated force density and shear stress were 2.62 $MN/m^3$ and 130 $kN/m^2$ respectively. Fig. 1-26 shows the CAD model of the proposed MLS. In order to construct the helical structure of the MLS, Holm *et al.* used round embedded magnets. The design used a total of 4340 magnets. The magnet retainer for the translator part is shown in Fig. 1-27.

Berg tested a MLS for active vehicle suspension, which is shown in Fig. 1-28-a [49]. A segmented structure was used to construct the helical rotor and translator. The authors used a polygon back-iron and square shaped magnets to make the threads. The assembly procedure of the translator is shown in Fig. 1-28-b.

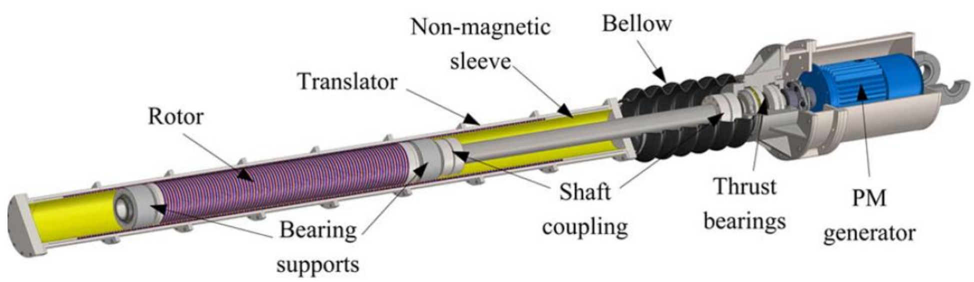


Fig. 1-26. CAD model of the proposed magnetic lead screw by Holm *et al.* [47]

Fig. 1-27. Magnet retainer of the translator part of the magnetic lead screw by Holm *et al.* [47]

(a) (b)

Fig. 1-28. a) Magnetic lead screw suspension system. b) Translator assembly procedure[49]

PMs in the non-active region of the MLS structure do not contribute to force production. Therefore, a low force per kg of PM material is expected for applications with long stroke lengths. Furthermore, the translator PMs need to slide on the surface of the linear bearings, which increases friction and wear. As the translator includes magnets that are exposed to the outside environment, they can attract ferromagnetic materials, which might cause corrosion of the magnets [50].

Lu *et al.* [51] proposed an electromagnetic lead screw (EMLS) by replacing the PM poles of the translator with a helical winding. In addition, they also added a PM generator around the rotor of this EMLS for potential wave energy application. Fig. 1-29 shows the structure of the proposed EMLS along with its winding configuration. Although replacing the translator PMs with windings might reduce the cost and the complexity of construction, the force production capability of the machine is degraded significantly due to the winding-related thermal limit.

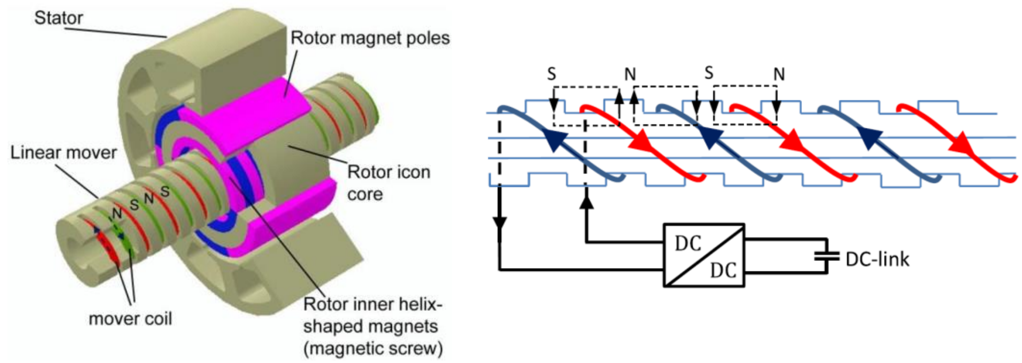

(a) (b)

Fig. 1-29. a) Lue's proposed electromagnetic lead screw. b) helical winding structure [51]

Integration of the MLS and a rotary PM machine has been investigated by Pakdelian *et al.* [52]. Pakdelian showed that for short stroke length applications, this integrated design resulted in a lower cost, more compact and lighter design when compared to a direct drive PM tubular machine. For applications with smaller force and longer stroke, however, this integration may lose its advantage over a PM tubular machine [52].

Ji *et al.* [53] proposed an integrated MLS with PM generator for use in an artificial heart. The PM poles on the MLS structure have a Halbach arrangement. The structure of the proposed machine is shown in Fig. 1-30. The MLS with Halbach arrangement of PM poles resulted in a 72% higher force capability when compared with radially-magnetized PM structure.

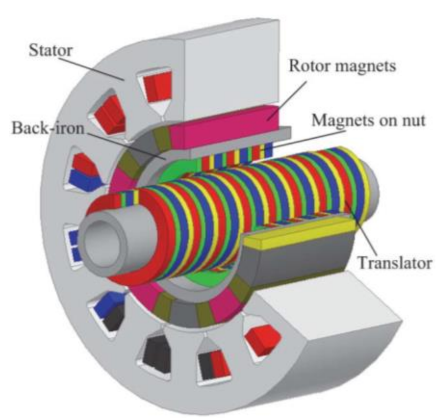


Fig. 1-30. PM machine integrated with a magnetic lead screw with Halbach pole arrangement [53].

Berg *et al.* [50] recently proposed a reluctance MLS for use in a wave energy converter, shown in Fig. 1-31. As the translator in the proposed design does not contain any magnet material, it can significantly reduce the cost of the MLS for long stroke length applications, but at the cost of reducing the output force. the shear force for this design was 88.4 kN/m$^2$.

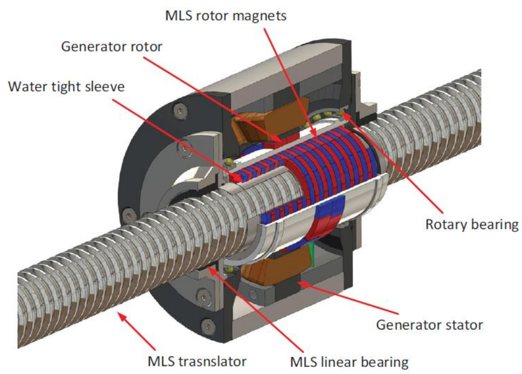


Fig. 1-31. Reluctance magnetic lead screw by Berg *et al.* [50]

### 1.2.6 Summary

Various linear actuators were investigated in this chapter. The advent of magnetic gear-based devices could have a considerable impact on the field of linear actuation. In order to compare the performance of all designs, a summary of the force production capabilities of the different linear actuators in different categories is given in Table 1-I.

Table 1-I. Performance Comparison of Various Linear Machines

| Structure | Geometry | | Force | | |
|---|---|---|---|---|---|
| | Cross section area [mm$^2$] | Axial length [mm] | Peak [kN] | Density (active) [kN/m$^3$] | Shear Stress [kN/m$^2$] |
| Hydraulic [54] | π×31.75×31.75 | 355.6 | 262.02 | 232.6×10$^3$ | 82.74×10$^3$ |
| Pneumatic [55] | π×31.75×31.75 | 220.66 | 13.1 | 18.74×10$^3$ | 4.13×10$^3$ |
| EMA [15] | 77.4×77.4 | 457 | 1.9 | 730 | - |
| DSLIM [21] | 250×1220 | 2440 | 11 | 16 | 18 |
| LSRM [23] | 148×185 | 100 | 0.16 | 58 | 8.6 |
| Tubular motor [56] | π×100×100 | 224 | 4.9 | 696 | 60 |
| Spiral motor [29] | 204×178 | 201 | 2 | 274 | 18 |
| LMG [43] | π×97×97 | 200 | 11.2 | 1.89×10$^3$ | 110 |
| MLS [47] | π×71×71 | 410 | 17 | 2.62×10$^3$ | 130 |

### 1.2.7 Problem Statement

Linear actuation is often achieved by using either a hydraulic or mechanical gearing mechanism. By operating a hydraulic actuator at high pressure, very high force densities can be sustained. ELAs have the advantage over hydraulic and mechanical mechanisms of being able to operate with higher efficiencies [8] and are potentially more reliable. However, the force density of an ELA is constrained by current density and magnetic saturation. Recently, the LMG and the MLS have been proposed as means for increasing the force densities of linear actuators. LMG and MLS rely only on magnetic loading and therefore a higher magnetic air-gap shear stress can be continuously sustained.

Both LMG and MLS topologies require one of the linear translating parts be made of magnet material. If the linear stroke length is large, then only a small portion of the magnet material will be used at any given time. Therefore, this will result in a low force-per-kilogram of magnet usage and consequently the design will be costly to build for a given outer radius. The LMG force density also becomes low when the linear stroke length is increased [43]. In the following chapter, a new type of magnetically geared linear actuator is proposed and investigated, that does not have PMs on the translator.

# 2 Chapter 2: Magnetically Geared Lead Screw

## 2.1 Introduction

In this chapter, a magnetically geared lead screw (MGLS) is proposed and investigated. The MGLS combines the operational concepts of the LMG and the MLS to overcome problems associated with these two designs. The MGLS is a rotary-to-linear actuator similar to the MLS, but it uses magnetic field modulation, like an LMG. In the following section, a small MGLS proof of concept is presented and analyzed. Then, in Section 2.3, a scaled-up design is investigated in order to show the force capability of the MGLS relative to comparable MLS. In order to experimentally test the MGLS, a small MGLS was designed and constructed. Detailed analysis and experimental results are given in Section 2.4. Lastly in Section 2.5, problems associated with the proposed MGLS are identified and a new version of the MGLS is proposed to resolve these issues.

## 2.2 Proof of Concept Design

### 2.2.1 Structural Characteristics

Fig. 2-1 shows the proposed MGLS and its cross-sectional parameters. The MGLS consists of three concentric tubular parts: an inner rotor with $p_i$ helically-skewed, radially-magnetized pole pairs; an outer cylinder with $p_o$ radially magnetized pole pairs; and, a translator that contains $n_t$ ferromagnetic annular skewed pole pieces. To maximize force, the pole combination was selected to satisfy:

$$n_t = p_i + p_o \quad (1.6)$$

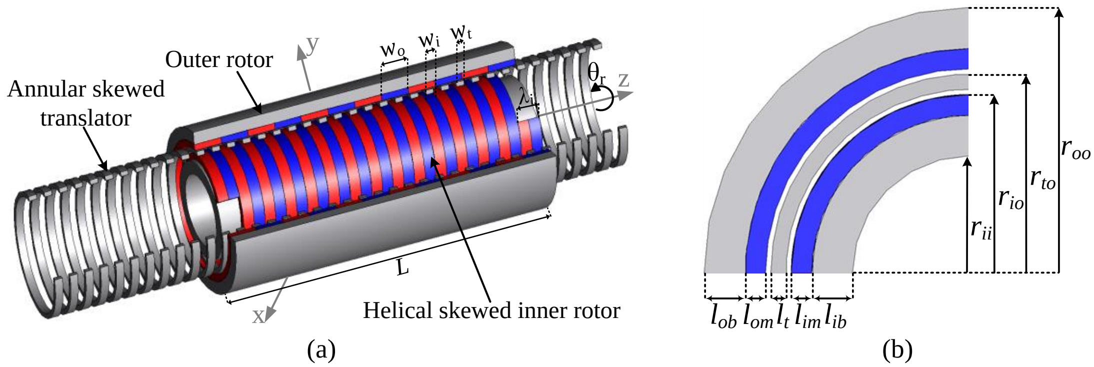


Fig. 2-1. MGLS proof of concept design; a) 3D view, b) cross-sectional parameters

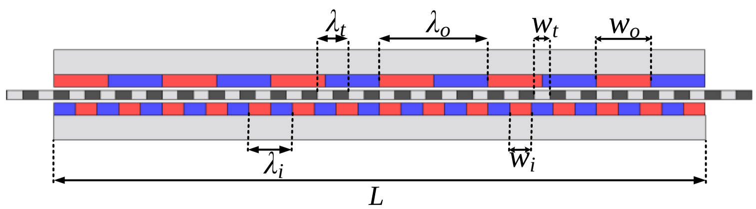


Fig. 2-2. Cut-through view of the magnetically geared lead screw showing the lead lengths for the inner outer and translator.

The required number of inner and outer pole-pairs and the translator pole-pieces must fit within the axial length, *L*. Therefore, the lead lengths, which are defined in Fig. 2-2, must satisfy the same equations as given for the LMG. These are:

$$\lambda_i = L / p_i \tag{1.10}$$

$$\lambda_o = L / p_o \tag{1.11}$$

$$\lambda_t = L / n_t \tag{1.12}$$

Based on these conditions, one then arrives at the following required pole-lead relationships:

$$\lambda_o p_o = \lambda_t n_t \tag{2.1}$$

$$\lambda_i p_i = \lambda_t n_t \tag{2.2}$$

Also using (1.10)-(1.12), the pole-pair requirement given by (1.6) can be expressed in terms of wavenumbers:

$$k_t = k_i + k_o \tag{2.3}$$

where

$$k_t = 2\pi/\lambda_t \tag{2.4}$$

$$k_o = 2\pi/\lambda_o \tag{2.5}$$

The amount of helical skew on the inner rotor is defined in terms of a lead angle. The lead angle is a function of the inner rotor outer radius, $r_{io}$, and lead length. Considering Fig. 2-3 the lead angle is

$$\alpha_i = \tan^{-1}[(\lambda_i / 2) / 2r_{io}] \tag{2.6}$$

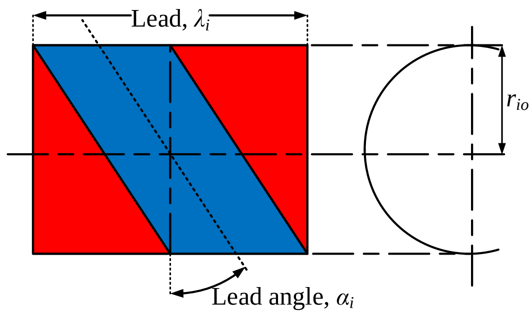


Fig. 2-3. Side view of the helical lines of the inner rotor

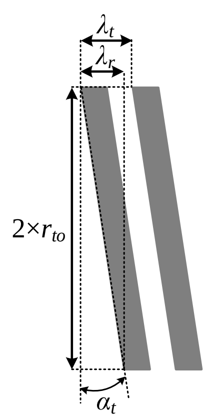


Fig. 2-4. Side view showing two consecutive skewed ferromagnetic translator rings. The definition for the translator rotor lead length $\lambda_r$ and translator lead $\lambda_t$ is also shown.

To create coupling between the translator and inner rotor, the translator rings are annularly skewed as shown in Fig. 2-4. In order to describe this skew, a translator skew angle was defined based on the ratio of a translator rotor lead, $\lambda_r$, and translator radius, $r_{to}$, such that:

$$\alpha_t = \tan^{-1}(\lambda_r / 2r_{to}) \tag{2.7}$$

These parameters are shown in Fig. 2-4. In order to convert the inner rotor torque to force, the translator angle was set equal to the inner rotor lead angle:

$$\alpha_t = \alpha_i \tag{2.8}$$

substituting (2.6) and (2.7) into (2.8) then gives:

$$\lambda_r = \frac{r_{to}}{2r_{io}} \tag{2.9}$$

This relates the translator rotor lead to the inner rotor lead. By substituting (2.2) into (2.9) the definition of the translator rotor lead, $\lambda_r$, can be related to the translator lead, $\underline{\lambda_t}$, by

$$\lambda_r = \frac{r_{to}}{2r_{io}} \frac{n_t}{p_i} \lambda_t \tag{2.10}$$

The difference in lead lengths is shown in Fig. 2-4.

### 2.2.2 Operational Characteristics

Under static conditions, the net force on the three MGLS parts must satisfy

$$F_t + F_i + F_o = 0 \tag{2.11}$$

where $F_i$ = inner rotor force, $F_t$ = translator force, $F_o$ = outer cylinder force. Due to the helical structure on the inner rotor and the translator annular skew, a torque is created on these two parts such that

$$T_i + T_t = 0 \tag{2.12}$$

where $T_i$ and $T_t$ are the torque on the inner rotor and translator respectively. The outer cylinder does not experience any torque since it is not skewed.

As the translator is subjected to both an applied torque and force it could undergo both translational and rotational motion. Both such situations are considered separately in the following sections. The inner rotor is connected to a rotary shaft and therefore unable to translate.

#### 2.2.2.1 Translator Case

The rotation of the MGLS inner rotor with angular velocity, $\omega_i$, will create a translational field velocity, $v_i$, given by:

$$\omega_i = k_i v_i \tag{1.13}$$

This translating field is modulated by the ferromagnetic translator pole pieces and therefore creates $z$-axis spatial harmonics. If (1.6) is satisfied, the spatial harmonics then interact with the outer cylinder's magnetic field. By substituting (1.13) into (1.9), one obtains:

$$n_t v_t = k_o v_o + \frac{p_i}{k_i}\omega_i \tag{2.13}$$

Equation (2.13) combines both the speed operating principals of the MLS and LMG. By substituting (1.10)-(1.12) into (2.13), the rotary conversion coefficients can be written in terms of lead lengths:

$$\omega_i = \frac{k_i \lambda_i}{\lambda_t} v_t - \frac{k_i \lambda_i}{\lambda_o} v_o \tag{2.14}$$

Noting that

$$k_i \lambda_i = 2\pi \tag{2.15}$$

And utilizing (2.4)-(2.5), equation (2.14) simplifies to:

$$\omega_i = k_t v_t - k_o v_o \tag{2.16}$$

If the outer cylinder is held fixed ($v_o = 0$), then:

$$\omega_i = k_t v_t \tag{2.17}$$

Equation (2.17) shows that the translational speed on the ferromagnetic rings is converted into an inner rotor rotary speed. If the translator wave number, $k_t$, is designed to be large, then this converts a low translational speed to high rotation speed. Importantly, the translator part is made entirely of low-cost ferromagnetic steel. Therefore, unlike the MLS and LMG, the translator stroke length can be long without requiring more magnet material.

#### 2.2.2.2 Oscillator Case

In deriving (2.17), the translator was assumed to be prevented from rotating. However, the inner rotor and translator both experience a torque. If the translator is only allowed to rotate (prevented for translating), the torque created by the inner rotor will cause the translator to rotate. This translator angular speed, $\omega_t$, is equal to the inner rotor angular speed such that

$$\omega_i = \omega_t \tag{2.18}$$

The rotation of the translator will create an oscillatory $z$-axis motion as illustrated in Fig. 2-5. The oscillatory motion of the translator is sinusoidal in form as shown by Fig. 2-6. The amount of axial displacement, $z_r$, is related to the translator rotor lead such that

$$z_r(\theta_t) = \frac{\lambda_r}{2}\cos(\theta_t) \tag{2.19}$$

where $\theta_t = \omega_t t$ is the translator angular position. Taking the derivative of (2.19), the translator ring linear speed due to the translator rotation is

$$v_r = -\frac{\lambda_r}{2}\omega_t \sin(\omega_t t) \tag{2.20}$$

This describes simple harmonic motion.

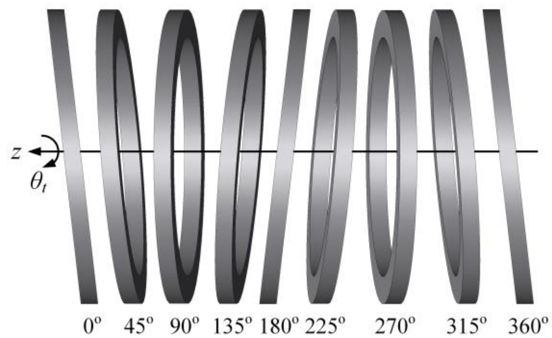


Fig. 2-5. One turn rotation of a translator ring (side view)

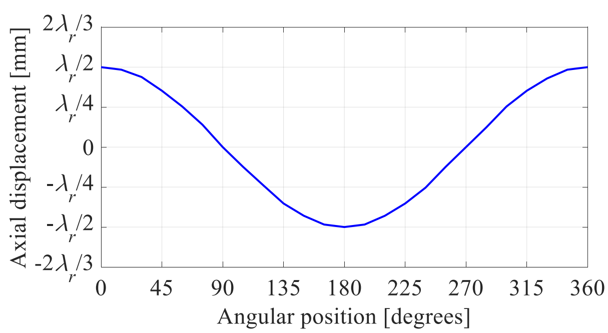


Fig. 2-6. Axial displacement of a translator ring as the function of translator angular position

#### 2.2.2.3 Power Conversion

If the translator is preventing from rotating, then the power flow relationship must satisfy

$$T_i\omega_i - F_t v_t = P_L \tag{2.21}$$

where $P_L$ is the electrical and mechanical losses. Substituting (2.17) into (2.21) and assuming the power loss is relatively small, one obtains

$$T_i k_t = F_t \tag{2.22}$$

If the translator lead is small, $k_t$ will be large. Equation (2.22) shows that a large force will be created from a small torque input.

### 2.2.3 Analysis and Results

The design parameters given in Table 2-I were selected to numerically verify the operating principal of the MGLS. Considering the geometric and material parameter values given in Table 2-I, the characteristics of the proposed MGLS were investigated using the 3D finite element analysis (FEA) by JMAG. The pole combination of ($p_i$ = 15, $n_t$ = 21, $p_o$ = 6) was selected to match with Li's work on a LMG [57].

The radial flux density due to the inner rotor PMs near the inner rotor and the outer rotor were evaluated. The results are shown in Fig. 2-7; the corresponding spatial harmonics, when the translator is present, is also shown. Fig. 2-8 shows the same plots when the PMs are only present on the outer rotor. The modulation effect of the translator is clearly evident.

Table 2-I. Summary of the Design Parameters

| **Parameter** | | **Value** | **Unit** |
|---|---|---|---|
| Outer rotor (fixed) – not skewed | Pole-pairs, $p_o$ | 6 | - |
| | Outer radius, $r_{oo}$ | 26 | mm |
| | Back iron, $l_{ob}$ | 4 | mm |
| | Pole-pitch, $w_o$ | 8.75 | mm |
| | Airgap length, $l_g$ | 0.5 | mm |
| | Axial length, $L$ | 105 | mm |
| Translator – annular skewed | Pole pieces, $n_t$ | 21 | |
| | Outer radius, $r_{to}$ | 19.5 | mm |
| | Steel thickness, $l_t$ | 1.5 | mm |
| | Pole-pitch, $w_t$ | 2.5 | mm |
| Inner rotor – helically skewed | Pole pairs, $p_i$ | 15 | - |
| | Inner radius, $r_{ii}$ | 11.5 | mm |
| | Outer radius, $r_{io}$ | 17.5 | mm |
| | Back iron, $l_{ib}$ | 4 | mm |
| | Magnet thickness, $l_{im}$ | 2 | mm |
| | Pole-pitch, $w_i$ | 3.5 | mm |
| | Lead, $\lambda_i$ | 7 | mm |
| Material | NdFeB magnet, Hitachi NMX-40CH | 1.25 | T |
| | 416 steel resistivity (translator) | 57.0 | μΩ-cm |
| | 1018 steel resistivity (back iron) | 15.9 | μΩ-cm |

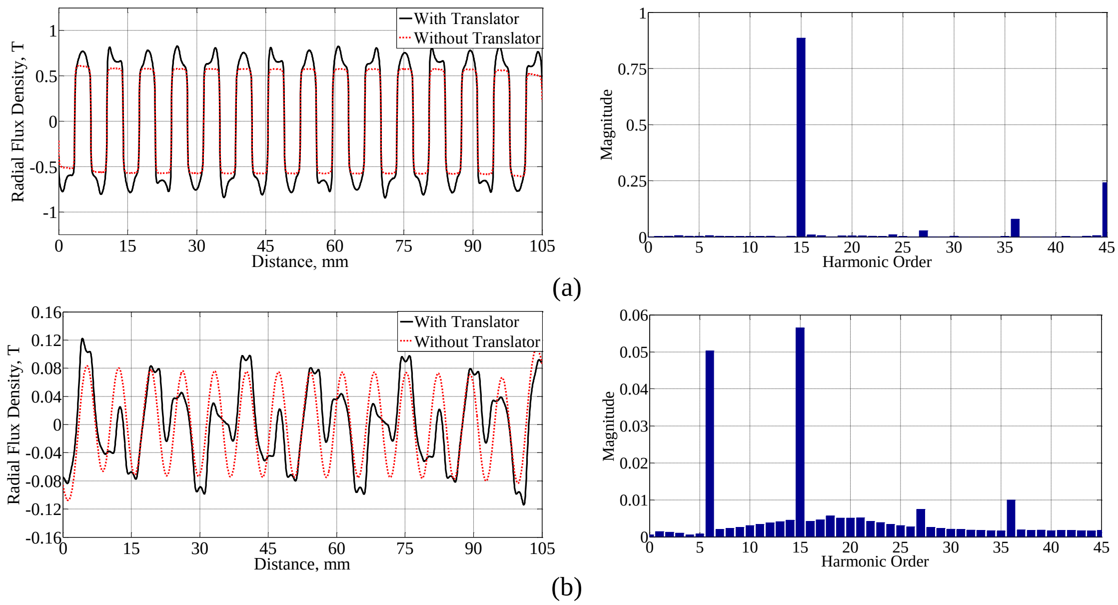


Fig. 2-7 Radial flux densities and related spectrums: a) adjacent to inner rotor due to inner rotor magnets at $r$=17.55 mm), b) adjacent to outer rotor due to inner rotor magnets (at $r$=19.95 mm).

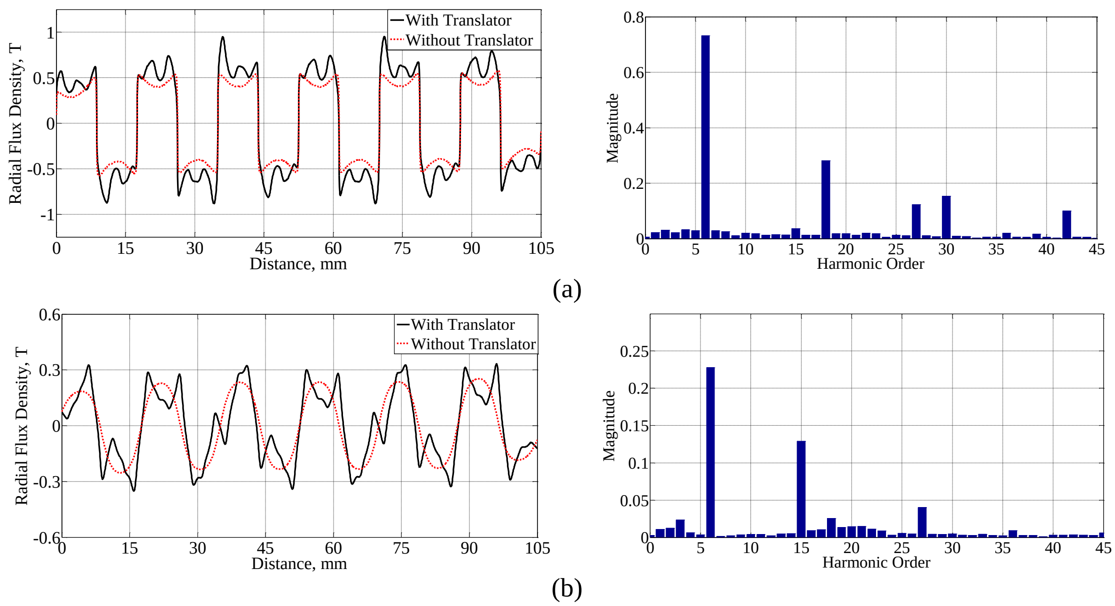


Fig. 2-8 Radial flux densities and related spectrums a) adjacent to outer rotor due to outer rotor (at $r$=19.95 mm), b) adjacent to inner rotor due to outer rotor (at $r$=17.55 mm)

When the inner rotor is rotated by 360$^o$ while the outer rotor and translator are kept stationary, an axial force along the $z$-axis is created as well as a torque. Fig. 2-9-a shows the calculated forces when using the parameters given in Table 2-I.

The torque on the MGLS components is shown in Fig. 2-9-b. Due to the helical structure of the inner rotor and the translator annular skew, a torque is created only on these two parts. The outer rotor does not experience any torque since it is not skewed.

The translator wave number is $k_t = 1256.6\ \text{m}^{-1}$, and so the torque is 1256.6 times smaller than the force. By having both rotation of the inner rotor and translation of the translator at the same time, a constant force in the *z*-direction is created. Fig. 2-10 shows the force and torque on the different parts when $\omega_i = 60$ r/min and $v_t = 5$ mm/s.

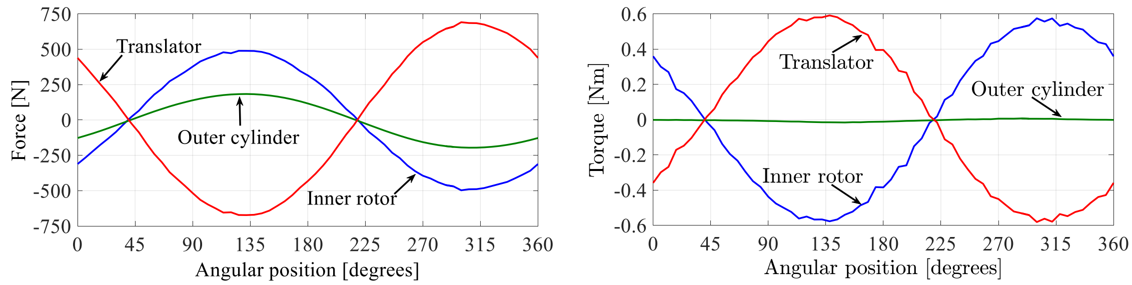


(a) (b)

Fig. 2-9. a) Force, and b) torque on different parts of the MGLS due to rotation of the inner rotor

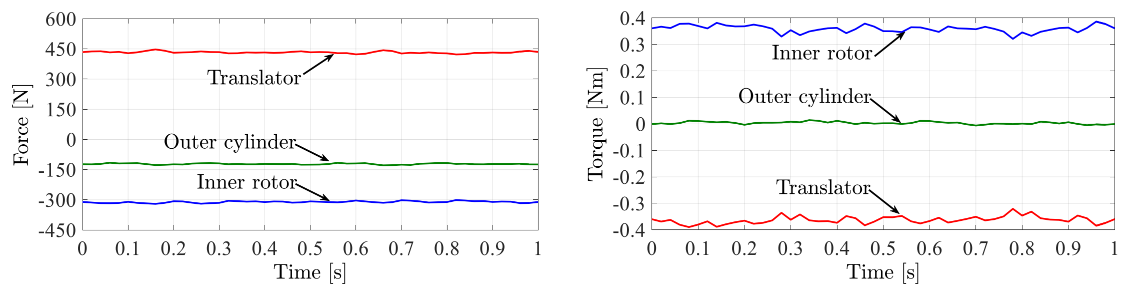


(a) (b)

Fig. 2-10. a) Force, and b) torque on different parts of the MGLS due to rotation of the inner rotor and translation of the translator at the same time

## 2.3 Comparative Design

In order to assess the performance of the MGLS relative to the LMG and MLS, a design analysis was conducted using the outer radial dimension, $r_{oo}$ = 71 mm, that was given in [47]. The same pole combination as that of the small MGLS is selected for this MGLS, which was $(p_i,p_o,n_t) = (6,15,21)$. With this pole combination, the axial length was selected as $L$ = 420 mm (rather than 410 mm as used in [47]). This results in integer lead lengths.

The translator wave number is then $k_t$ = 314 m$^{-1}$ and therefore in this design the force is amplified by 314 relative to the applied torque.

A 3D view of the scaled-up MGLS is shown in Fig. 2-11. The key structural difference between the previous design and the scaled-up design is that the outer cylinder pole-pairs in the scaled up design were arranged in a flux-focusing structure using axially-magnetized ring magnets and a ferromagnetic steel ring. The lead length definition for this design is illustrated in Fig. 2-12.

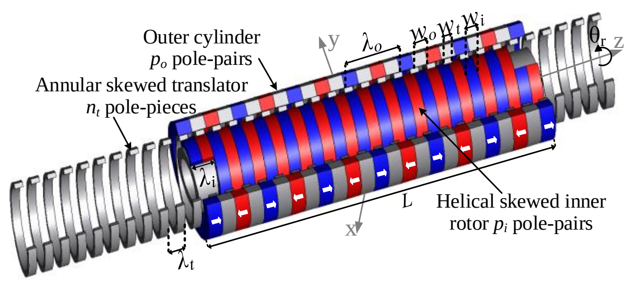


Fig. 2-11. Structure of the magnetically geared lead screw with $p_i$ =15 inner rotor pole-pairs, $p_o$ = 6 pole pairs and $n_t$ = 21 segments across the axial length.

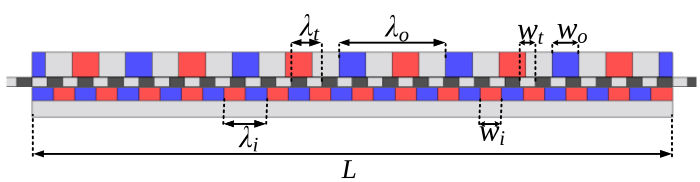


Fig. 2-12. Cut-through view of the magnetically geared lead screw showing the lead lengths for the inner outer and translator.

### 2.3.1 Design Analysis

A 3D finite element analysis (FEA) iterative parameter sweep analysis was used to design the MGLS. The objective was to maximize the active region volumetric force density, defined as:

$$V_{Fd} = F_t / (\pi r_{oo}^2 L) \tag{2.23}$$

Such a design approach was used because the simulation time for each design was very long. The inner rotor back iron was made sufficiently thick so as to avoid saturation. As the geometric parameters are interrelated, only three radial parameters are used to describe the radial geometry. They are the inner radius of inner rotor, $r_{ii}$; outer radius of inner rotor, $r_{io}$; and translator outer radius, $r_{to}$, as shown in Fig. 2-13. The other geometric parameters, given in Table 2-II, were fixed. In iteration I, $r_{ii}$ was fixed (48 mm) and through a parametric sweep of $r_{io}$ and $r_{to}$ a peak force density was determined to occur at ($r_{io}$, $r_{to}$) = (53, 58.5) mm. In iteration II the iteration I, values were fixed and a parametric sweep for $r_{ii}$ was performed. The results are shown in Table 2-III. The peak force density is achieved at $r_{ii}$ = 45.5 mm. This iterative procedure was repeated until no significant improvement was obtained.

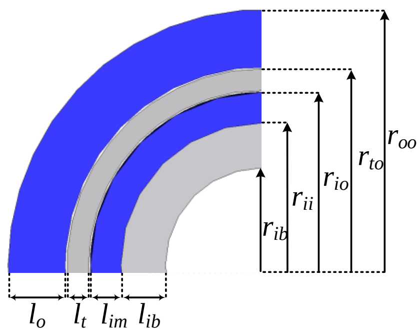


Fig. 2-13. Cross-sectional dimensional parameters.

Table 2-II. Scaled-up Design; Fixed Geometric and Material Values

| **Parameter** | | **Value** | **Unit** |
|---|---|---|---|
| Outer cylinder (fixed) - not skewed | Pole-pairs, $p_o$ | 6 | - |
| | Outer radius, $r_{oo}$ | 71 | mm |
| | Pole-pitch, $2w_o$ | 33.6 | mm |
| | Airgap length, $l_g$ | 0.5 | mm |
| | Axial length, $L$ | 420 | mm |
| Translator - annular skewed | Pole pieces, $n_t$ | 21 | - |
| | Pole-pitch, $w_t$ | 10 | mm |
| | Translator lead, $\lambda_t$ | 20 | mm |
| Inner rotor - helically skewed | Pole pairs, $p_i$ | 15 | - |
| | Back iron, $l_{ib}$ | 11 | mm |
| | Pole-pitch, $w_i$ | 14 | mm |
| | Lead, $\lambda_i$ | 28 | mm |
| Material | NdFeB magnet, $B_r$, NMX-40CH | 1.25 | T |
| | 416 steel resistivity (translator) | 57.0 | μΩ-cm |
| | 1018 steel resistivity (inner, outer rotors) | 15.9 | μΩ-cm |

The parametric sweep values for the last two iterations are depicted in Fig. 2-14 and Fig. 2-15. Fig. 2-15 shows that a trade-off exists between maximizing mass and volumetric force density. The maximum force and force density are 12.46 kN and 1.87 kN/L, respectively.

Table 2-III. Iteration of the radial parameters of the scaled-up MGLS

| Iteration number | | I | II | III | IV | V | VI | Unit |
|---|---|---|---|---|---|---|---|---|
| Inner rotor | Outer radius, $r_{io}$ | 53 | 53 | 51 | 51 | 48 | 48 | mm |
| | Inner radius, $r_{ii}$ | 48 | 45.5 | 45.5 | 42 | 42 | 39.5 | mm |
| Translator outer radius, $r_{to}$ | | 58.5 | 58.5 | 57.5 | 57.5 | 54.5 | 54.5 | mm |
| Translator bar thickness, $l_t$ | | 5 | 5 | 6 | 6 | 6 | 6 | mm |
| Outer cylinder inner radius $r_{oi}$ | | 59 | 59 | 58 | 58 | 55 | 55 | mm |
| Translator force, $F_t$ | | 11.6 | 11.8 | 12.1 | 12.2 | 12.4 | 12.5 | kN |
| Volumetric force density | | 1.74 | 1.78 | 1.81 | 1.84 | 1.86 | 1.87 | kN/L |
| Force-per-kg magnet, $F_{ko}$ | | 0.88 | 0.76 | 0.86 | 0.71 | 0.78 | 0.69 | kN/kg |

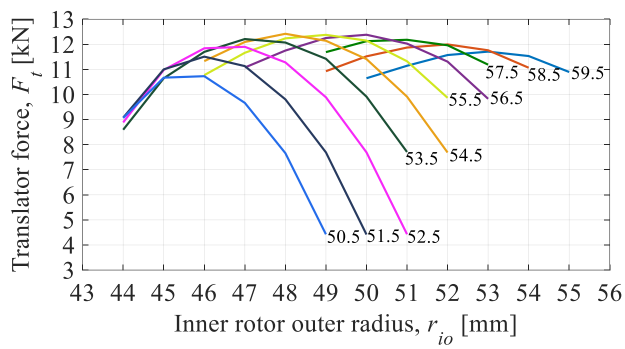


Fig. 2-14. Translation force as a function of inner rotor outer radius, $r_{io}$ and translator outer radius $r_{to}$ for iteration V. The curves for different $r_{to}$ are shown on the figure.

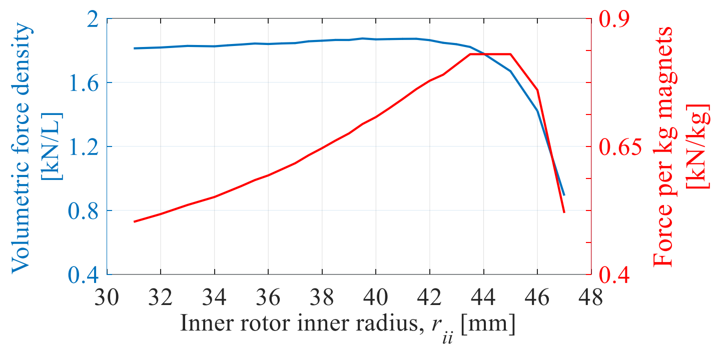


Fig. 2-15. The trade-off between maximizing volumetric force density and force-per-kg of magnet for iteration VI when ($r_{io}$ , $r_{to}$ ) = (48,54.5) mm.

### 2.3.2 Operational Analysis

Using the values given in Table 2-II and Table 2-III, the radial flux density due to the outer cylinder PMs near the inner rotor has been evaluated. The results are shown in Fig. 2-16. The corresponding spatial harmonics, when the translator is present, are also shown in this figure. Fig. 2-17 shows the same type of plots for the outer airgap when only the PMs are present on the inner rotor. The harmonic analysis plots given in Fig. 2-16 and Fig. 2-17 show how the necessary 15$^{th}$ and 6$^{th}$ harmonics are created by the translator modulation effect. Fig. 2-18 shows the field in the outer air-gap when the magnets are present in both the inner and outer rotors. The high 6$^{th}$ harmonic flux density present in the air-gap, relative to the ELA designs [58], is apparent.

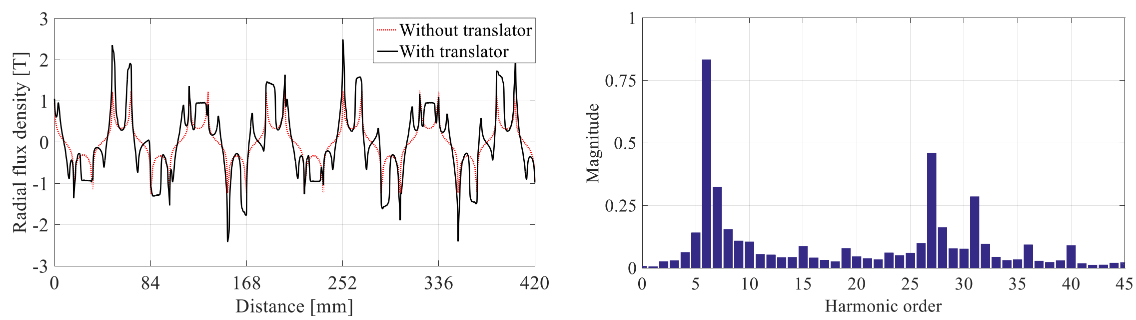


(a)

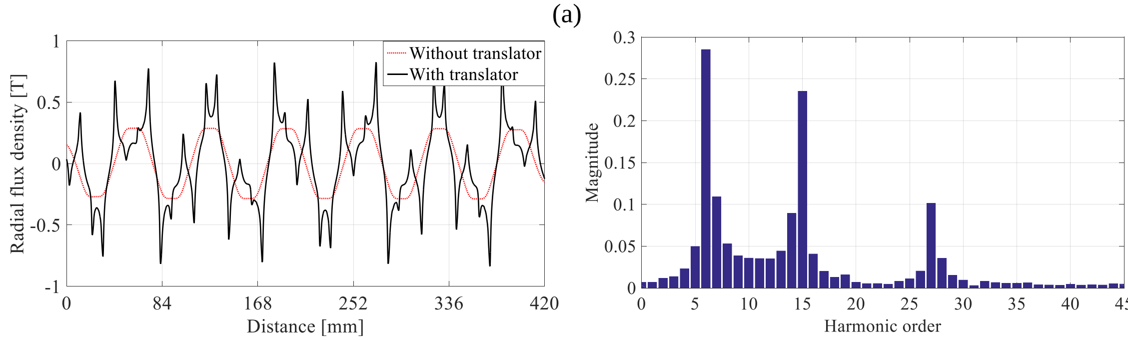


(b)

Fig. 2-16. Radial flux densities and related spectrums a) adjacent to outer rotor due to outer rotor (at $r$=54.9 mm), b) adjacent to inner rotor due to outer rotor (at $r$=48.1 mm)

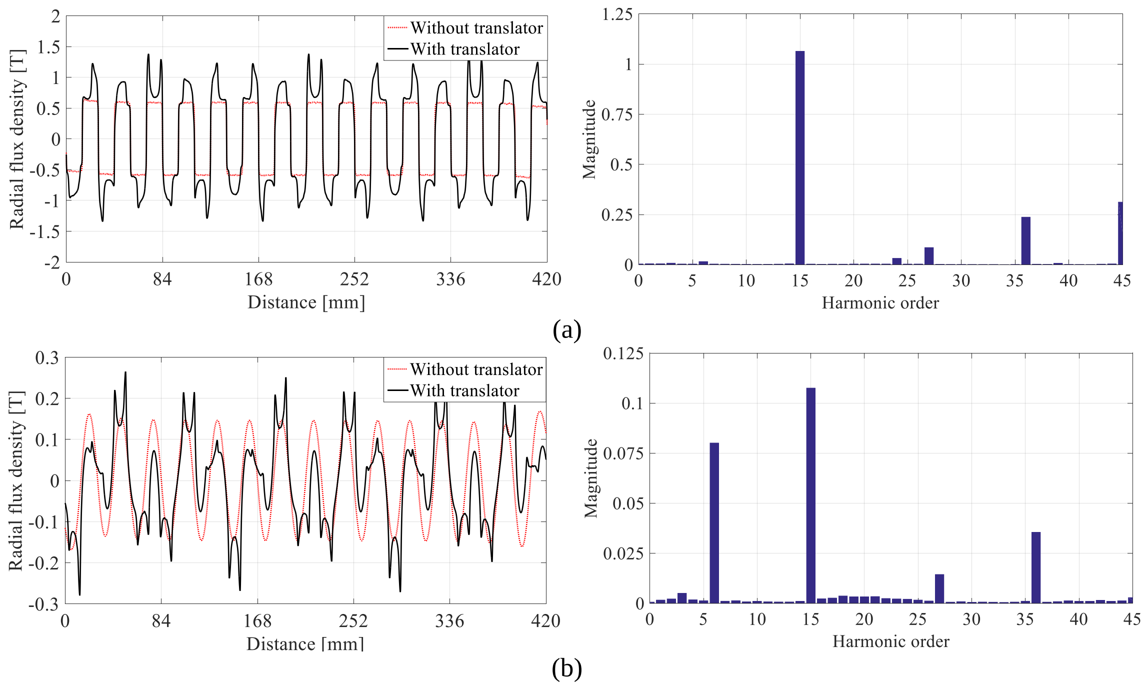


Fig. 2-17. Radial flux densities and related spectrums: a) adjacent to inner rotor due to inner rotor magnets at $r$=48.1 mm), b) adjacent to outer rotor due to inner rotor magnets (at $r$=54.9 mm).

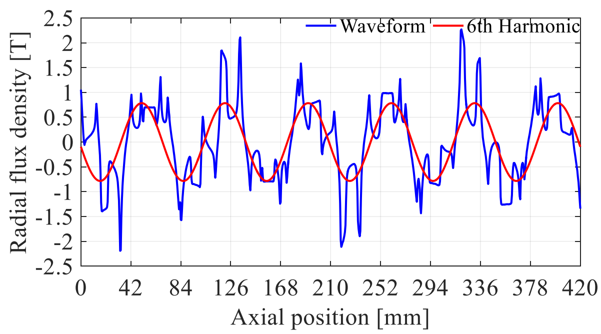


Fig. 2-18. Radial flux density in the outer air-gap due to magnets on both the inner and outer rotor.

When the inner rotor is rotated by 360° while the outer cylinder and translator are kept stationary, an axial force along the *z*-axis is created as well as a torque. Fig. 2-19 shows the calculated pole slippage force and torque when using the final design parameters.

When the rotor speed is $\omega_i$ = 150 r/min and the translator speed is $v_t$ = 50 mm/s, the torque and force were calculated on the presented MGLS using 3D FEA. The resulting torque and force values are shown in Fig. 2-20. An applied torque of only 39.7 Nm creates 12.46 kN force on the translator. The presented design also exhibits very low torque ripple.

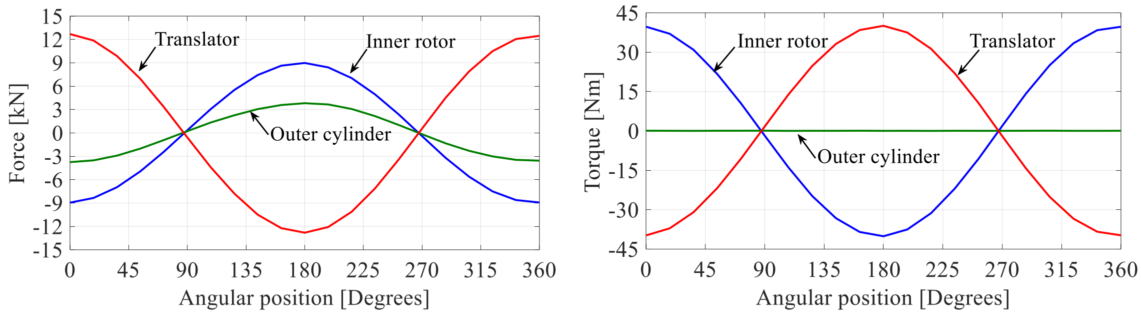


(a) (b)

Fig. 2-19. a) Force, and b) torque on different parts of the MGLS due to rotation of the inner rotor

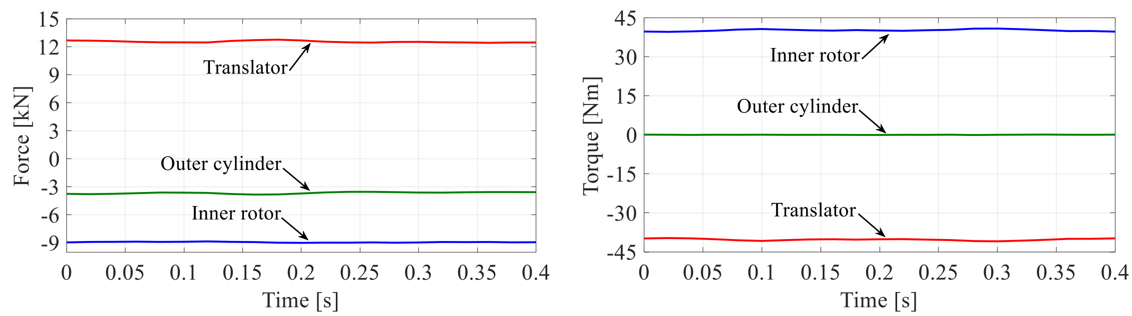


(a) (b)

Fig. 2-20. a) Force, and b) torque on different parts of the MGLS due to rotation of the inner rotor and translation of the translator at the same time

Fig. 2-21 shows the variation of the force per magnet volume as a ratio of stroke length, $L_s$, to the active length, $L_a$, for the MGLS in comparison to the MLS and LMG. The geometric and material properties provided in [43] and [47] were used to model the LMG and MLS performance. Fig. 2-21 shows that the proposed MGLS has a higher force per magnet volume for all stroke lengths compared to the LMG, and for long stroke lengths compared with the MLS. The force capabilities for the LMG and MLS are summarized in Table 2-IV. The translator used by the LMG and MLS are composed of both magnets and a back-iron to support the magnet flux path. This back-iron adds significantly more mass to the translator. The last row in Table 2-IV shows the added ferromagnetic and magnet mass per centimeter of stroke length for each device. The MGLS translator mass is significantly lower.

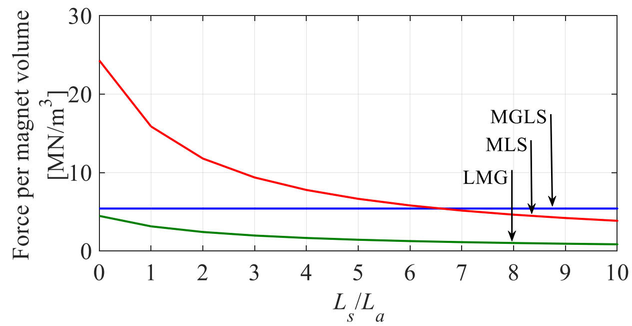


Fig. 2-21. Force per magnet volume as a function of $L_s/L_a$

Table 2-IV. Comparison of the force capabilities

| **Design** | | **MGLS** | **LMG** | **MLS** |
|---|---|---|---|---|
| Reference | | - | [43] | [47] |
| Thrust force [kN] | | 12.5 | 11.2 | 17 |
| Force per active volume [MN/m$^3$] | | 1.87 | 1.89 | 2.61 |
| Force per magnet volume [MN/m$^3$] | $L_s/L_a$ = 1 | 5.4 | 3.1 | 15.8 |
| | $L_s/L_a$ = 7 | 5.4 | 1.1 | 5.1 |
| Added weight per cm of stroke [g] | | 84.9 | 724 | 134 |

## 2.4 Prototype Design

In this section, a scaled down MGLS is designed, analyzed and constructed. Through a parametric sweep analysis, the geometric parameters are selected. The experimental results is presented

### 2.4.1 Design Analysis

In order to make a prototype, a small MGLS was designed with an axial length of $L$=120 mm, and an outer radius of $r_{oo}$=40 mm. A summary of the initial geometric parameters used is given in Table 2-V. The same material properties as shown in Table 2-II were used. Using the initial values shown in Table 2-V, the parametric sweep analysis was used to maximize the volumetric force density. A summary of the results when using this iterative method is given in Table 2-VI. The maximum force density for this design was determined to be 3.13 kN/L (iteration IV).

Table 2-V. Prototype Designs Geometric Parameters

| Parameter | | Initial Value | Prototype Values | Unit |
|---|---|---|---|---|
| Outer cylinder (fixed) | Pole-pairs, $p_o$ | 6 | 6 | - |
| | Outer radius, $r_{oo}$ | 40 | 40 | mm |
| | Pole-pitch, $2w_o$ | 9.6 | 9.6 | mm |
| | Airgap length, $l_g$ | 0.5 | 0.5 | mm |
| | Axial length, $L$ | 120 | 120 | mm |
| Translator | Pole pieces, $n_t$ | 21 | 16 | - |
| | Pole-pitch, $w_t$ | 2.8571 | 3.75 | mm |
| Inner rotor -helically skewed | Pole pairs, $p_i$ | 15 | 10 | - |
| | Pole-pitch, $w_i$ | 4 | 6 | mm |
| | Lead, $\lambda_i$ | 8 | 12 | mm |
| Wavenumber, $k_t$ | | 1099.5 | 837.75 | $m^{-1}$ |

Table 2-VI. Iteration of Radial Parameters

| Iteration number | | 0 | I | II | III | IV | V | $V_p$ | Unit |
|---|---|---|---|---|---|---|---|---|---|
| Inner rotor | Outer radius, $r_{io}$ | 31 | 31 | 31 | 30 | 30 | 30 | 26 | mm |
| | Inner radius, $r_{ii}$ | 29 | 29 | 25 | 25 | 22 | 22 | 20 | mm |
| Translator outer radius, $r_{to}$ | | 37.5 | 33.5 | 33.5 | 32.5 | 32.5 | 32.5 | 32.5 | mm |
| Translator bar thickness, $l_t$ | | 6 | 2 | 2 | 2 | 2 | 2 | 6 | mm |
| Outer rotor inner radius $r_{oi}$ | | 38 | 34 | 34 | 33 | 33 | 33 | 33 | mm |
| Translator force, $F_t$ | | 0.76 | 1.76 | 1.84 | 1.85 | 1.88 | 1.88 | 1.06 | kN |
| Volumetric force density | | 1.1 | 2.92 | 3.06 | 3.07 | 3.13 | 3.13 | 1.82 | kN/L |
| Force-per-kg magnet, $F_{ko}$ | | 1.15 | 1.75 | 1.14 | 1.2 | 0.97 | 0.97 | 0.84 | kN/kg |

Fig. 2-22 shows a trade-off between maximizing volumetric force density and force-per-kg of magnet materials as a function of inner rotor inner radius for iteration IV. The translation force as a function of $r_{io}$ and $r_{to}$ for iteration V is plotted in Fig. 2-23.

In order to handle the mechanical force on the translator rings, it is desirable to have enough radial thickness. Therefore, a design with proper translator radial thickness (6 mm) was selected instead of the best design achieved (iteration $V_p$ in Table 2-VI).

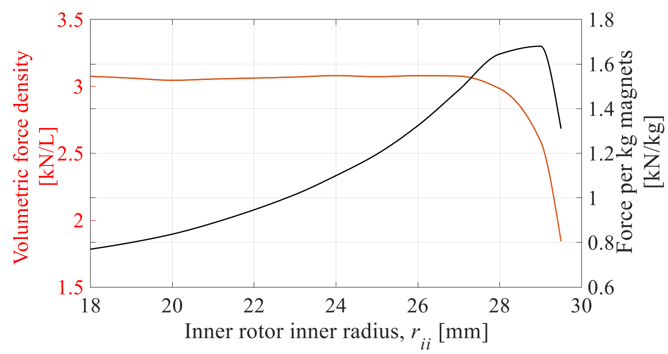


Fig. 2-22. Trade-off between maximizing volumetric force density and force-per-kg of magnet material. Results shown for iteration IV

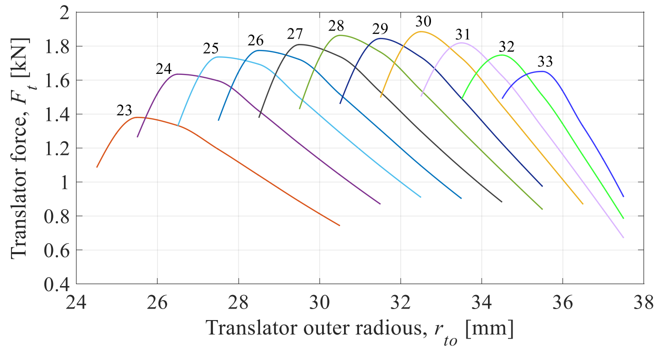


Fig. 2-23. Translation force as a function of translator outer radius, $r_{to}$ and inner rotor outer radius $r_{io}$ for iteration V

In order to make the construction of the helical inner rotor using commercially available blocks of magnets, a segmented helix structure was used. Such an approach was also used for some MLS designs [59]. Fig. 2-24 shows one turn of the inner rotor helix using different numbers of magnet segments. Each helix turn is formed by $n$ magnet segments displaced axially with respect to the adjacent segments. The amount of magnet segment axial shift, $L_{sh}$, depends on the axial thickness of each piece, $w_i$, as well as the number of magnet segments, $n$, in one helix turn. Therefore, the axial shift is defined as:

$$L_{sh} = w_i / (n/2) \tag{2.24}$$

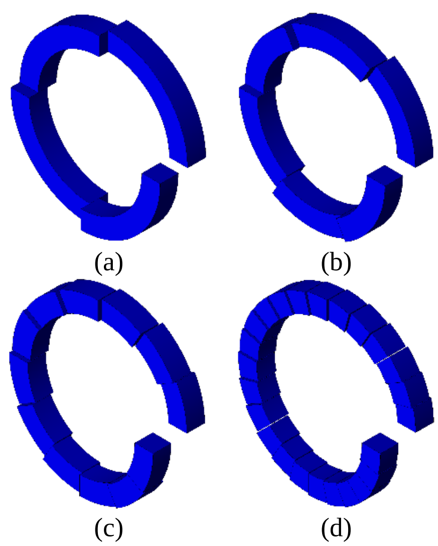


Fig. 2-24. One turn of the inner rotor helix using a) 4, b) 6, c) 12, and d) 24 magnet segments

Considering the axial length of $L$=120 mm and having $p_i$ = 15 inner rotor pole-pairs, the axial thickness of these magnet segments would need to be $w_i = L/(2p_i) = 4$ mm, which is too thin. This magnet thickness will cause two problems from a practical point of view; first the thin magnets are likely to break easily, and second, as the magnets must be axially shifted with respect to their adjacent magnets, the small magnet thickness means that the axial shift is less than 1 mm and this makes it difficult to align the magnets in their correct position. Therefore due to these issues and time limits related to the project, the pole-pair combination was changed from ($p_i$, $p_o$, $n_t$) = (15, 6, 21) to ($p_i$, $p_o$, $n_t$) = (10, 6, 16). This enables the axial thickness of each magnet to be increased to $w_i$ = 6 mm. The $k_t$ value then becomes 837.75 m$^{-1}$.

Fig. 2-25 shows the inner rotor torque and translator force for the different numbers of magnet segments. As predicted, higher numbers of magnet pieces per helix turn results in a better approximation of the helical structure, which in turn results in more sinusoidal torque and force curves. Based on (2.24) however, a higher number of segments will result in smaller amount of axial shift and also a smaller segment arc length, which make the design more difficult to fabricate. In addition, as can be seen from Fig. 2-25-b, increasing the number of segments does not significantly increase the translator force.

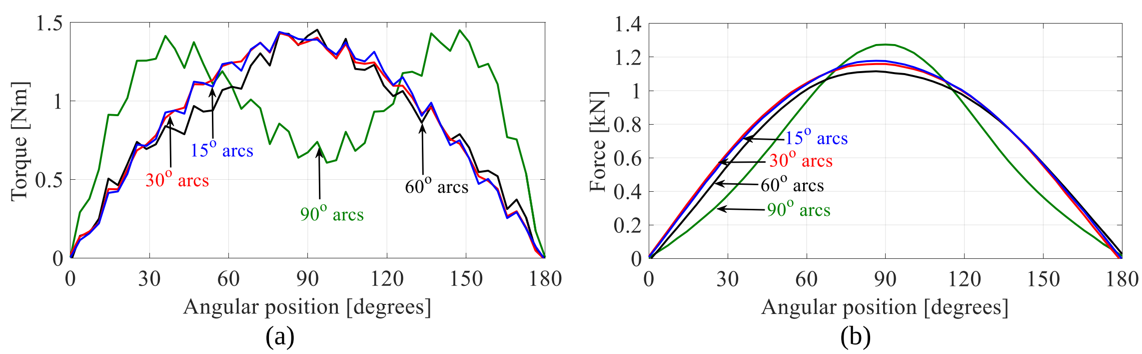


Fig. 2-25. a) Torque, and b) force when the inner rotor was rotated by 180 degrees for various designs with different inner rotor magnet arc length

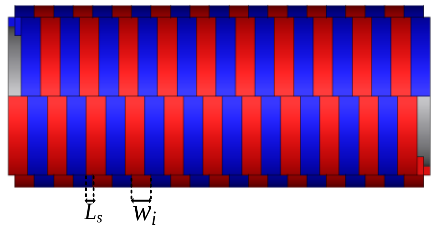


Fig. 2-26. Side view of the segmented helical inner rotor with 60° magnet arcs

Therefore, in the proposed MGLS, 6 segments were considered for each helix turn of the inner rotor, which corresponds to a 60° magnet arc, and an axial shift of $L_s$ = 2 mm. Fig. 2-26 shows the side view of the segmented helical inner rotor with 6 segments per helix turn. In order to avoid using a thin piece of magnet at both axial ends, which are difficult to fabricate, the rotor back-iron was extended by 5 mm on both sides, and the magnets with the same size were used at the ends. The final prototype values for the MGLS are summarized in Table 2-V on page 43.

### 2.4.2 Simulation Results

Using the final values of the parametric sweep given in Table 2-VI and applying the practical changes outlined above, a 3D FEA model of the MGLS was investigated. Rotation of the inner rotor while the other two parts of the MGLS were kept stationary created an axial force and torque on different parts. Fig. 2-27 shows the calculated pole slippage force and torque on the different parts.

Rotation of the inner rotor at 80 r/min and translating the translator at 10 mm/s creates a constant force and torque. Fig. 2-28 shows the calculated force and torque on different parts. The peak force is about 840 times larger than the torque due to the magnetic gearing. The segmentation of the inner rotor created some torque and force ripple.

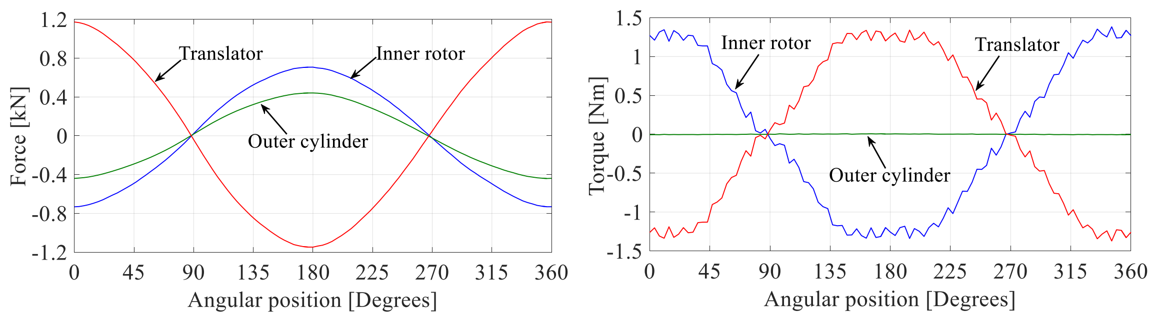


(a) (b)

Fig. 2-27. a) Force, and b) torque on different parts of the MGLS due to rotation of the inner rotor

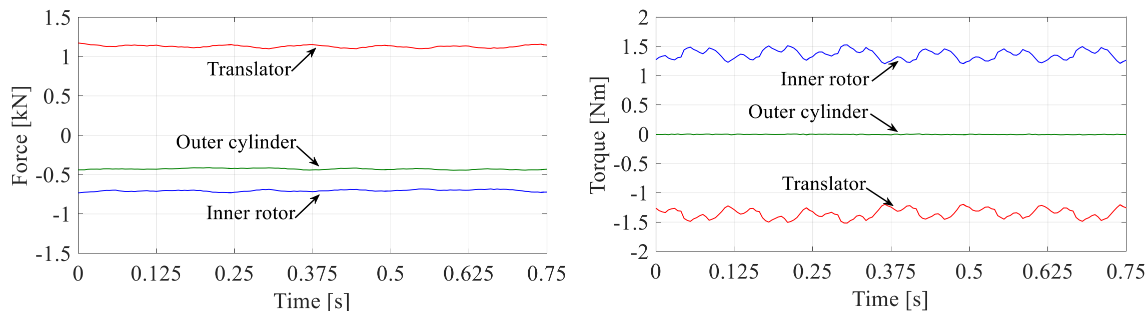


(a) (b)

Fig. 2-28. a) Force, and b) torque on different parts of the MGLS due to rotation of the inner rotor and translation of the translator at the same time

### 2.4.3 Experimental Results

The numerically-modelled MGLS prototype presented in section 2.4.1 was constructed. The assembled inner rotor and translator are shown in Fig. 2-29. Fig. 2-30 shows the MGLS on the test bed before connecting to the electromechanical actuator load.

(a) (b)

Fig. 2-29. a) Inner rotor and b) translator for the MGLS.

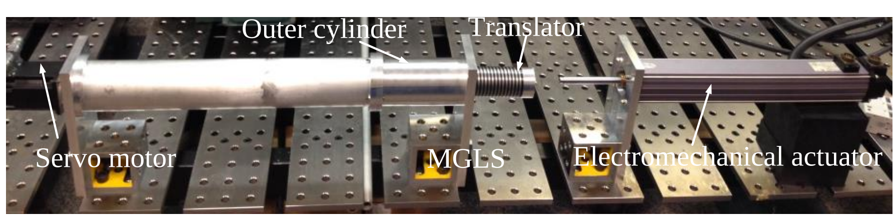


Fig. 2-30. The MGLS on the testbed before testing.

The radial flux density at the surface of the inner rotor and outer cylinder was measured using a Gaussmeter. Measurements were compared with the FEA results. Fig. 2-31 show the flux density of the inner rotor and outer cylinder. A good agreement was obtained.

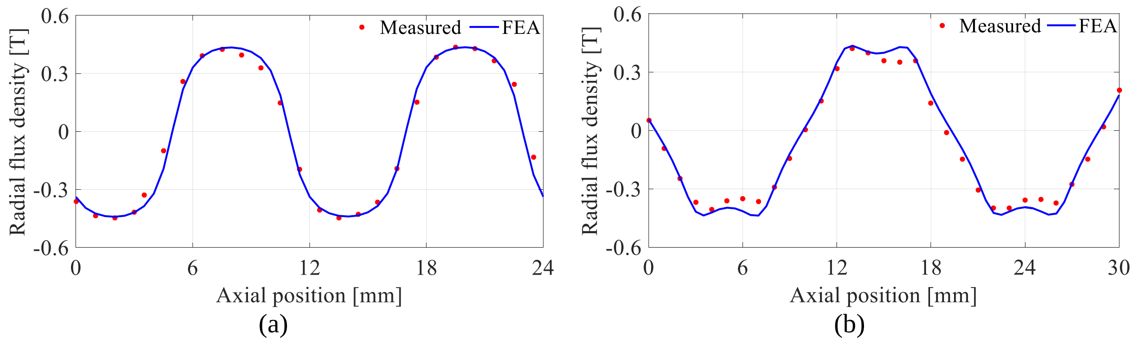


Fig. 2-31. Radial flux density along z-axis at radial distance of 0.85 mm from the surface of the a) inner rotor and b) outer cylinder

The inner rotor of the assembled MGLS was rotated manually by 90 degrees while the translator was kept stationary. Using a FUTEK load cell, the force on the translator was measured (Fig. 2-32). Fig. 2-33 shows the measured force on the translator compared with the calculated force using FEA. The measured force is considerably lower than the calculated force.

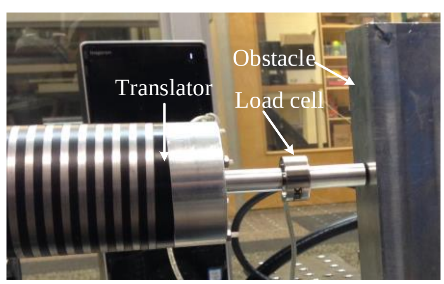


Fig. 2-32. Translator force measurement using a load cell when it was pushing against an obstacle.

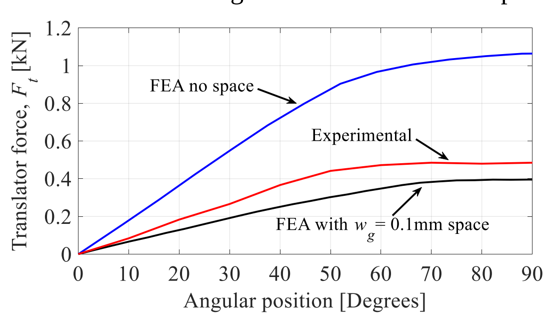


Fig. 2-33. Measured and calculated translator force with and without 0.1 mm space between rings.

The force capability of the MGLS is extremely sensitive to the space between ferromagnetic pole-pieces of the translator. As the steel and plastic rings of the translator were held together using just four Delrin rods, and due to manufacturing tolerances, small spaces between the translator rings were present. An FEA tolerance sensitivity analysis was performed to calculate the effect of having different spaces between translator rings. A small space of just $w_g$ =0.1 mm was considered, as shown in Fig. 2-34. Fig. 2-35 shows that a 2.6% increase in the space between the steel rings resulted in a 60% reduction in the thrust force. Such a sensitivity to tolerance was previously seen to exist for LMGs [43]. This sensitivity to tolerance must be carefully taken into account when designing the translator.

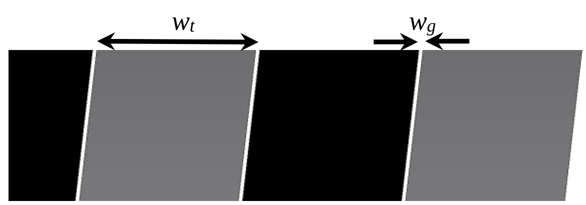


Fig. 2-34. Close up view (not to scale) of the translator pole-pieces and $w_g$ = 0.1 mm space between plastic (black) and steel rings (gray).

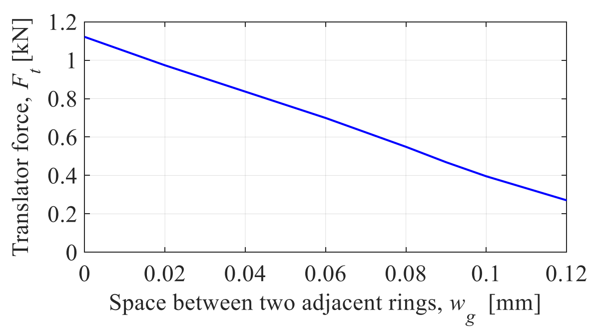


Fig. 2-35. Variation of the translator force as a function of space between two adjacent rings

### 2.4.4 Lead Angle

In the above analysis, the inner rotor lead angle was defined as shown by (2.6), which was based on the approximate side view of the helical shaped magnets of the inner rotor. This method of defining the lead was also presented by Lu *et al.* [60].

$$\alpha_i = \tan^{-1}[(\lambda_i / 2) / (2r_{io})] \tag{2.6}$$

After further study, it was determined that using the standard mechanical definition of the lead angle of a helix to determine the translator rings skew angle results in a higher force for the MGLS.

Based on the ANSI/AGMA Standard (1012-G05), the lead angle is defined as the angle between the helix and a plane of rotation [61], as illustrated in Fig. 2-36. The inner rotor lead angle is defined as:

$$\alpha_i = \tan^{-1}[\lambda_i / (2\pi r_{io})] \tag{2.25}$$

Substituting (2.25) and (2.7) into (2.8) gives

$$\lambda_r = \frac{r_{to}}{\pi r_{io}} \lambda_i \tag{2.26}$$

Table 2-VII shows that selecting the translator lead angle based on (2.25), the ANSI mechanical standard, rather than the definition provided by (2.6) results in higher translator force. Therefore, future MGLS designs should meet the lead condition given by (2.26).

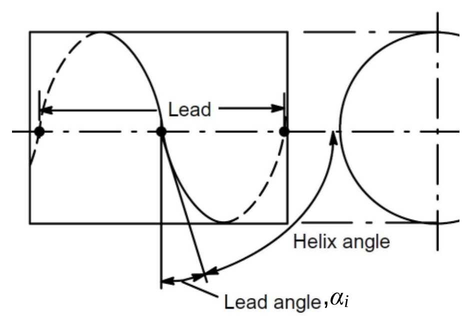


Fig. 2-36. Definition of the lead angle per ANSI/AGMA 1012-G05 [61]

Table 2-VII. Impact of Inner Rotor Lead Angle on Force

| Lead Definition | Lead angle [degrees] | $F_{tmax}$ [N] |
|---|---|---|
| Presented experimental design | 6.58 | 1060 |
| ANSI/AGMA 1012-G05 | 4.20 | 1512 |

## 2.5 MGLS without Translator Skewing

As discussed in Section 2.4.3, small tolerance inaccuracies in the rings cause the force to reduce significantly when compared to the predicted values. The skewing of the translator rings also significantly increases the manufacturing cost of the MGLS, as it is difficult to fabricate the skewed rings to a high tolerance. In this section, a new type of MGLS is presented that does not require the use of skewed translator rings, therefore significantly reducing the translator construction cost.

### 2.5.1 Design Analysis

The translator rings in the new design are not skewed. However, in order to create field coupling with the inner rotor, the outer cylinder poles need to be skewed instead. Consider the schematic shown in Fig. 2-37. The outer cylinder can be skewed by axially shifting a half-ring (180°) of the magnet and ferromagnetic steel by distance $L_a$.

Using the geometric and material parameters given in Table 2-VIII, force as a function of axial shift, $L_a$, is calculated and shown in Fig. 2-38. The peak translator force $F_t$ = 1444 N occurs at $L_a$ = 9 mm. However, if the half ring outer rotor is shifted by $L_a$ =9.6 mm, then this equals the outer cylinder pole-pitch ($2w_o$) and the peak translator force only reduces by 0.4% to $F_t$ = 1435 N.

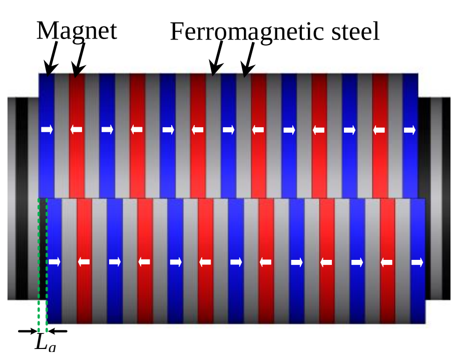


Fig. 2-37. Parametric design to investigate the effect of the axial shift, $L_a$, between the top and bottom set of half rings

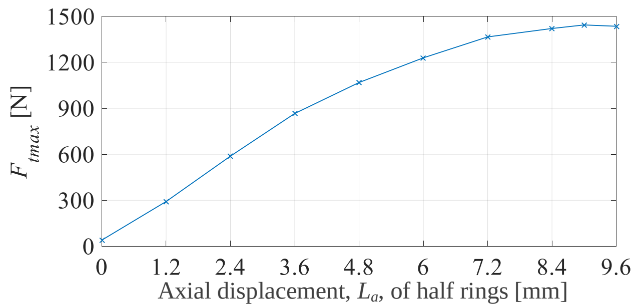


Fig. 2-38. Maximum translator force versus axial shift, $L_a$ of the half rings

Table 2-VIII. Geometric and material parameters

| **Parameter** | | **Value** | **Unit** |
|---|---|---|---|
| Outer cylinder (fixed) | Pole-pairs, $p_o$ | 6 | - |
| | Outer radius, $r_{oo}$ | 40 | mm |
| | Pole-pitch, $2w_o$ | 9.6 | mm |
| | Airgap length, $l_g$ | 0.5 | mm |
| | Axial length, $L$ | 120 | mm |
| Translator rings | Ferromagnetic pieces, $n_t$ | 16 | - |
| | Outer radius, $r_{to}$ | 32.5 | mm |
| | Radial thickness, $l_t$ | 6 | mm |
| | Pole-pitch, $w_t$ | 3.75 | mm |
| Inner rotor<br>- helically skewed | Pole pairs, $p_i$ | 10 | - |
| | Outer radius, $r_{io}$ | 26 | mm |
| | Pole-pitch, $w_i$ | 6 | mm |
| | Lead, $\lambda_i$ | 12 | mm |
| Material | NdFeB magnet, $B_r$, NMX-40CH | 1.25 | T |
| | 1018 steel resistivity | 15.9 | µΩ-cm |

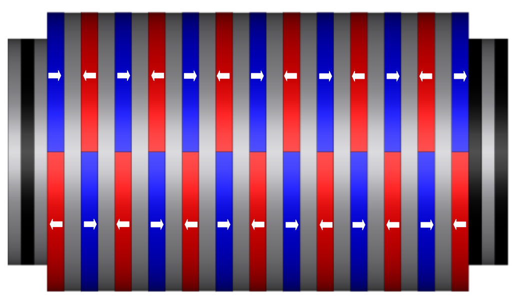

Fig. 2-39. Proposed new MGLS

Therefore, by choosing a half ring shift $L_a = 2w_o$, a particularly simple design is achieved since the outer rotor is made of complete ferromagnetic rings with half-ring magnets. Such a design is illustrated in Fig. 2-39.

### 2.5.2 FEA Analysis

The MGLS demonstrated in the previous section (with $L_a$ = 9.6 mm) was simulated using JMAG FEA software. The radial magnetic flux density due to the inner rotor magnets in the outer airgap with and without translator effect is shown in Fig. 2-40-a. Spatial harmonics created by the translator are depicted in Fig. 2-40-b. The modulation effect of the translator rings results in a large 6$^{th}$ harmonic being created in the outer air-gap. The same plots for the radial magnetic flux density in the inner airgap when magnets are only present on the outer cylinder are shown in Fig. 2-41.

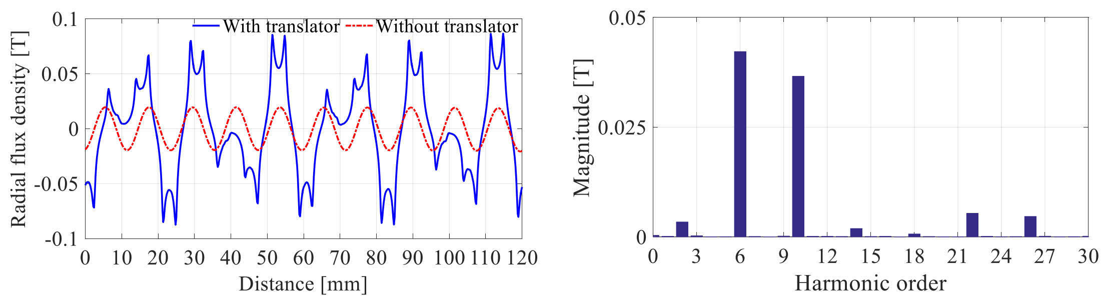


(a) (b)

Fig. 2-40. a) Radial flux density in the outer airgap ($r$=32.75 mm) when only inner rotor magnets present. b) Harmonic content with translator present

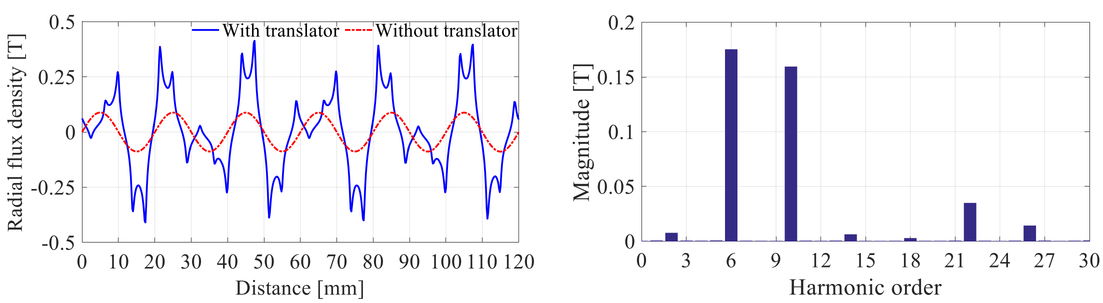


(a) (b)

Fig. 2-41. a) Radial flux density in the inner airgap ($r$=26.25 mm) when only outer cylinder magnets. b) Harmonic content with translator presents

The force and torque on the different parts, when the inner rotor is rotated by 360$^o$ while the other two parts are stationary, is shown in Fig. 2-42. The peak pole slipping force and torque occurs at $F_t$ = 1435 N and $T_i$ = 1.72 Nm, respectively. The values given in Table 2-VIII (with $L_a = 2w_o$) were used in the analysis.

Considering the inner rotor speed to be $\omega_i$ = 80 r/min, and a translator speed of $v_t$ = 10 mm/s, the continuous force and torque were calculated using 3D FEA. Fig. 2-43 shows the calculated force and torque on the different parts. A relatively low force ripple and torque ripple are present at peak conditions. The calculated magnetic shear stress of this design is 130 kN/m$^2$.

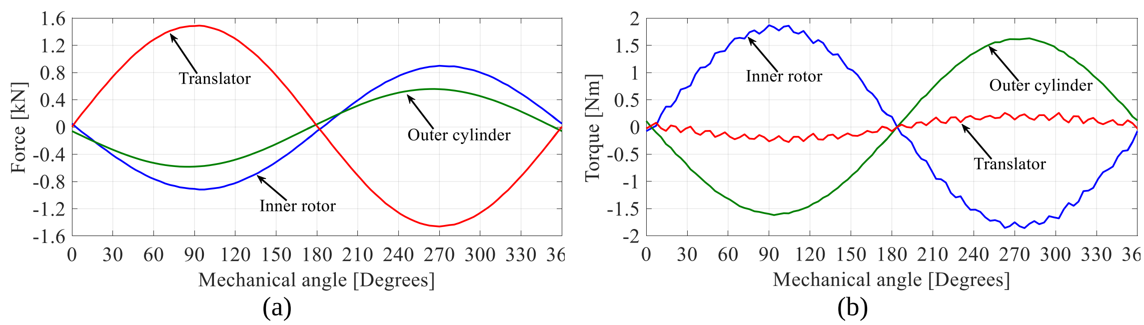


Fig. 2-42. a) Force and b) torque on each MGLS part as a function of inner rotor phase angle.

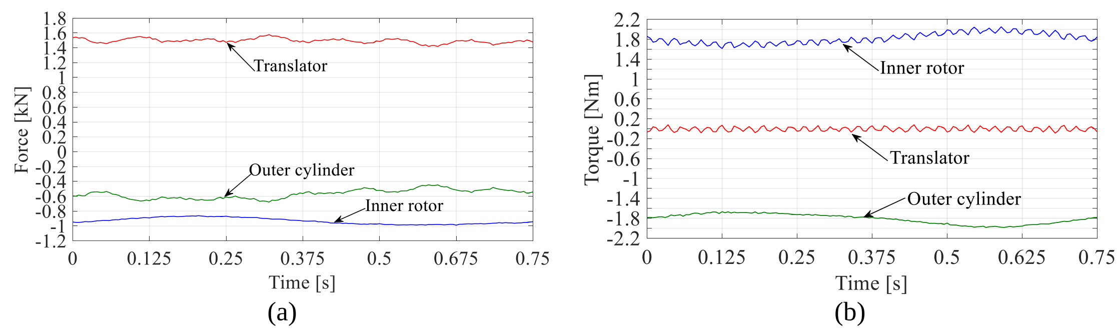


Fig. 2-43. a) Force and b) torque on each MGLS part due to rotation of the inner rotor and translation of the translator at the same time.

### 2.5.3 Experimental Verification

The inner rotor of the new MGLS is the same as the first prototyped MGLS (Section 2.4.3), but the outer cylinder and the translator have been modified. These two parts are shown in Fig. 2-44. The calculated and measured radial flux density for the inner rotor and outer cylinder are depicted in Fig. 2-45-a and Fig. 2-45-b. Their corresponding main harmonic orders are compared in Fig. 2-45-c and Fig. 2-45-d. The 10$^{th}$ harmonic of the inner rotor flux density is just 0.6% lower than the 10$^{th}$ harmonic of the calculated flux density. This discrepancy is 8.2% for the 6$^{th}$ harmonic of the outer cylinder flux density.

(a) (b)

Fig. 2-44. MGLS components; a) outer cylinder, b) translator.

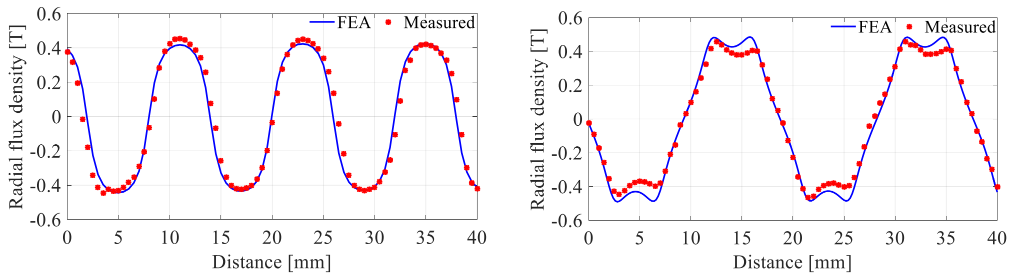


(a) (b)

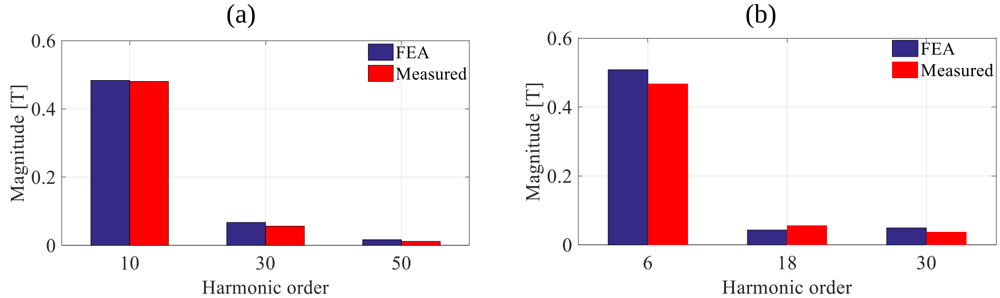


(c) (d)

Fig. 2-45. Calculated and measured flux density and the corresponding main harmonics at 0.85 mm above the surface of (a) inner rotor and (b) outer cylinder when they are surrounded by air. The corresponding harmonics for the inner rotor and (fixed) outer cylinder are compared in (c) and (d) respectively.

The test setup for the force measurement is shown in Fig. 2-46 and Fig. 2-47. In this test the inner rotor was rotated while the translator was pushed against an obstacle.

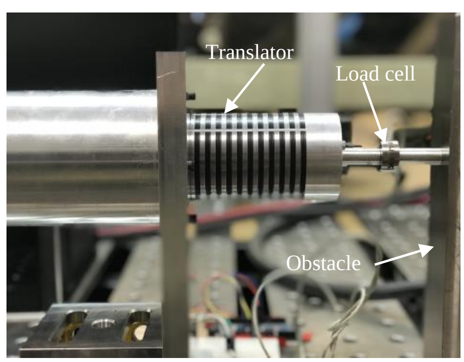


Fig. 2-46. Test setup for force measurement

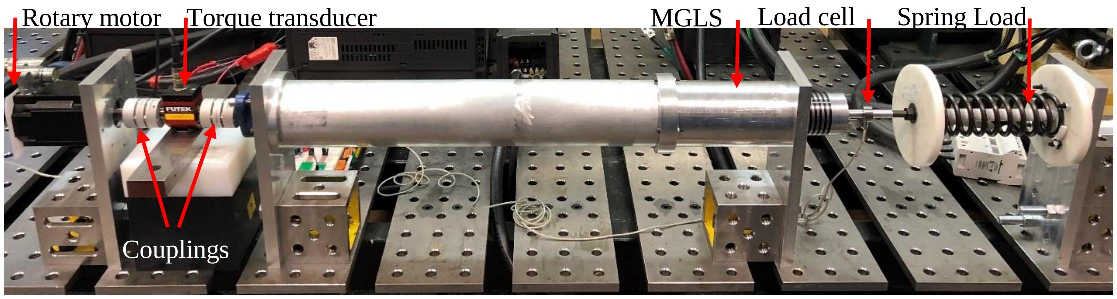


Fig. 2-47. MGLS on the test bed connected to a spring load

Measured force and torque are shown in Fig. 2-48. As can be seen the measured maximum force value is considerably lower than the calculated force while the applied torque is larger than calculated. The possible reason for this discrepancy is the high friction inside the MGLS against both rotation and translation.

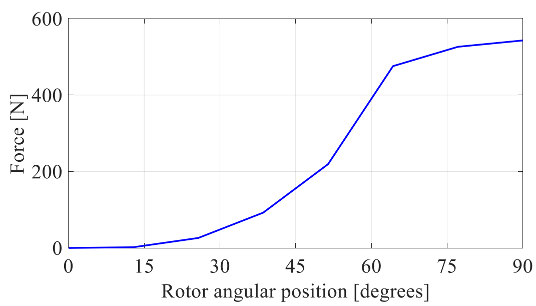


a

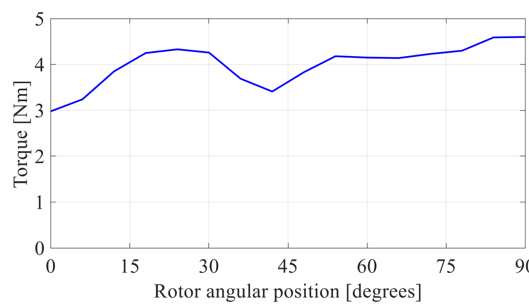


b

Fig. 2-48. a) Measured translator force, b) measured inner rotor torque, when inner rotor was rotated while translator pushed against an obstacle.

Fig. 2-49 shows a cutaway view of the MGLS. As can be seen, the translator slides between two sets of sleeve bearings. Although a set of three plastic rods was considered to reduce the contact point, there is still a considerable amount of friction. The inner rotor, which is connected to two of these sleeve bearings, experiences friction against its motion. In order to further understand these losses, two no-load tests were performed. Fig. 2-50 shows the measured torque, while the inner rotor was rotated and translator was free to move. As there was no load attached to the translator, this torque is only due to friction losses.

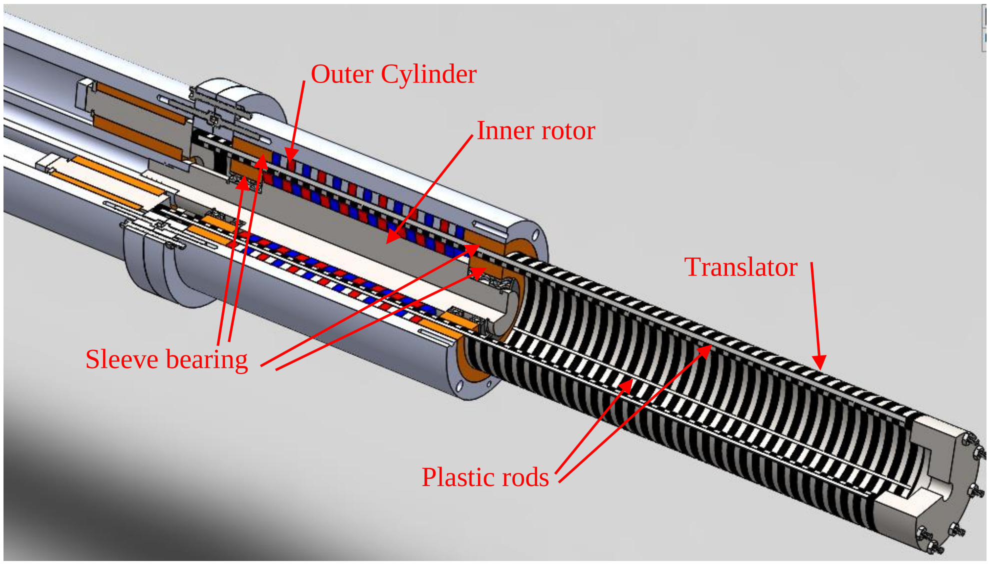


Fig. 2-49. 3D cut view of the MGLS showing the plastic rods and sleeve bearings

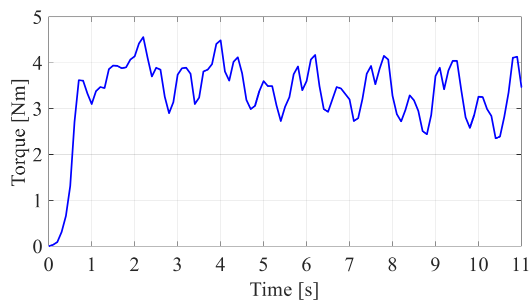


Fig. 2-50. Measured torque while inner rotor was rotated and translator was free to move.

Deduction of the average friction torque from the measured torque in previous test (Fig. 2-48 (b)) results in a value comparable to the calculated torque. In another test, the translator was pushed in using a mechanical actuator (not shown in the picture), while the torque and force values were measured. Fig. 2-51 shows the results of this test. It can be seen that about 1.9 kN, which is considerably larger than the calculated force, is applied while the measured torque of about 1.7 Nm is comparable to the calculated torque. These results shows that a part of the applied force is lost to overcome the friction.

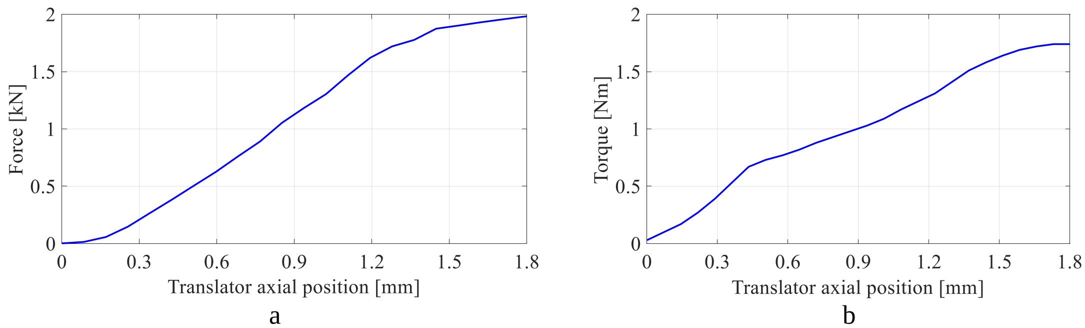


Fig. 2-51. a) Measured translator force, b) measured inner rotor torque, when translator was pushed in using a mechanical actuator.

### 2.5.4 Conclusion

Two different types of MGLS have been proposed for the first time. Manufacturing the skewed translator rings with high tolerance is vital, and a small change in the thickness of the translator rings results in a significant reduction of output force. In order to address this issue, a MGLS without translator skewing was proposed. The PM poles of the outer cylinder in the second version of the MGLS were required to be skewed instead, which was achieved using half-ring magnets. Results show that with a simpler structure the later version of the MGLS achieves the same force performance. The experimental results shows that a considerable friction exist within the structure of the MGLS. This issue could be considered by redesigning the MGLS both magnetically and mechanically. For high torque linear motion applications, the MGLS could be further driven using a magnetically geared motor. In the following chapter a new type of axial MG motor is investigated for low speed applications.

# 3 Chapter 3: Axial Flux-Focusing Magnetically Geared Motor

## 3.1 Introduction

Growing concerns about climate change have motivated researchers to make use of clean and renewable energy. Wind power generation and hybrid electric vehicles (HEV) are two areas that have attracted attention recently. The two characteristics of these applications are their low speed and high torque nature. Electrical machines cannot provide high torque with low speed unless either they use a reduction mechanism or they have a large number of poles. Since a limited number of poles can be fitted within a limited circumference, they need to be made large and bulky.

Mechanical gears are used as the reduction mechanism to meet the electromechanical requirements of the electrical machine [62]. Due to the physical contact between their moving parts, they suffer from low reliability, high noise, and regular maintenance requirements. Moreover, they have a short life time. For example, the life time of a typical wind turbine is 20 years, while the mechanical gearboxes usually fail before this. The cost of replacing the mechanical gearbox is up to 10 percent of the original construction cost [63].

As an alternative, MGs have been investigated. MGs, like their conventional mechanical counterparts, provide torque and speed conversion. The unique characteristic of the MG is its ability to provide contactless speed conversion. MGs offer a number of significant potential advantages compared with their mechanical counterpart, such as quieter operation, improved reliability, higher efficiency, reduced maintenance requirements, and inherent overload protection [37], [64].

An axial flux magnetic gear (AFMG) operates based on the same concept as the coaxial version, as discussed in section 1.2.5. As they take up less axial space, they are suitable for some specialized applications and have been considered for use in hybrid electric vehicles [65], [66].

MGs can be either connected to a regular machine as a separate part, or they can be combined with the electrical machine to construct a magnetically geared machine (MGM), which has a more compact design, and fewer moving part. The focus of this chapter is on investigating a unique AFMG and its integration with electrical machines to construct a compact direct-drive machine. The MGM could then be connected to the MGLS further increasing the torque to force ratio.

### 3.2 Brief Review of Axial Flux Magnetically Geared Motors

Mezani *et al.* [38] proposed an AFMG, shown in Fig. 3-1. It works based on the same concept as the coaxial MG concept (section 1.2.5), but three parts of the AFMG are placed along the axial direction instead of radially. A calculated torque density of 70 Nm/L was reported for this design.

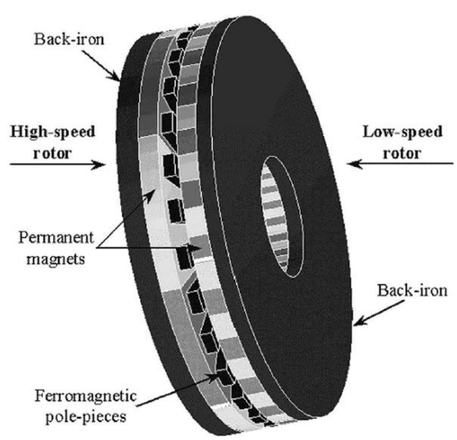


Fig. 3-1. Schematic of an AFMG [38].

Wang *et al.* [67] combined an AFMG with a PM generator to construct an AFMGM for a wind power application, as shown in Fig. 3-2. It consists of an axial machine connected to the high speed rotor of an AFMG with a gear ratio of $G_r \approx 6.67$. Although the high speed rotor of the AFMG is directly connected to the PM rotor of the generator, they have two separate sets of PM poles. A solid iron disc was used as the back iron for both the high speed rotor of the MG and the stator PM rotor. The PMs on either side of the stator PM rotor and high speed rotor can be arranged in either the same coupled polarity or the opposite decoupled polarity shown in Fig. 3-3. The magnetic field of the low speed rotor in the coupled design contributes to the total flux linkage in the stator. Therefore, the coupled structure results in a slightly higher back-EMF in the stator winding.

Wang *et al.* calculated an active region torque density of 105 kNm/m$^3$ for just the MG part when the outer diameter is 320 mm. If the volume of the generator, which was almost the same as the MG, is also considered, the torque density significantly decreases.

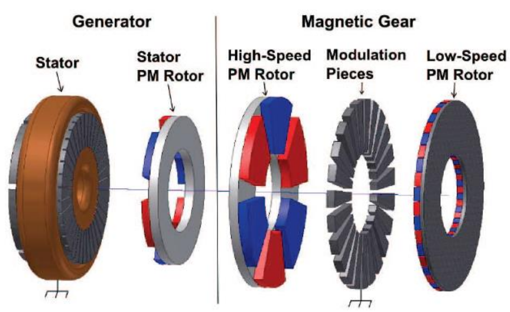


Fig. 3-2. An axial flux magnetically geared machine proposed by Wang *et al* [67]

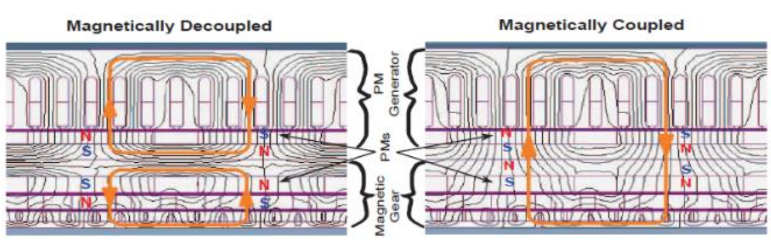


Fig. 3-3. Magnetic field distribution in coupled and decoupled designs [67]

The advantage of this design is that both the MG and the generator can be optimized individually to achieve good performance. For example, machines with a larger least common multiple (LCM) between the number of poles and slots have a lower cogging torque [68]. This can also be considered by checking the “goodness” of the pole-pair combination of the MG. Zhu *et al.* [68] define an index named the cogging factor to check the “goodness” of the design as follow:

$$C_T = \frac{2p \times Q}{LCM(2p, Q)} \tag{3.1}$$

where $p$ is the number of pole-pairs, and $Q$ is number of stator slots or modulator pole-pieces. A unity cogging factor is preferred. Wang’s design has a unity cogging factor for the MG side, but $C_T = 6$ for the generator side. This is due to a relatively small LCM of 36 between the number of slots and poles.

This design is simply stacking an AFMG with an axial generator. In comparison when using a radial version of these machines, this AFMGM considerably reduces the axial length of the overall design.  However, as the MG and the generator are physically independent and do not share any part, this cannot be considered as a compact axial machine design.

Johnson *et al.* [69] proposed a compact AFMGM in which the electrical machine is placed in the bore of the AFMG, as shown in Fig. 3-4. As the addition of the electrical machine does not add to the overall size of the AFMGM, a relatively compact design results. A volumetric torque density of 62.6 kNm/m$^3$ was reported for the MG when the outer diameter is 239 mm. The torque density of AFMGM was 60.6 kNm/m$^3$, which shows a negligible reduction in comparison with just the MG. The rotor has 10 poles, and the stator has 24 slots with a concentrated winding, which results in a cogging factor of $C_T$ = 4. The MG has a gear ratio of $G_r \approx 9.33$, with 3 and 28 pole-pairs on the high speed and low speed rotors respectively, which results in a unity cogging factor. As the generator and high speed rotor of the MG have different numbers of pole-pairs, this design results in a sinusoidal back-EMF (i.e. no contribution from the MG side). One disadvantage of this design is that in order to magnetically isolate the AFMG and PM machine, a large radial airgap was considered, which in turn limited the space for integrating the PM machine. Heat transfer in this design may also be challenging, and could limit the rating of the PM machine. Diagnosis and maintenance of the generator could be another issue for this design.

Fig. 3-5 shows the structure of an AFMGM proposed by Niguchi *et al.* [70]. In this design, one of the AFMG's PM rotors is replaced by a stator. Both the stator teeth and steel pole-segments of the low speed rotor modulate the magnetic field and create additional harmonics, which interact and generate torque in both airgaps. The gear ratio is given by:

$$G_r = \frac{n_l}{2 \times p_h} \tag{3.2}$$

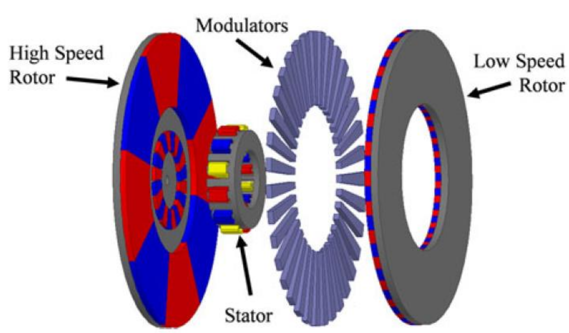


Fig. 3-4. AFMG proposed by Johnson *et al.* [69]

where $n_l$ = 20 and $p_h$ = 4 are the number of steel pole-segments of the low speed rotor and the number of pole-pairs of the high speed rotor, respectively. The calculated gear ratio is 2.5. This design suffers from very low torque density (15 kNm/m$^3$) and high torque ripple (62.5 percent). The former is due to using only one PM rotor. The high cogging toque could be due to the high cogging factor ($C_T$ = 4). Tong *et al.* [65] proposed an AFMGM, which is shown in Fig. 3-6, for a HEV application. This design also has poor torque density performance because only one rotor contains PMs. It was determined by Fu [71] that using only one PM rotor results in the torque density being no better than a direct-drive motor.

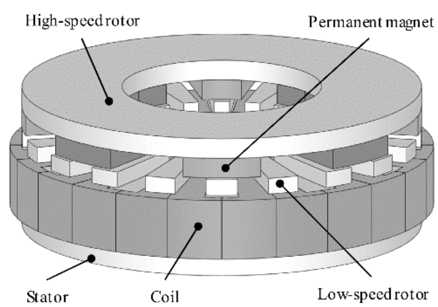

Fig. 3-5. AFMGM proposed by Niguchi *et al.* [70]

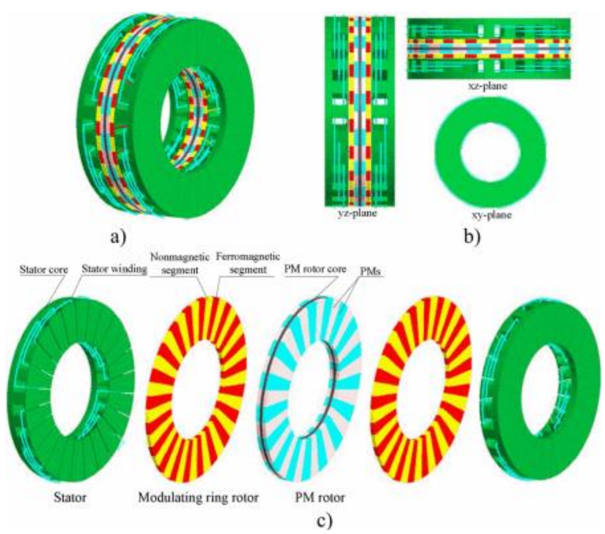

Fig. 3-6. Structure of the proposed AFMGM by Tong *et al.* [65]

Using the modulating steel pieces of the AFMG as the stator teeth is another approach to construct an AFMGM. Fig. 3-7 shows a design of this type, proposed by Zaytoon *et al.* [72]. This design is an AFMG with a winding around the steel pole-pieces of the modulator. This design consist of a high speed rotor with two PM pole-pairs, a low speed rotor with seven pole-pairs, and a modulation section with nine ferromagnetic segments. Nine individual windings are placed around the ferromagnetic pole-pieces, which construct a nine-phase electrical machine. This combination results in a gear ratio of 3.5. As this design takes advantage of two PM source of magnetic field, a higher flux density exist within the airgap, which results in higher torque density. A very low torque density of about 46 $kNm/m^3$ was achieved using an outer diameter of 140 mm.

The stator of this AFMGM is sandwiched between the two rotors, which makes heat dissipation difficult. This limits the current density of the winding. In order to fit the required winding turns around the pole-pieces, the pole-pieces need to be made thicker, which decreases the torque density because it increases the volume of the machine by increasing the axial length.

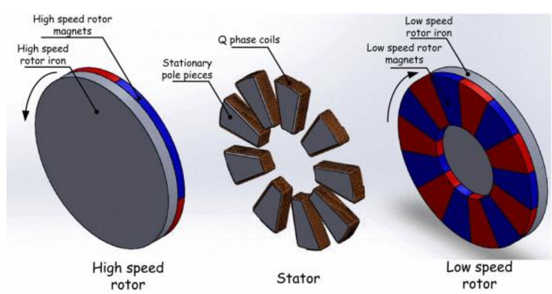


Fig. 3-7. Exploded view of the axial flux magnetically geared machine proposed by Zaytoon *et al.* [72]

Khatab *et al.* [73] presented an AFMGM similar to Zytoon's design [72]. This design was inspired by the yokeless and segmented armature (YASA) axial flux PM machine (AFPM), proposed by Woolmer *et al.* [74]. YASA is a double-sided AFPM, which contains a stator with magnetically separated segments between two PM rotors with the same number of poles. The only difference between the YASA motor and the proposed AFMGM is that the number of pole-pairs on the three parts is different and satisfies (1.6)

$$n_t = p_i + p_o \tag{1.6}$$

Therefore, this design works based on the MG concept. Fig. 3-8 shows the structure of the Khatab's design, which includes a high speed rotor with 5 PM pole-pairs, a low speed rotor with 7 pole-pairs and a stator with 12 ferromagnetic segments.

The combination of the pole-pairs and steel pole-pieces in a regular MG must satisfy (1.6). In order to reduce the torque ripple, combinations with unity cogging factor are preferred. But for Khatab's design, other considerations also must be taken into account. For example, the number of steel-pieces must be a multiple of the number of phases. In addition, the relationship between the stator slot number and rotor pole number should satisfy [73]:

$$n_s = p + 2 \tag{3.3}$$

where $n_s$ and $p$ are the number of stator slots and rotor poles, respectively.

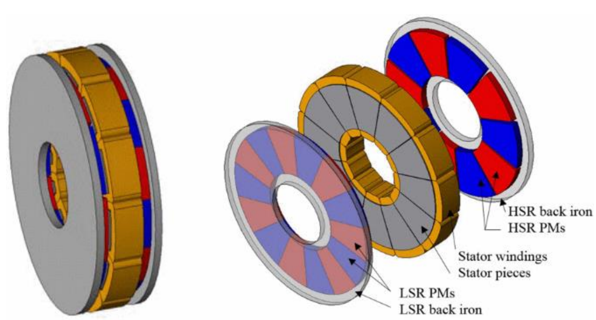

Fig. 3-8. Axial flux magnetically geared machine proposed by Khatab *et al.* [73]

This limitation constrains the number of feasible pole-pair combinations and the gear ratio. For example, Khatab's design uses a small gear ratio of 1.4. In comparison, HEVs use planetary gears with gear ratios between 1.5 to 3 [75]. A torque density of 44 kNm/m$^3$ with outer diameter of 90 mm is reported.

### 3.3 Axial Flux-Focusing Magnetic Gear

Fig. 3-9 shows the structure of a AFMG proposed by Acharya *et al.* [76], [77]. It consists of three parts; two rotors with PM poles, which have been arranged in a flux-focusing structure, and a rotor with ferromagnetic pole pieces in between them, which modulates the magnetic field of the other parts. Rotor 1 consists of $p_1 = 6$ pole-pairs and rotates at $\omega_1$, rotor 2 consists of $n_2 = 25$ ferromagnetic steel poles and rotates at $\omega_2$, and rotor 3 consists of $p_3 = 19$ pole-pairs and rotates $\omega_3$. The number of pole-pairs must satisfy (1.6). If rotor 3 is fixed, the speed relationship will be as (1.8). The gear ratio is $G_r = n_2/p_1 \approx 4.16$.

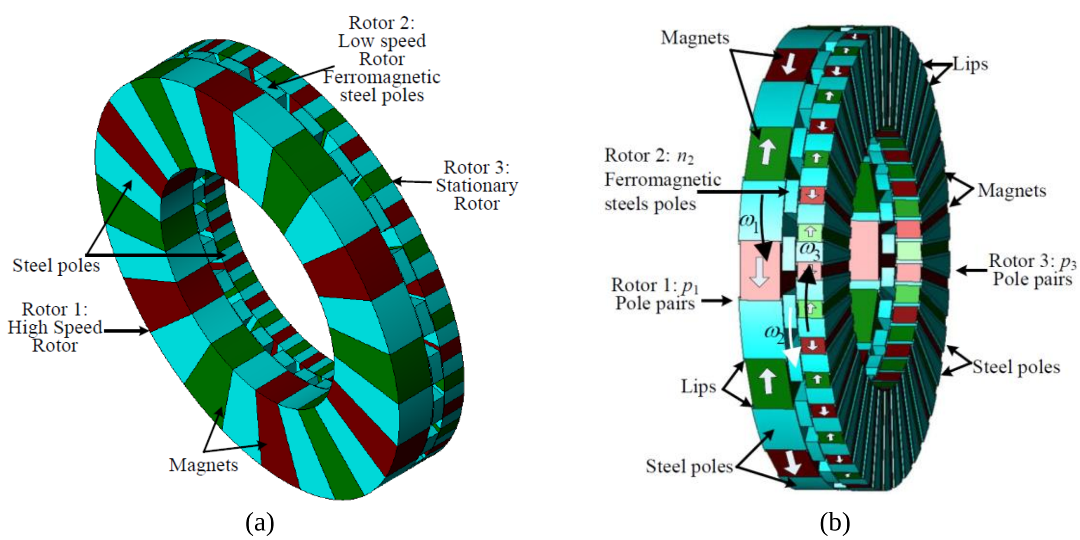


Fig. 3-9. An axial flux magnetic gear with a flux-focusing typology proposed by Acharya *et al.* [76], [77]. a) Optimized design, b) assembly design with rectangular magnets and steel poles' lips. $p_1 = 6$ $n_2 = 25$ and $p_3 = 19$.

Fig. 3-10 shows the design parameters and the initial design used by Acharya *et al*. A summary of these parameters is given in Table 3-I. A torque density of 289.8 Nm/L was reported for the design shown in shown in Fig. 3-9-a. Practical considerations including rectangular shaped magnets and steel pole lips in addition to increasing the axial length of the rotor three led to the design shown in Fig. 3-9-b. Acharya showed that these considerations result in lower, but still high torque density of 257.6 Nm/L. The later design was re-simulated in JMAG to verify Acharya's results.

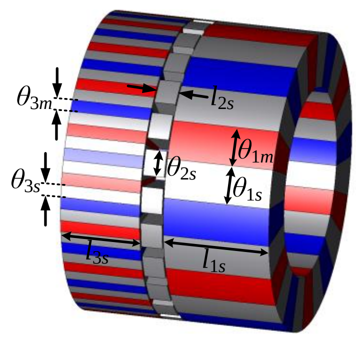


Fig. 3-10. Geometric parameters used for the axial flux magnetic gear with a flux-focusing typology [76], [77]. .

Table 3-I. Summary of the Design Parameters

| Parameter | | Value | | | Unit |
|---|---|---|---|---|---|
| | | Design by Acharya [76], [77] | | Current design | |
| | | Optimized | Assembly | | |
| High speed rotor | Pole-pairs, $p_1$ | 6 | 6 | 6 | - |
| | Steel pole span, $\theta_{1s}$ | 15 | 15 | 15 | degrees |
| | Magnet dimentions | $\pi\times(140^2\text{-}80^2)\times25/24$ | 36×60×25 | 36×60×25 | $mm^3$ |
| | Axial length, $l_{1s}$ | 25 | 27 | 27 | mm |
| | Airgap length, $g$ | 0.5 | 0.5 | 1 | mm |
| Low speed rotor | Pole pieces, $n_2$ | 25 | 25 | 25 | - |
| | Steel pole span, $\theta_{2s}$ | 8.5 | 8.5 | 9.5 | degrees |
| | Axial length, $l_{2s}$ | 8 | 8 | 8 | mm |
| Fixed rotor | Pole pairs, $p_3$ | 19 | 19 | 19 | - |
| | Steel pole span, $\theta_{3s}$ | 4.74 | 4.74 | 4.74 | degrees |
| | Magnet dimentions | $\pi\times(140^2\text{-}80^2)\times15/76$ | 11×60×20 | 11×60×20 | $mm^3$ |
| | Axial length, $l_{3s}$ | 15 | 22 | 22 | mm |
| MG Radial | Outer radius, $r_o$ | 140 | 140 | 140 | mm |
| | Inner radius, $r_i$ | 80 | 80 | 80 | mm |
| Material | NdFeB magnet, $B_r$, NMX-40CH | 1.25 | 1.25 | 1.25 | T |
| | Resistivity | 1080 steel, 18 | | 1018 steel, 15.9 | μΩ-cm |
| | Resistivity | 430FR steel, 76.4 | | 416 steel, 57.0 | μΩ-cm |

Fig. 3-11 shows the geometry of the AFMG used in this dissertation. The airgap was increased to 1 mm and the steel pole lips were place on only one side (facing the airgap). A torque density of 173.2 Nm/L was calculated for this design. Geometric and performance comparison of these three designs are given in Table 3-I and Table 3-II respectively.

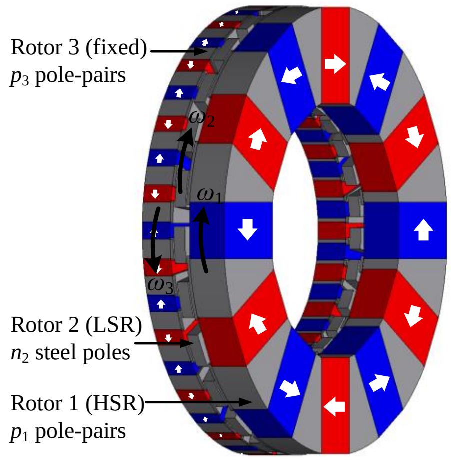


Fig. 3-11. An axial flux magnetic gear with a flux-focusing typology based on [76], [77]. $p_1 = 6$, $n_2 = 25$, and $p_3 = 19$.

### 3.3.1 Field Analysis

A 3D FEA model of the AFMG was simulated in order to verify its published performance. Fig. 3-12 shows the generated mesh using JMAG FEA software. Total number of about 16.5 million elements created a design with relatively fine mesh. Fig. 3-13-a shows the axial flux density near the fixed rotor due to the magnets only on the high-speed rotor (rotor 1), with and without the modulation effect of the low-speed rotor. Fig. 3-13-b shows the corresponding harmonic content of the modulated axial flux density. The same plots for the axial flux density near the high-speed rotor due to magnets only on the fixed rotor is shown in Fig. 3-14. The modulation effect of the low-speed rotor is clearly evident.

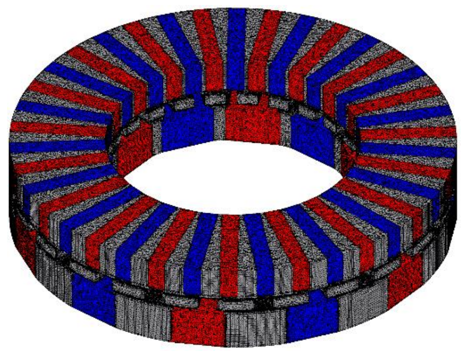

Fig. 3-12. Generated mesh using JMAG FEA software

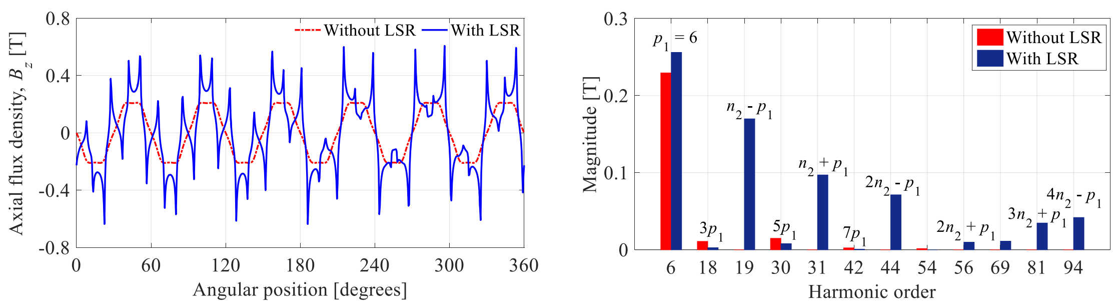


(a) (b)

Fig. 3-13. a) Axial flux density near fixed rotor 3 due to magnets only on the high-speed rotor (rotor 1) at a radius of $r$=137 mm and an axial distance of 0.5 mm. b) Corresponding harmonic contents.

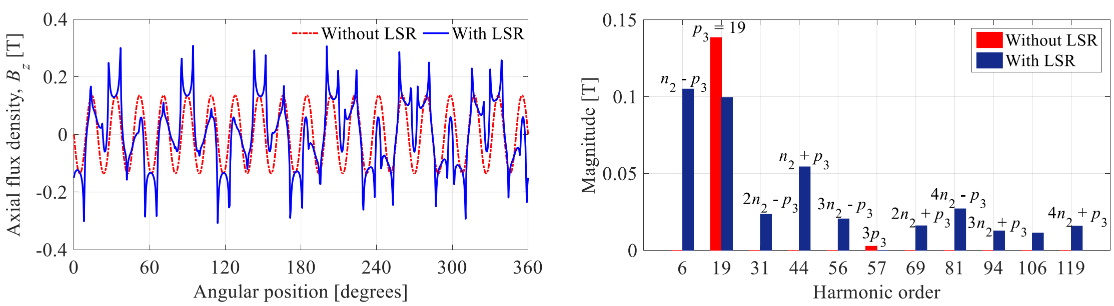


(a) (b)

Fig. 3-14. a) Magnetic flux density near the high-speed rotor due to magnets only on the fixed rotor 3 at a radius of $r$=137 mm and an axial distance of 0.5 mm. b) Corresponding harmonic contents.

### 3.3.2 Performance Analysis

Torque on the different parts of this AFMG, when only the low-speed rotor is rotated, is shown in Fig. 3-15. An active region torque density of 173.2 Nm/L was calculated to be achievable. Torque and force on different parts of the AFMG when both rotors were rotated are shown in Fig. 3-16 and Fig. 3-17, respectively. A large axial force characteristic is present within the AFMG. This makes assembly challenging.

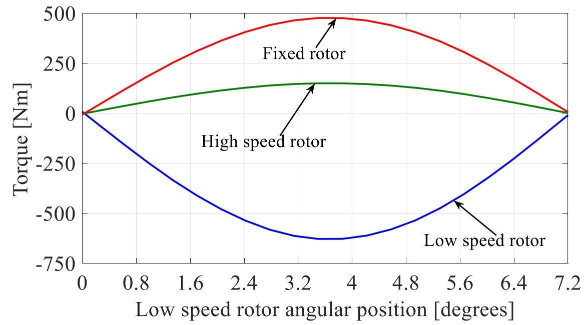


Fig. 3-15. Torque on the low speed rotor (LSR), high speed rotor (HSR) and fixed rotor for the case when only the low speed rotor is rotating with practical design considerations.

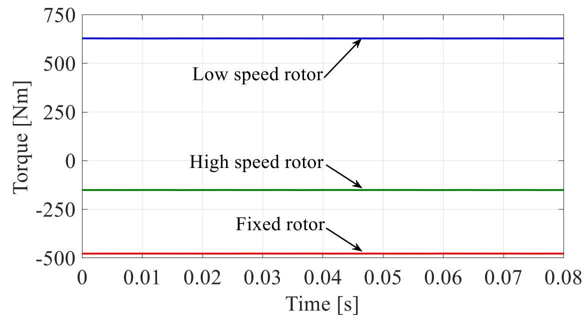


Fig. 3-16. Torque on the low speed rotor (LSR), high speed rotor (HSR) and fixed rotor for the case when both rotors were rotated with practical design considerations.

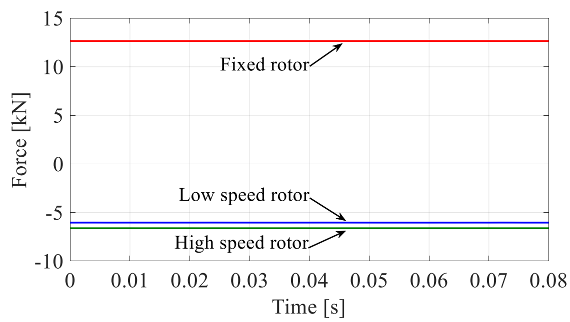


Fig. 3-17. Axial force characteristics of the AFMG for the case when both rotors were rotated with practical design considerations.

Table 3-II. Performance comparison between the initial design and current design

| Parameter | Acharya et al. [76] | | Current design | Unit |
|---|---|---|---|---|
| | Optimized | Assembly | | |
| Torque | 872.3 | 919.9 | 628.6 | Nm |
| Volume | 3.01 | 3.57 | 3.63 | L |
| Magnet mass | 6.3 | 8.74 | 8.74 | kg |
| Torque density | 289.8 | 257.6 | 173.2 | Nm/L |
| Torque per kg of magnet material | 138.4 | 105.26 | 72 | Nm/kg |

### 3.3.3 Experimental Results

The experimentally constructed high-speed rotor, low-speed rotor and fixed rotor are shown in Fig. 3-18. The measured axial magnetic flux density, $B_z$, when the rotors are surrounded by air for the high-speed rotor is compared in Fig. 3-19. Fig. 3-20 shows the field comparison next to the fixed rotor. The measured 6$^{th}$ harmonic of the high-speed rotor and the measured 19$^{th}$ harmonic of the fixed rotor are respectively 1.7% and 5.2% lower than calculated. Note, these values are different from the reported values in [78] because incorrect dimensions for the Gauss meter probe were considered. This resulted in larger difference between FEA and measured values. As the fixed rotor contains a higher number of poles the measurement accuracy is less than that for the high-speed rotor so a larger discrepancy in this case could be partly related to measurement error.

(a) (b) (c)

Fig. 3-18. The experimentally assembled axial flux focusing magnetic gear with a) high-speed rotor, b) low-speed rotor, and c) fixed rotor.

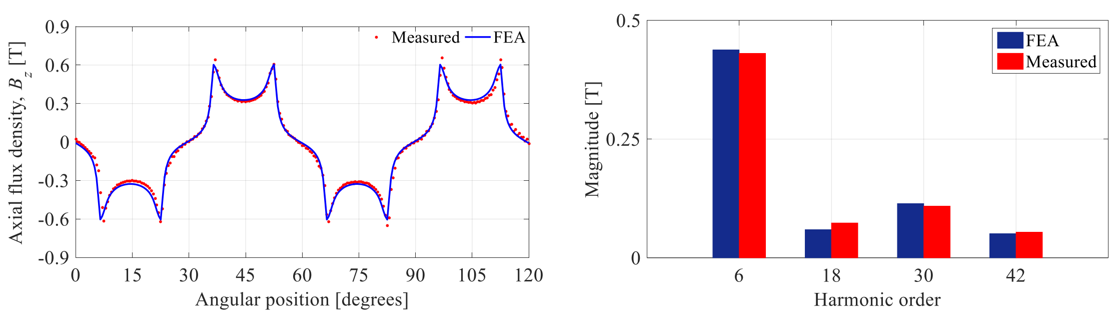


(a) (b)

Fig. 3-19. a) High speed rotor axial magnetic flux density at r = 135mm and 1.04mm above the axial rotor and b) corresponding spatial harmonic comparison showing the 6th, 18th, 30th, and 42nd harmonic for the measured and FEA calculated axial flux density (when surrounded by air).

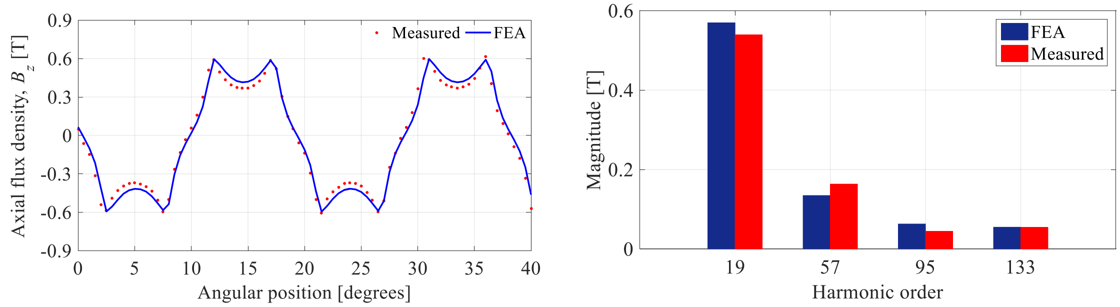


(a) (b)

Fig. 3-20. a) Fixed rotor axial magnetic flux density field when the rotor surrounded by air at r = 135mm and z = 1.04mm above the rotor b) Corresponding harmonic analysis showing the 19th, 57th, 95th, and 133rd harmonic for measured and FEA calculated axial flux density for the fixed rotor (when surrounded by air).

The axial MG assembly on the test bed is shown in Fig. 3-21. The low-speed rotor was driven by an induction motor, while the high-speed rotor was connected to a PM generator. The high-speed rotor was rotated at $\omega_1$ = 50 r/min. Using the torque control method, a stepped load torque was applied to the MG until it reached the pole-slip torque point. The resultant torque plot is shown in Fig. 3-22.

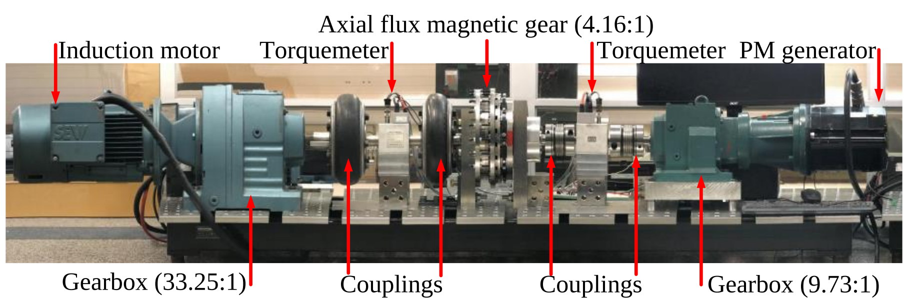


Fig. 3-21. Axial magnetic gear on the test bed

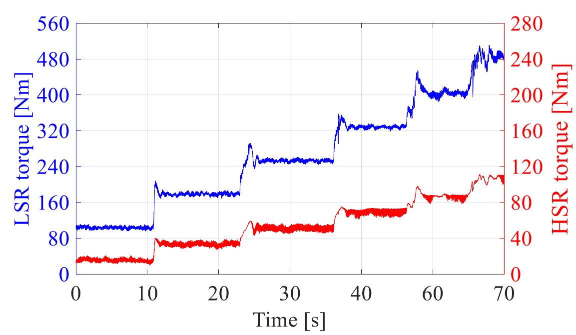


Fig. 3-22. Measured torque on high speed and low speed rotors.

The peak measured torque was 553.2 N m, which resulted in the measured active region volumetric and mass torque density being 152.3 N·m/L and 42.3 N·m/kg respectively. This is 12 % lower than calculated. The reason for this discrepancy is believed to be primarily due to the mechanical frictional losses within the axial bearings as well as for the unaccounted-for eddy current losses within the solid steel poles and support mechanical structure. The large axial forces present within the MG create significant challenges with respect to mechanical construction and cause mechanical losses within the bearings.

The measured no-load torque on the high speed and low speed rotor is shown in Fig. 3-23. Fig. 3-24 shows the power loss as a function of load. The power loss does not change with increasing load when the MG input speed is held fixed at $\omega_1$ = 50 r/min. This therefore results in the efficiency increasing significantly with increased applied load.

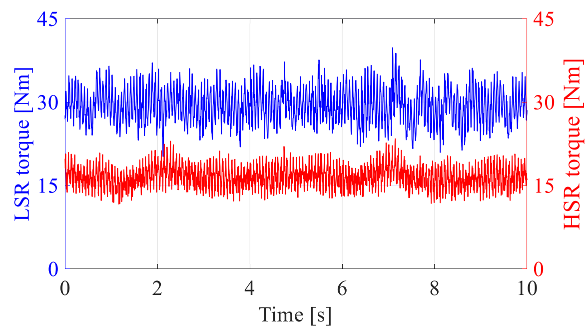


Fig. 3-23. Measured no load torque on low speed and high-speed rotors

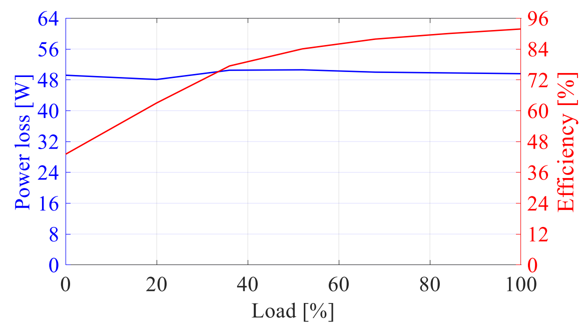


Fig. 3-24. Power loss and efficiency as a function of the load torque at 50 r/min high speed rotor speed.

The measured torque ripple as a function of the load for the low speed and high speed rotors is shown in Fig. 3-25 and Fig. 3-26, respectively. The torque ripple for different loads is relatively unchanged. This results in a very high percentage torque ripple at light loads. A summary of the above experimental analysis results is given in Table 3-III.

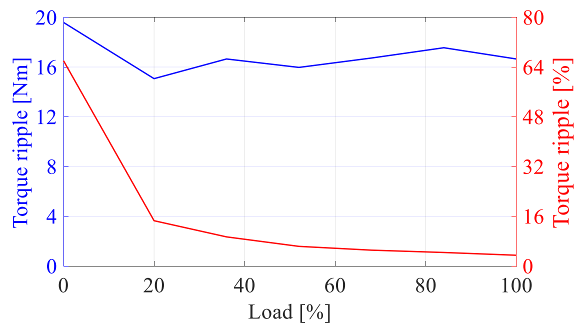


Fig. 3-25. Torque ripple as a function of load for low speed rotor.

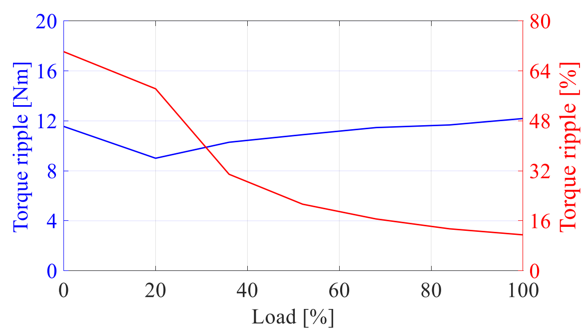


Fig. 3-26. Torque ripple as a function of load for high-speed rotor.

Table 3-III. Measured average torque and calculated power, loss and efficiency at each load step.

| Load % | Power loss [W] | Efficiency | Torque ripple [N·m] | |
|---|---|---|---|---|
| | | | HSR | LSR |
| 0 | 49.2 | 43.07 | 11.55 | 19.58 |
| 20 | 48.1 | 63.02 | 9.01 | 15.06 |
| 36 | 50.5 | 77.41 | 10.28 | 16.64 |
| 52 | 50.6 | 84.06 | 10.89 | 15.96 |
| 68 | 50.0 | 87.86 | 11.46 | 16.72 |
| 84 | 49.8 | 90.01 | 11.67 | 17.55 |
| 100 | 49.6 | 91.79 | 12.18 | 16.64 |

### 3.4 Axial Flux-Focusing Magnetically Geared Motor

In this section a new type of AFMGM, as shown in Fig. 3-27, is proposed. Unlike in [69], the stator is placed on the outer radius of the high-speed rotor. Also due to the use of a flux-focusing rotor structure, the stator takes advantage of the high-speed rotor flux in the radial direction. As a result, there is no need for a separate set of magnet poles for the rotor of the PM motor. Using an externally-mounted stator also enables cooling to be more easily applied. In this section, a fractional slot winding design is discussed and the performance of the proposed AFMGM is investigated.

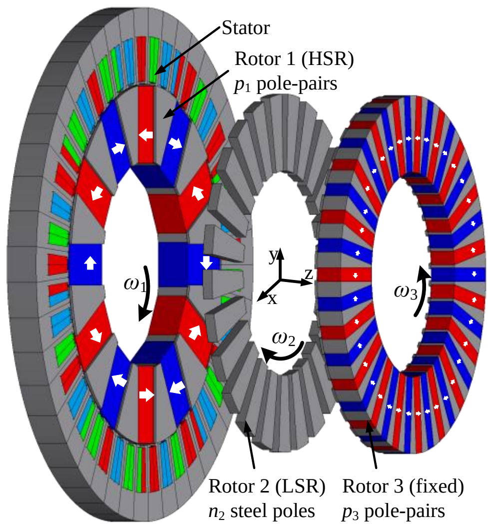


Fig. 3-27. Exploded view of the proposed AFMGM with 45 slot stator around the 6 pole-pair high speed rotor where $p_1$= 6, $n_2$ = 25, and $p_3$ = 19.

### 3.4.1 Stator Slot Design

The stator specifications are given in Table 3-IV. In order to reduce the torque ripple, the selected number of stator slots listed in Table 3-V were evaluated. The least common multiple (LCM) between the number of slots and poles, defined as

$$LCM(Q, 2p_1) \tag{3.4}$$

and slot per pole per phase (SPP), defined as

$$q = Q/(2p_1 \times m) \tag{3.5}$$

and number of slot per pole (SP)

$$q \times m = Q/2p_1 \tag{3.6}$$

are shown in Table 3-V. Where $Q$ is the number of stator slots, $p_1$ is the high speed rotor pole-pairs, and $m$ = 3 is the number of phases.

The combination of 18-slots/12-pole results in a SPP of 0.5. This combination, which uses a non-overlapping winding, generates a high cogging torque due to its small LCM between the number of slots and poles [68]. The 36-slot/12-pole combination results in a unity SPP winding with a simple layout, but it also has a small LCM, which was predicted to produce a high cogging torque. Fractional slot winding designs should reduce the torque ripple [79]. Two feasible combinations of 45-slots/12-poles and 54-slots/12-poles were investigated. As shown in Table 3-V, the combination of 45-slots/12-poles results in the largest LCM in the listed combinations. The winding is feasible when

$$n = Q / (m \times t) \text{ is an integer} \tag{3.7}$$

is satisfied [79]. Where and $t$ is the machine periodicity which is defined as

$$t = GCD(Q, p_1) \tag{3.8}$$

where GCD is the greatest common devisor.

Table 3-IV. Stator Specifications

| Parameter | Value | | Unit |
|---|---|---|---|
| | Initial | Final | |
| Outer radius, $r_{so}$ | 200 | 215 | mm |
| Inner radius, $r_{si}$ | 140.5 | 155.5 | mm |
| Airgap length | 0.5 | 1.5 | mm |
| Stack length | 25 | 16.5 | mm |
| Maximum current density | 6.4 | | A/mm$^2$ |
| Winding fill factor | 0.6 | 0.3 | - |
| Lamination material | M19 Steel | | |

Table 3-V. LCM, GCD, SPP, and SP for Different Combinations of Stator Slots and $p_1$ = 6 Pole-pair Rotor.

| Stator slots, $Q$ | LCM[Q, 2$p_1$] | GCD[Q, $p_1$] | SPP | SP | n |
|---|---|---|---|---|---|
| 18 | 36 | 6 | 0.5 | 1.5 | 1 |
| 36 | 36 | 6 | 1 | 3 | 2 |
| 45 | 180 | 3 | 1.25 | 3.75 | 5 |
| 54 | 108 | 6 | 1.5 | 4.5 | 3 |

In order to observe the effect of the selected number of slots for the stator on the torque ripple, the AFMGM with the selected combination of slots/poles was simulated using JMAG 3D FEA software, when there was no current excitation. These four models are shown in Fig. 3-28. Table 3-VI shows the average torque on the different parts of the AFMGM, and Table 3-VII shows the corresponding torque ripple. The fractional slot design significantly reduces the torque ripple. As predicted, the 45 slot stator results in the lowest torque ripple on the high-speed rotor and the stator. The 54 slot stator design has the lowest torque ripple on the low-speed rotor and the fixed rotor. However, the purpose of using fractional slot winding is to reduce the torque ripple on the combination of the stator and high-speed rotor. Therefore, 45 slot stator was selected.

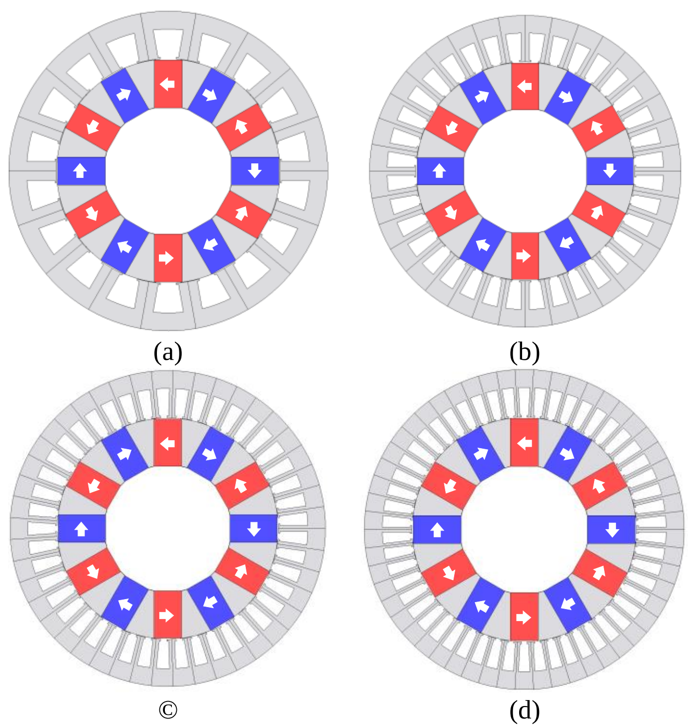


Fig. 3-28. Stator and the high speed rotor of the proposed axial flux magnetically geared motor with a) 18, b) 36, c) 45, and d) 54 stator slots.

Table 3-VI. Average Torque for Each Part of Different Designs

| Design | Average torque [Nm] | | |
|---|---|---|---|
| | Low speed rotor | High speed rotor | Fixed rotor |
| 18 slots | -600 | 145 | 455 |
| 36 slots | -613 | 143 | 466 |
| 45 slots | -626 | 151 | 475 |
| 54 slots | -640 | 154 | 486 |

Table 3-VII. Torque Ripple Comparison for Different Slot Combinations at Peak Torque Condition

| Design | Torque ripple [Nm/%] | | |
|---|---|---|---|
| | Low speed rotor | High speed rotor | Fixed rotor |
| 18 slots | 5.41/0.9% | 15.22/15.3% | 4.38/0.96% |
| 36 slots | 7.48/1.2% | 71.83/120.2% | 6.53/1.4% |
| 45 slots | 2.23/0.4% | 7.3/4.8% | 1.6/0.34% |
| 54 slots | 1.73/0.3% | 14.7/9.5% | 1.83/0.4% |

### 3.4.2 Fractional Slot Winding Design for 45 Slot Stator

In order to design the phase windings for the 45 slot stator, the star-of-slots approach was used [79]. The star-of-slots is the phasor representation of the main EMF harmonic induced in the coil side of each slot, which has *Q/t* spokes, with each spoke containing *t* phasors. The star-of-slots is formed by *Q* phasors. Phasors are numbered based on the designated slot number [79]. For the selected number of slots from (3.5) and (3.6), one can calculate 5/4 slot-per-pole-per-phase and 15/4 slot-per-pole respectively. This indicates that four poles must be distributed over 15 slots and the pattern will be repeated after four poles. The phase shift in electrical degrees between slots, which is the angle between two adjacent phasors, is calculated by

$$\alpha_s^e = p_1 \times (360 / Q) = 6 \times (360 / 45) = 48^\circ \tag{3.9}$$

Considering that the phase shift for the 45 slot design is 48$^o$, the star-of-slots design shown in Fig. 3-29 can be created. An equal number of slots are assigned to all three phases. The winding layouts of the three phases over the first four poles are shown in Fig. 3-30. A slot span of 4 is selected, as it is the closest to 180 electrical degrees (4×48 = 192). Considering $N_t$ turns in each coil, the corresponding turns function $n(\theta)$, and winding function $N(\theta)$, are calculated and shown in Fig. 3-31 and Fig. 3-32 respectively. The turns function and winding function are related by [80]

$$N(\theta) = n(\theta) - < n(\theta) > \tag{3.10}$$

where $<n(\theta)>$ is the average of the turns function, $n(\theta)$, and equal to $(26/15)N_t$, $(11/15)N_t$, and $(-19/15)N_t$ for the phases $A$, $B$, and $C$ windings respectively.

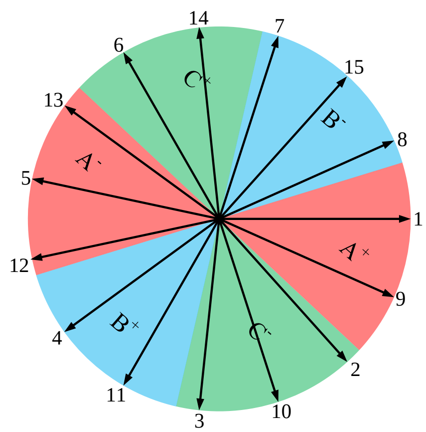


Fig. 3-29. Star of slots phasor diagram of a 45slots/12poles motor.

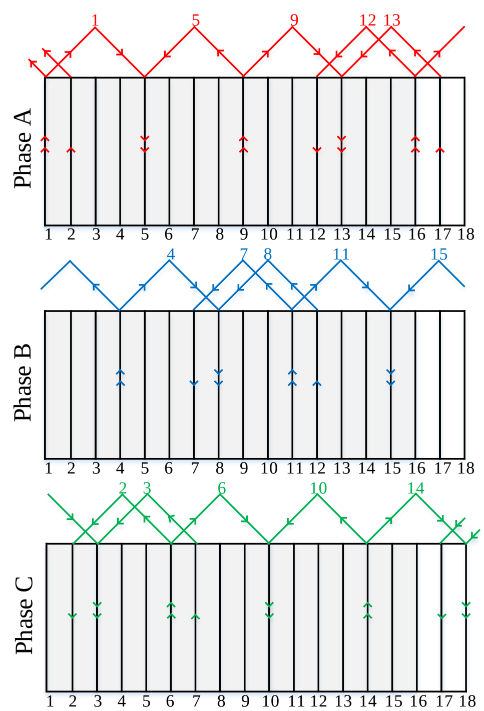


Fig. 3-30. Winding layout of the three phases over the first four poles.

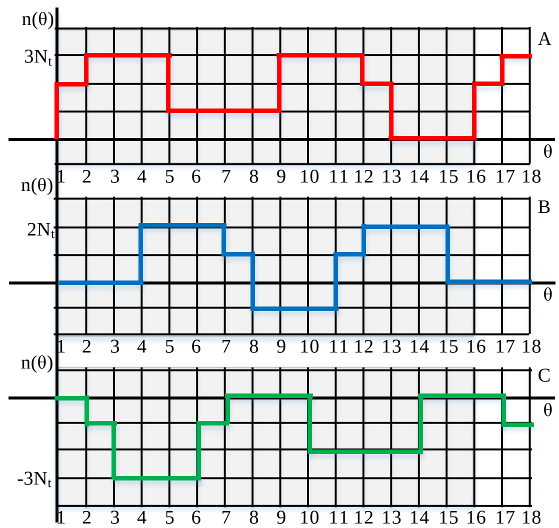


Fig. 3-31. Turns function of the three phases over the first four poles.

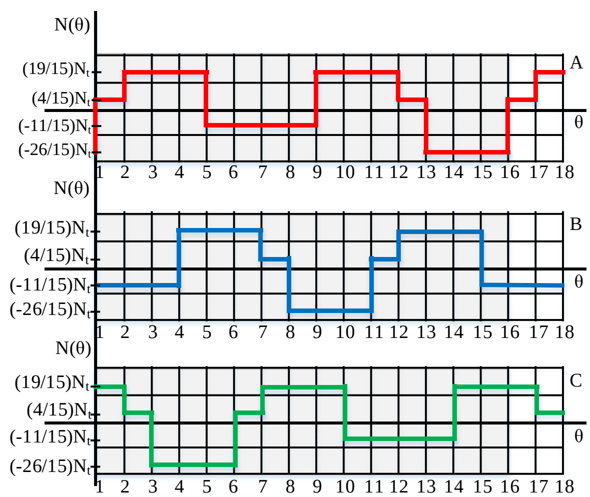


Fig. 3-32. Winding function of the three phases over the first four poles.

### 3.4.3 Field Analysis

A 3D FEA model of the AFMGM was simulated using a 6.4 A/ $mm^2$ current density and 0.6 fill factor. The mesh plot using JMAG FEA software is shown in Fig. 3-33. Fig. 3-34-a shows the axial flux density near the fixed rotor due to the magnets only on the high-speed rotor (rotor 1), with and without the modulation effect of the low-speed rotor. Fig. 3-34-b shows the corresponding harmonic content of the modulated axial flux density. The same plots for the axial flux density near the high-speed rotor due to magnets only on the fixed rotor is shown in Fig. 3-35.

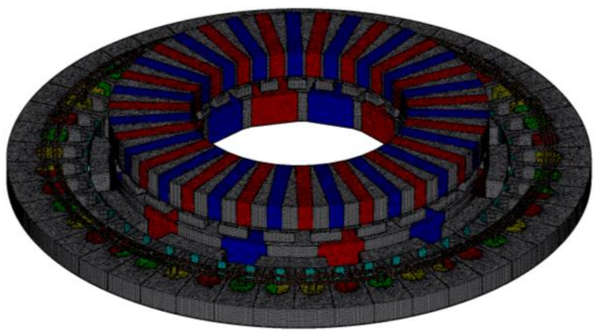

Fig. 3-33. Mesh plot for axial flux magnetically geared machine using JMAG

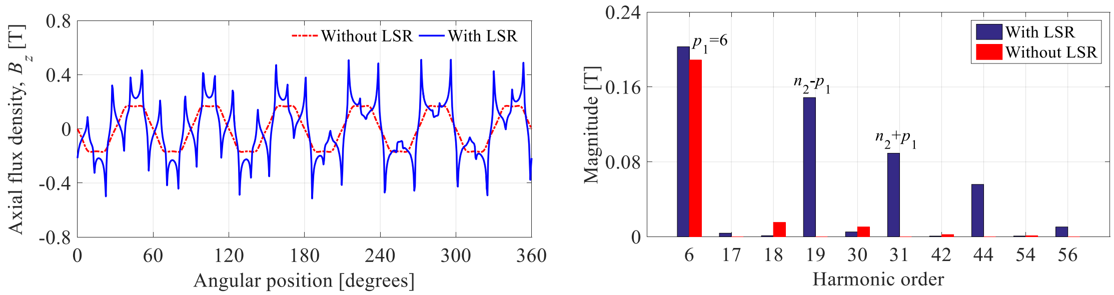


(a) (b)

Fig. 3-34. a) Axial flux density near fixed rotor 3 due to magnets only on the high-speed rotor (rotor 1) at a radius of $r$=137 mm and an axial distance of 0.5 mm. b) Harmonic contents of the modulated flux density.

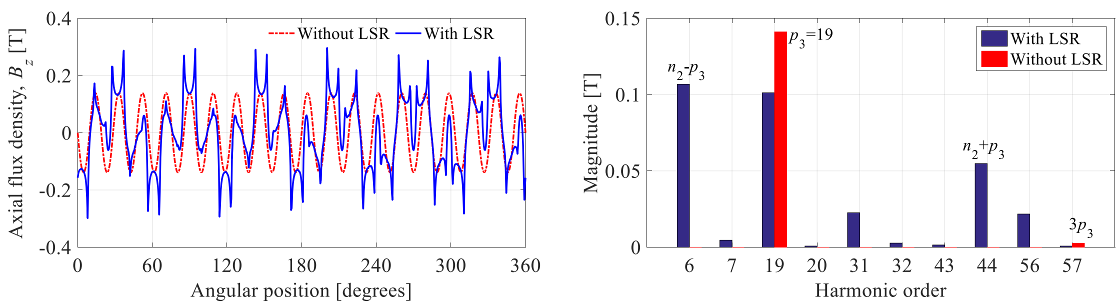


(a) (b)

Fig. 3-35. a) Magnetic flux density near the high-speed rotor due to magnets only on the fixed rotor 3 at a radius of $r$=137 mm and an axial distance of 0.5 mm. b) Harmonic contents of the modulated flux density.

The modulation effect of the low-speed rotor is clearly evident. MMF waveform of the stator winding can be calculated from the three-phase winding functions by multiplying the winding functions with the corresponding phase current magnitude. In order to verify the calculated winding functions, the normalized three-phase MMF of the stator was compared with FEA results when $I_B$=$I_C$=$-0.5I_A$. Fig. 3-36 shows the comparison of the calculated MMF waveforms using FEA and winding function analysis (WFA). The corresponding harmonic content of these two waveforms are shown in Fig. 3-37. The creation of the 6 pole-pairs is clearly evident. The results of the normalized FEA values match very well with WFA.

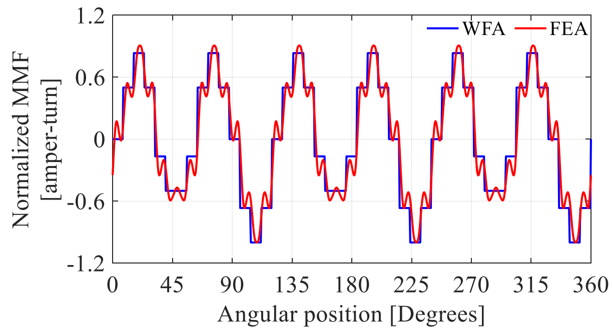


Fig. 3-36. Normalized MMF using the winding function analysis and FEA.

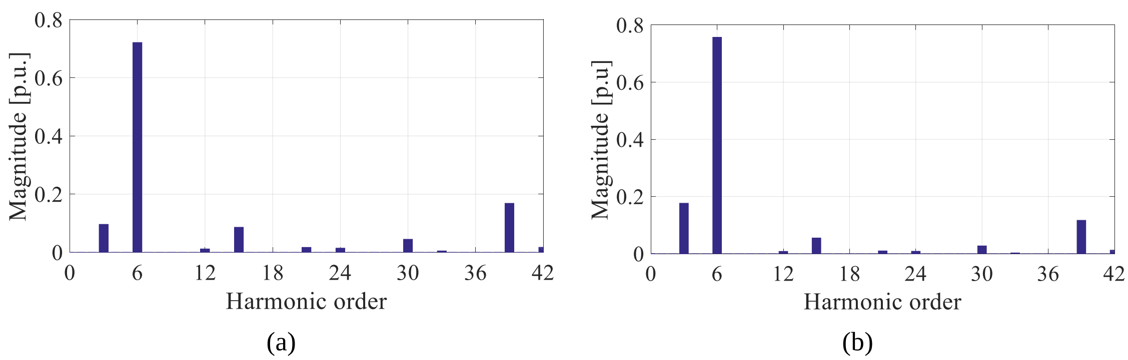


Fig. 3-37. Harmonic contents of the normalized MMF a) using FEA results b) using winding function analysis.

### 3.4.4 Torque Analysis

A three-phase 60 Hz current was applied to the stator windings. The current amplitude and number of winding turns were calculated considering the fill factor of 0.6 and a maximum current density of 6.4 A/mm$^2$. This value of the current density was selected because it results in the peak high-speed rotor torque, $T_1$ being zero. At the same time, the high-speed and low-speed rotors were rotated at $\omega_1$ = 600 r/min and $\omega_2$ = 144 r/min respectively. Fig. 3-38 shows the calculated torque on the different parts of the AFMGM. A summary of the average torque and torque ripple on each part is given in Table 3-VIII. $\omega_1$ is related to the stator frequency, $f_e$, by

$$\omega_1 = 120\times(f_e/2p) = 120\times(60/12) = 600 \text{ rad/s} \tag{3.11}$$

The calculated active region torque density for this AFMGM is 128 Nm/L.

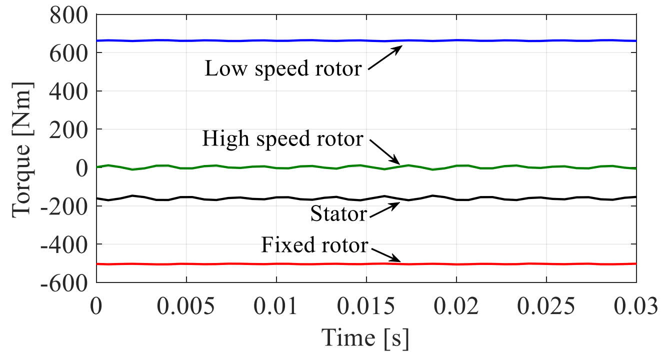


Fig. 3-38. Torque on different parts.

Table 3-VIII. Average Torque and Torque Ripple for Each Part

| | Low-speed rotor | High-speed rotor | Fixed rotor | Stator |
|---|---|---|---|---|
| Average torque | 662Nm | 0Nm | -501Nm | -161Nm |
| Torque ripple | 5.4Nm/0.8% | 22.6Nm | 4.1Nm/0.8% | 22.6Nm/14% |

The stator torque relationship must satisfy

$$T_1 + T_2 + T_3 + T_s = 0 \tag{3.12}$$

and power flow relationship must satisfy

$$T_1\omega_1 + T_2\omega_2 + T_3\omega_3 + T_s\omega_s = P_{loss} \tag{3.13}$$

power loss ,$P_{loss}$ is defined as

$$P_{loss} = P_m + P_h + P_e \tag{3.14}$$

where $P_m$, $P_h$ and $P_e$ are mechanical, hysteresis and eddy current losses respectively.

The high-speed rotor torque, $T_1$ = 0 as it is assumed that power is flowing through the stator and not the high speed rotor shaft. Therefore

$$T_2\omega_2 + T_s\omega_s = P_{loss} \tag{3.15}$$

Injecting current into the stator windings could be used to provide additional overload torque during transient overshoots. In order to examine this possibility, a 3D FEA simulation was performed in which a three-phase current was applied that is directly in-phase with the HSR magnet flux. The stator winding current was varied across the range [0A, 80 $A_{rms}$]. Fig. 3-39 shows the resultant change in the HSR and LSR torque with stator current. In this analysis, a MG air-gap of 1 mm and stator airgap of 0.5 mm were used. The addition of the stator reduced the torque values when there was no current excitation. By using current injection, the HSR torque increased by 151 Nm, a 110% increase, while the torque on LSR increased by 86 Nm, a nearly 15% increase.

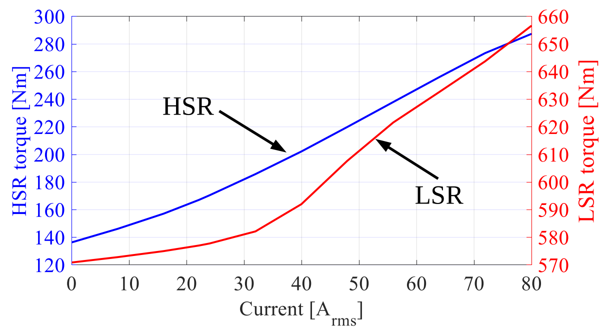


Fig. 3-39. Torque on the low-speed rotor and high- speed rotor as a function of stator current for the case when a fill factor of 0.3 was used. This lower fill factor was used as it was closer to the experimental value used in the prototype. A stator current of 25.4 $A_{rms}$ corresponds to a current density of 6.5A/mm$^2$

### 3.4.5 Experimental Results

The fabricated stator is shown in Fig. 3-40. Due to assembly challenges, the airgap between the rotors was increased to 1 mm and the air-gap between the HSR and the stator lamination was increased to 1.5 mm. Additional ferromagnetic segments (not-shown) also had to be added to enable the stator to be inserted over the AFMG. The stator stack length was decreased to 16.5 mm because the low speed rotor steel bars are fixed using an end ring from outside, which limits the stator space around the HSR. Therefore, to avoid contact between parts, a smaller stack length was needed and the surface of the HSR was raised using additional steel poles.

(a) (b)

Fig. 3-40. The experimentally assembled stator a) lamination with winding, b) mounted on the AFMG.

These design changes resulted in the calculated peak torque and torque density without current excitation reducing to 570.7 Nm and 114 Nm/L, respectively. Due to the space limitations on two ends of the stator, the end-windings needed to be made relatively small. Consequently, this required the number of turns to be reduced from 100 to 20 in the slots. Fig. 3-41 shows the AFMG motor on the test bed.

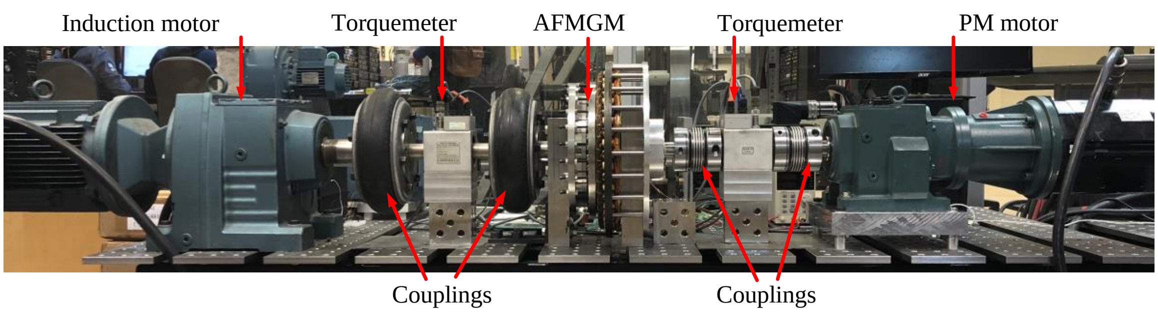


Fig. 3-41. Axial flux magnetically geared machine on the test bed.

The AFMG motor was rotated such that the HSR had a 50 r/min angular speed and the resultant no-load measured back-EMF voltage was then compared with the FEA calculated voltage in Fig. 3-42. The measured value is quite distorted. The harmonic content of the calculated and measured back-EMF is shown in Fig. 3-43. The same harmonics are dominant, but the experimentally measured values are significantly lower and have many additional harmonics. This could be due to high flux leakage and not perfectly uniform airgap. The measured and calculated peak back-EMF at different r/min is shown in Fig. 3-44. This shows a very good agreement with the FEA model.

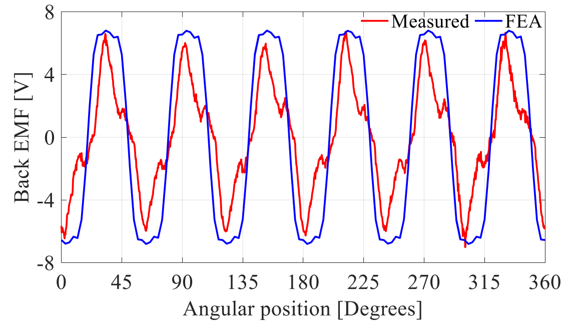


Fig. 3-42. Measured and calculated no-load three phase back-emf waveforms when the HSR is rotating at 50 r/min.

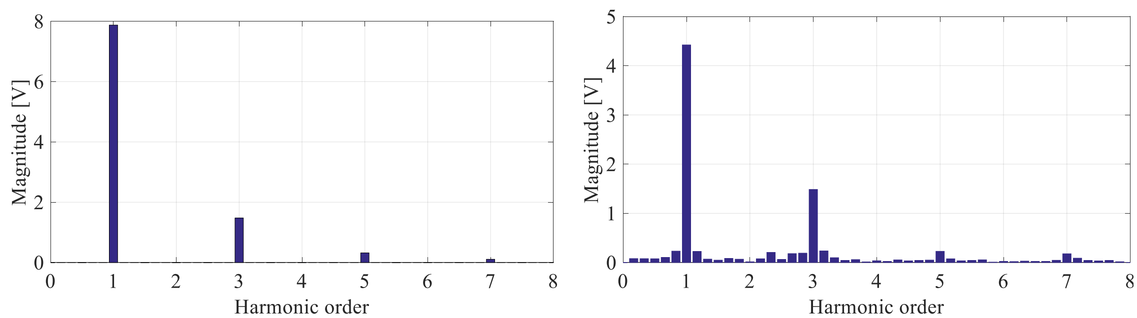


(a) (b)

Fig. 3-43. Harmonic spectrum of the a) calculated and b) measured no load back-emf voltage.

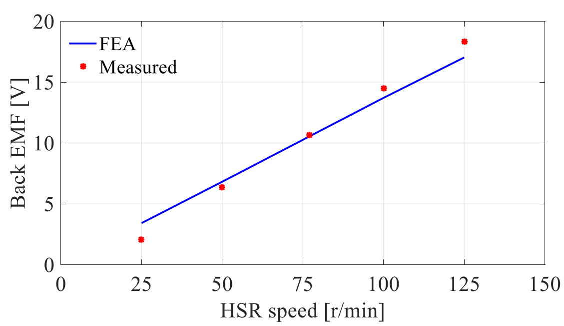


Fig. 3-44. Simulated and measured peak back-EMF at different speeds

The LSR was rotated while no-load was connected to the HSR and the stator. The calculated no-load losses versus HSR speed is shown in Fig. 3-45. The experimentally measured torque on the HSR and LSR is shown in Fig. 3-46. The peak measured torque and corresponding active region torque density are 473 Nm and 94.4 Nm/L.

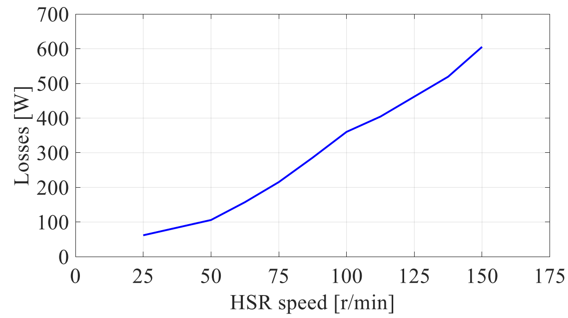

Fig. 3-45. Experimental no-load losses

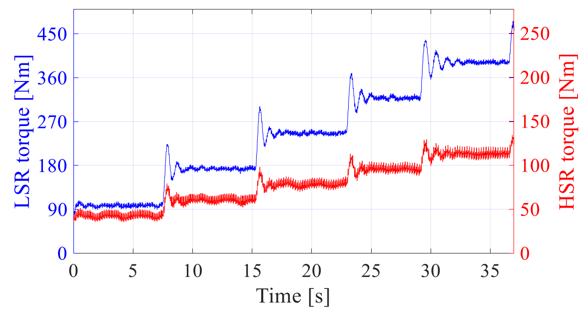


Fig. 3-46. Measured torque at HSR speed of 50 r/min at different loads.

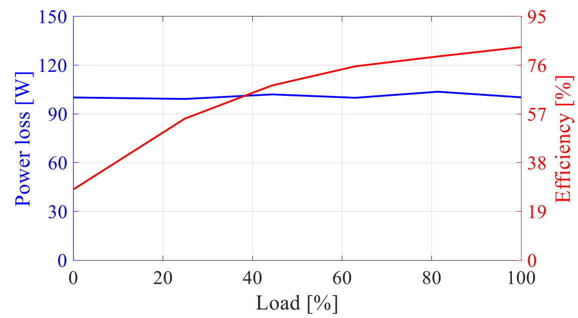


Fig. 3-47. Measured loss and efficiency as a function of load

### 3.4.6 Conclusion

A new type of AFMGM was proposed and investigated. The proposed AFMGM has multiple advantages, including simple and compact design, no need for a separate sets of magnet poles for the stator excitation, and relatively high torque rating capability. The disadvantage of this design is that because of the complex flux path, solid steel poles were used. This limits its applicability to very low-speed applications. The stator of the PM motor was designed with the aim of reducing the torque ripple. The star-of-slots approach was used in order to design the phase windings for this stator. The stator was designed in terms of the number of slots and the winding configuration, but the geometry of the stator was not optimized. Therefore, a further reduction in the torque ripple could be achieved by conducting a more detailed cogging torque analysis. This AFMGM could also be coupled to a suitably-designed linear actuator to achieve a very high torque-to-force ratio actuator.

# 4 Chapter 4: Analytical Model of a Linear Coupling and a Magnetic Lead Screw

This chapter is dedicated to analytical modeling of a linear permanent magnet coupling (LPMC) and a magnetic lead screw (MLS). In section 4.1, an introduction is given. The analytical-based model of the LPMC is developed in section 4.2 and an MLS is modeled using analytical-based method in section 4.3.

## 4.1 Introduction

In order to determine the upper force density bound of magnetic devices a scaling analysis is required. To understand the scaling characteristics and fundamental geometric parameters over a large design space, fast and accurate analysis methods are required. Pure numerical methods like FEA using available commercial software packages are proven to be accurate and effective enough for modeling various electromechanical and electromagnetic devices [25]. However, these FEA simulations are usually computationally expensive requiring a considerable amount of memory and time, especially when using 3D simulation. To address this issue, analytical models of magnetic couplings have been proposed. These methods are based on either equivalent current sheet or equivalent charge sheet models of PM poles [81]. Xiong *et al.* [82] proposed a model for a flat single-sided PM linear machine based on the concept of magnetic charge and used the method of images. An ideal permanent magnet ($\mu_r$ = 1) was considered in this model, which resulted in modeling the PMs with only surface charges. This resulted did not incorporate the relative permeability of the magnet material. As the model was discretized, the final results include summation terms within integrals, which makes this method complicated and time consuming. 2D analytical models based on magnetic vector potential were proposed in [83], [84] for flat PM linear machines. PM poles were modeled using equivalent current sheets. The relative permeability of the magnet material was not considered in these proposed methods. Wang *et al.* [85] developed an analytical model for tubular PM machines based on the magnetic scalar potential. The advantage of using the scalar potential over the vector potential is that the vector potential requires three vector components to be used whilst the scalar potential utilizes a single scalar term. However, the scalar potential method is only applicable in current-free problems [86]. Therefore, magnetic charge must be used to model the fields.

Wave energy power generation [87], energy storage mechanisms [88], and linear magnetic springs [89] are some examples of applications that could use LPMC. More generally, the field interaction between two linear PM cylinders can be considered to be near the force limit of what is possible for non-superconducting linear motion devices. Therefore, developing an analytical-based model helps with understanding the scaling and fundamental geometric parameters that govern linear motion magneto-mechanical devices.

In this chapter, analytical-based scalar potential models of a LPMC and an MLS are developed. The effects of various dimensional ratios on the mass and volumetric force density performance of each device is investigated. The analysis shows the effectiveness of the proposed modeling method in parametric analysis and design optimization of the linear magnetic devices. The results provides the upper force density capability of the linear-based magnetic devices.

### 4.2 Analytical-Based Model for Halbach Linear Permanent Magnet Coupling

The PM configuration for the LPMC can be formed using a radial, axial or Halbach magnet array arrangement [25]. Due to its unique characteristics, the Halbach array arrangement has recently attracted more attention. It was originally discovered as a one-sided flux structure by Mallinson [90], subsequently it was realized using individual magnets by Halbach [91]. The Halbach array is ideally a rotating magnetization vector with constant amplitude. Depending on the rotation direction, one side has almost zero flux while the other side has a sinusoidal magnetic field. Fig. 4-1 shows a 2D sketch of one period of a Halbach array for a LPMC. It consist of four magnet pieces per pole-pair, including radially and axially magnetized magnets. This unique magnet structure offers a variety of benefits. Such as, a higher torque/force capabilities [92]; a lower torque/force ripple [83]; and back-iron is not necessary due to the inherently self-shielded structure [93]. For these reasons, the Halbach magnet array structure will be used in the LPMC. The magnetization curves due to this configuration are shown in Fig. 4-2.

The vector representation of this Halbach array is:

$$\mathrm{M} = M_r(z_I)\hat{\mathrm{r}} + M_z(z_I)\hat{\mathrm{z}} \tag{4.1}$$

and its corresponding Fourier series is:

$$\mathrm{M} = \sum_{n=1}^{\infty} a_n \cos\left(\frac{2\pi n}{T_I} z_I\right)\hat{\mathrm{r}} + \sum_{n=1}^{\infty} b_n \sin\left(\frac{2\pi n}{T_I} z_I\right)\hat{\mathrm{z}} \tag{4.2}$$

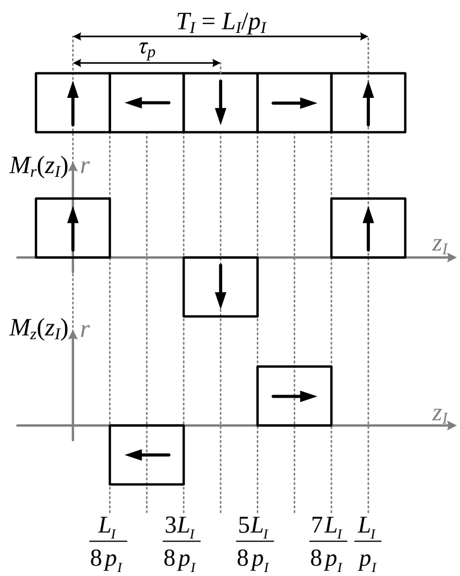


Fig. 4-1. One period of the Halbach array

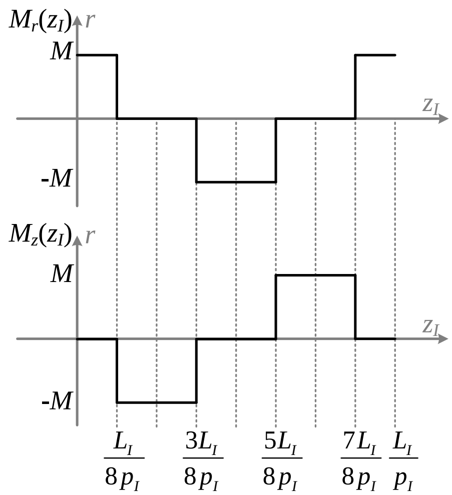


Fig. 4-2. Magnetization plots of the Halbach array

where

$$a_n = \frac{4}{T_I}\int_0^{T_I/2} M_r(z_I)\cos(\frac{2\pi n}{T_I}z_I)dz_I \tag{4.3}$$

and

$$b_n = \frac{4}{T_I}\int_0^{T_I/2} M_z(z_I)\sin(\frac{2\pi n}{T_I}z_I)dz_I \tag{4.4}$$

where $T_I$ is the Halbach array period and is defined as:

$$T_I = \frac{L_I}{p_I} \tag{4.5}$$

where $L_I$ is the axial length and $p_I$ is the number of pole-pairs. Noting the step change magnetizing values in Fig. 4-1 and using half-wave symmetry, (4.3) and (4.4) can be evaluated as:

$$a_n = \frac{4}{L_I/p_I}[\int_0^{L_I/8p_I} M\cos(\frac{2\pi p_I n}{L_I}z_I)dz_I - \int_{3L_I/8p_I}^{L_I/2p_I} M\cos(\frac{2\pi p_I n}{L_I}z_I)dz_I] \tag{4.6}$$

$$b_n = \frac{-4}{L_I / p_I}[\int_{L_I/8p_I}^{3L_I/8p_I} M \sin(\frac{2\pi p_I n}{L_I} z_I) dz_I] \tag{4.7}$$

From (4.6) one can calculate:

$$\begin{aligned} a_n &= \frac{4M}{L_I / p_I} \frac{L_I}{2\pi p_I n}[\sin(\frac{2\pi p_I n}{L_I} z_I)\Big|_0^{L_I/8p_I} - \sin(\frac{2\pi p_I n}{L_I} z_I)\Big|_{3L_I/8p_I}^{L_I/2p_I}] \\ &= \frac{2M}{n\pi}[\sin(\frac{n\pi}{4}) - \sin(n\pi) + \sin(\frac{3n\pi}{4})] \end{aligned} \tag{4.8}$$

Using the trigonometric identity:

$$\sin\alpha \pm \sin\beta = 2\sin(\frac{\alpha \pm \beta}{2})\cos(\frac{\alpha \mp \beta}{2}) \tag{4.9}$$

Equation (4.8) becomes:

$$a_n = \frac{2M}{n\pi}[2\sin(\frac{n\pi}{2})\cos(\frac{n\pi}{4})] \tag{4.10}$$

or

$$a_n = \begin{cases} \frac{4M}{n\pi}[\sin(\frac{n\pi}{2})\cos(\frac{n\pi}{4})] & , n \text{ odd} \\ 0 & , n \text{ even} \end{cases} \tag{4.11}$$

And calculating (4.7) gives:

$$\begin{aligned} b_n &= \frac{4M}{L_I / p_I} \frac{L_I}{2\pi p_I n} \cos(\frac{2\pi p_I n}{L_I} z_I)\Big|_{L_I/8p_I}^{3L_I/8p_I} \\ &= \frac{2M}{n\pi}[\cos(\frac{3n\pi}{4}) - \cos(\frac{n\pi}{4})] \end{aligned} \tag{4.12}$$

Using the trigonometric identity:

$$\cos\alpha - \cos\beta = -2\sin(\frac{\alpha+\beta}{2})\sin(\frac{\alpha-\beta}{2}) \tag{4.13}$$

Equation (4.12) becomes:

$$b_n = \frac{2M}{n\pi}[-2\sin(\frac{n\pi}{2})\sin(\frac{n\pi}{4})] \tag{4.14}$$

or

$$b_n = \begin{cases} -\frac{4M}{n\pi}[\sin(\frac{n\pi}{2})\sin(\frac{n\pi}{4})] & , n \text{ odd} \\ 0 & , n \text{ even} \end{cases} \tag{4.15}$$

Substituting (4.10) and (4.14) into (4.2) gives:

$$\begin{aligned} \mathbf{M} = & \frac{4M}{\pi}\sum_{n=1}^{\infty}\frac{1}{2n-1}\sin[\frac{(2n-1)\pi}{2}]\cos[\frac{(2n-1)\pi}{4})]\cos[(2n-1)k_I z_I]\,\hat{\mathbf{r}} \\ & -\frac{4M}{\pi}\sum_{n=1}^{\infty}\frac{1}{2n-1}\sin[\frac{(2n-1)\pi}{2}]\sin[\frac{(2n-1)\pi}{4}]\sin[(2n-1)k_I z_I]\,\hat{\mathbf{z}} \end{aligned} \tag{4.16}$$

where $k_I$ is defined as:

$$k_I = \frac{2\pi}{T_I} \tag{4.17}$$

For the first harmonic ($n$ = 1), from (4.10) and (4.14) one can obtain:

$$|a_1| = |b_1| = 0.9003M \tag{4.18}$$

Therefore, the fundamental magnetization vector magnitude, $M_f$, can be defined as:

$$M_f = c_1 M \tag{4.19}$$

where:

$$c_1 = 0.9003 \tag{4.20}$$

The magnitude of the different harmonics were calculated using (4.10) and (4.14) and plotted in Fig. 4-3.

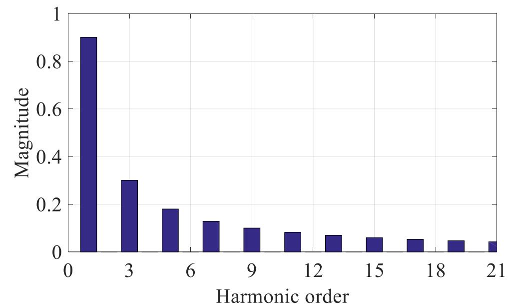


Fig. 4-3. Harmonic spectrum of the magnetization

The geometry of the inner part of the Halbach LPMC in the cylindrical coordinate system is depicted in Fig. 4-4. Cylindrical surfaces $S_o^I$ and $S_i^I$ are located at $r = r_{Io}$ and $r = r_{Ii}$, respectively, and a volume $V^I$ is defined in between these two surfaces.

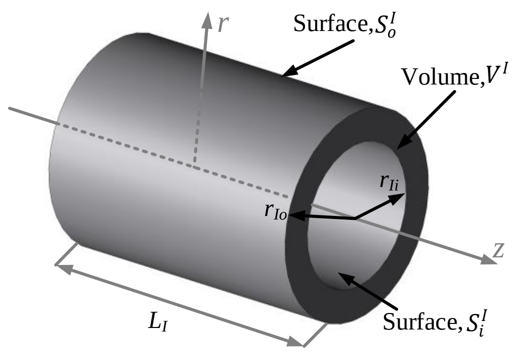


Fig. 4-4. Geometry definition for inner part of the linear coupling

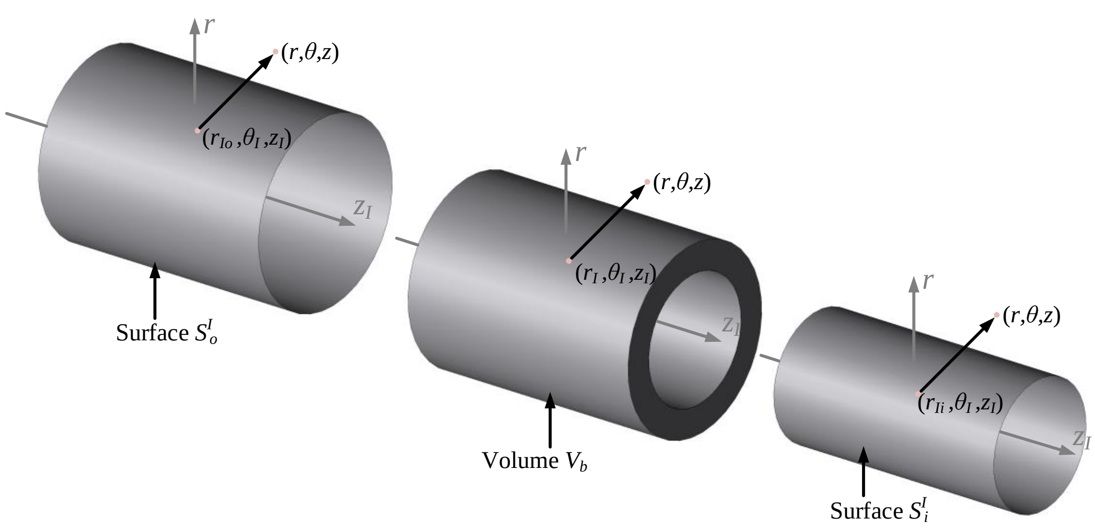


Fig. 4-5. Point charge and related coordinate parameters

A point charge is defined as shown in Fig. 4-5. In order to calculate the magnetic field of this Halbach cylinder at an arbitrary point of ($r$, $\theta$, $z$), two surface charge densities of $\sigma_{mo}^I$ and $\sigma_{mi}^I$ and one volume charge density of $\rho_m^I$ are defined for surface $S_o^I$, surface $S_i^I$ and volume $V^I$, respectively.

For a current-free problem, the magnetostatic Maxwell's equations are as follow [94]:

$$\nabla \cdot \mathbf{B} = 0 \tag{4.21}$$

$$\nabla \times \mathbf{H} = 0 \tag{4.22}$$

where **B** and **H** are magnetic flux density and field intensity, respectively, which are related as:

$$\mathbf{B} = \mu_0(\mathbf{H} + \mathbf{M}) \tag{4.23}$$

where **M** is the magnetization and $\mu_0$ is the permeability of the space. The relationship between the magnetization and the magnetic field in a magnetic material can be defined using magnetic constitutive law [94]:

$$\mathbf{M} = \chi_m \mathbf{H} + \mathbf{M}_m \tag{4.24}$$

where $\chi_m$ is the magnetic susceptibility and $\mathbf{M}_\mathrm{m}$ is the PM magnetization vector, which is independent of the external field and defined as:

$$\mathbf{M}_\mathbf{m} = \mathbf{B}_m / \mu_0 \tag{4.25}$$

where $\mathbf{B}_m$ is the remnant flux density of the permanent magnet. Substituting (4.24) into (4.23) gives:

$$\begin{aligned} \mathbf{B} &= \mu_0(\mathbf{H} + \chi_m \mathbf{H} + \mathbf{M}_m) \\ &= \mu_0 \mu_r \mathbf{H} + \mu_0 \mathbf{M}_m \\ &= \mu \mathbf{H} + \mu_0 \mathbf{M}_m \end{aligned} \tag{4.26}$$

where $\mu_r$ = 1+ $\chi_m$ is the relative permeabilty and $\mu$ is the permeability of the material. In free space (4.26), reduces down to:

$$\mathbf{B} = \mu_0 \mathbf{H} \tag{4.27}$$

In order to solve for the magnetic field, the magnetic scalar potential, $\phi$, is defined, which relates to the magnetic field intensity by [95]:

$$\mathbf{H} = -\nabla\phi \tag{4.28}$$

Taking the divergence of both sides of (4.26) gives:

$$\nabla\cdot\mathbf{B} = \mu\nabla\cdot\mathbf{H} + \mu_0\nabla\cdot\mathbf{M}_m \tag{4.29}$$

Substituting (4.21) and (4.28) into (4.29) gives:

$$\nabla^2\phi = \frac{\nabla\cdot\mathbf{M}_m}{\mu_r} \tag{4.30}$$

Equation (4.30) is a second order scalar equation. As the magnetization imediately becomes zero outside the permanent magnet one has:

$$\nabla^2\phi = 0 \tag{4.31}$$

The integral solution to (4.31) in cylinderical coordinate system becomes [95]:

$$\begin{aligned}\phi^I(r,\theta,z) = {} & \frac{1}{4\pi\mu_r}\iiint_{V^I}\frac{\nabla\cdot\mathbf{M}_m}{\mathrm{R}(r,\theta,z,r_I,\theta_I,z_I)}r_I dr_I d\theta_I dz_I \\ & +\frac{1}{4\pi}\iint_{S_o^I}\frac{\hat{\mathrm{r}}\cdot\mathbf{M}_m}{\mathrm{R}(r,\theta,z,r_{Io},\theta_I,z_I)}r_{Io} d\theta_I dz_I \\ & -\frac{1}{4\pi}\iint_{S_i^I}\frac{\hat{\mathrm{r}}\cdot\mathbf{M}_m}{\mathrm{R}(r,\theta,z,r_{Ii},\theta_I,z_I)}r_{Ii} d\theta_I dz_I\end{aligned} \tag{4.32}$$

where R can be defined using the law of cosine:

$$\mathrm{R}(r,\theta,z,r_I,\theta_I,z_I) = \sqrt{r^2 + r_I^2 + 2rr_I\cos(\theta-\theta_I) + (z-z_I)^2} \tag{4.33}$$

Considering the numerator terms in (4.32), the volume and surface charges are defined as follow:

$$\rho_m^I = -\frac{\nabla \cdot \mathbf{M}_m}{\mu_r}, \text{ in volume } V^I \tag{4.34}$$

$$\sigma_{mo}^I = +\hat{\boldsymbol{r}} \cdot \mathbf{M}_m, \text{ on surface } S_o^I \tag{4.35}$$

$$\sigma_{mi}^I = -\hat{\boldsymbol{r}} \cdot \mathbf{M}_m, \text{ on surface } S_i^I \tag{4.36}$$

Therefore, the magnetic scalar potential created by a surface and volumetric magnetic charge function is given by:

$$\begin{aligned}\phi^I(r,\theta,z) = &\frac{1}{4\pi}\int_0^{2\pi}\int_{-L_I/2}^{L_I/2}\int_{r_{Ii}}^{r_{Io}} \frac{\rho_m^I(z_I)}{\mathrm{R}(r,\theta,z,r_I,\theta_I,z_I)} r_I dr_I d\theta_I dz_I \\ &+\frac{1}{4\pi}\int_{-L_I/2}^{L_I/2}\int_0^{2\pi} \frac{\sigma_{mo}^I(z_I)}{\mathrm{R}(r,\theta,z,r_{Io},\theta_I,z_I)} r_{Io} d\theta_I dz_I \\ &+\frac{1}{4\pi}\int_{-L_I/2}^{L_I/2}\int_0^{2\pi} \frac{\sigma_{mi}^I(z_I)}{\mathrm{R}(r,\theta,z,r_{Ii},\theta_I,z_I)} r_{Ii} d\theta_I dz_I\end{aligned} \tag{4.37}$$

Since [95]

$$\nabla \cdot \mathbf{M} = \frac{1}{r}M_r + \frac{1}{r}\frac{\partial M_r}{\partial r} + \frac{1}{r}\frac{\partial M_\theta}{\partial \theta} + \frac{\partial M_z}{\partial z} \tag{4.38}$$

Substituting (4.2) into (4.38) gives:

$$\nabla \cdot \mathbf{M} = \frac{1}{r_I}\sum_{n=1}^{\infty} a_n \cos(nk_I z_I) + k_I \sum_{n=1}^{\infty} nb_n \cos(nk_I z_I) \tag{4.39}$$

or

$$\nabla \cdot \mathbf{M} = \sum_{n=1}^{\infty}[\frac{1}{r_I}a_n + k_I nb_n]\cos(nk_I z_I) \tag{4.40}$$

Therefore, substituting (4.40) into (4.34) gives:

$$\rho_m^I(z_I) = -\sum_{n=1}^{\infty}[\frac{1}{\mu_r r_I}a_n + \frac{k_I}{\mu_r}nb_n]\cos(nk_I z_I), \text{ in volume } V^I \tag{4.41}$$

Substituting (4.1) into (4.35) and (4.36) gives:

$$\sigma_{mo}^I(z_I) = \sum_{n=1}^{\infty} a_n \cos(nk_I z_I), \text{ on surface } S_o^I \tag{4.42}$$

$$\sigma_{mi}^I(z_I) = -\sum_{n=1}^{\infty} a_n \cos(nk_I z_I), \text{ on surface } S_i^I \tag{4.43}$$

Considering just the fundamental component (4.41)-(4.43) become:

$$\rho_m^I(z_I) = -\frac{M_f}{r_I \mu_r}(1 - k_I r_I)\cos(k_I z_I) \tag{4.44}$$

$$\sigma_{mo}^I(z_I) = M_f \cos(k_I z_I) \tag{4.45}$$

$$\sigma_{mi}^I(z_I) = -M_f \cos(k_I z_I) \tag{4.46}$$

where $M_f$ is the fundamental magnitude of magnetization defined by (4.19).

Substituting (4.44)-(4.46) into (4.37) gives:

$$\begin{aligned}\phi^I(r,\theta,z) = {} & \frac{M_f}{4\pi}\int_{-L_I/2}^{L_I/2}\int_0^{2\pi}\frac{r_{Io}\cos(k_I z_I)d\theta_I dz_I}{\mathrm{R}(r, r_{Io}, \theta - \theta_I, z, z_I)} \\ & -\frac{M_f}{4\pi}\int_{-L_I/2}^{L_I/2}\int_0^{2\pi}\frac{r_{Ii}\cos(k_I z_I)d\theta_I dz_I}{\mathrm{R}(r, r_{Ii}, \theta - \theta_I, z, z_I)} \\ & -\frac{M_f}{4\pi\mu_r}\int_{-L_I/2}^{L_I/2}\int_0^{2\pi}\int_{r_{Ii}}^{r_{Io}}\frac{\cos(k_I z_I)(1 - k_I r_I)dr_I d\theta_I dz_I}{\mathrm{R}(r, r_I, \theta - \theta_I, z, z_I)}\end{aligned} \tag{4.47}$$

The magnetic scalar potential is separated into three terms for surfaces $S_o^I$ and $S_i^I$ and volume $V^I$ as follow:

$$\phi^I(r,\theta,z) = \phi_{So}^I(r,\theta,z) + \phi_{Si}^I(r,\theta,z) + \phi_V^I(r,\theta,z) \tag{4.48}$$

where:

$$\phi_{So}^{I}(r,\theta,z)=\frac{M_f}{4\pi}\int_{-L_I/2}^{L_I/2}\int_{0}^{2\pi}\frac{r_{Io}\cos(k_I z_I)d\theta_I dz_I}{\mathrm{R}(r,\theta,z,r_{Io},\theta_I,z_I)} \tag{4.49}$$

$$\phi_{Si}^{I}(r,\theta,z)=-\frac{M_f}{4\pi}\int_{-L_I/2}^{L_I/2}\int_{0}^{2\pi}\frac{r_{Ii}\cos(k_I z_I)d\theta_I dz_I}{\mathrm{R}(r,\theta,z,r_{Ii},\theta_I,z_I)} \tag{4.50}$$

$$\phi_{V}^{I}(r,\theta,z)=-\frac{M_f}{4\pi\mu_r}\int_{-L_I/2}^{L_I/2}\int_{0}^{2\pi}\int_{r_{Ii}}^{r_{Io}}\frac{\cos(k_I z_I)(1-k_I r_I)dr_I d\theta_I dz_I}{\mathrm{R}(r,\theta,z,r_I,\theta_I,z_I)} \tag{4.51}$$

Substituting (4.33) back into (4.49)-(4.51) gives:

$$\phi_{So}^{I}(r,\theta,z)=\frac{M_f}{4\pi}\int_{-L_I/2}^{L_I/2}\int_{0}^{2\pi}\frac{r_{Io}\cos(k_I z_I)d\theta_I dz_I}{\sqrt{r^2+r_{Io}^2-2rr_{Io}\cos(\theta-\theta_I)+(z-z_I)^2}} \tag{4.52}$$

$$\phi_{Si}^{I}(r,\theta,z)=-\frac{M_f}{4\pi}\int_{-L_I/2}^{L_I/2}\int_{0}^{2\pi}\frac{r_{Ii}\cos(k_I z_I)d\theta_I dz_I}{\sqrt{r^2+r_{Ii}^2-2rr_{Ii}\cos(\theta-\theta_I)+(z-z_I)^2}} \tag{4.53}$$

$$\phi_{V}^{I}(r,\theta,z)=-\frac{M_f}{4\pi\mu_r}\int_{-L_I/2}^{L_I/2}\int_{0}^{2\pi}\int_{r_{Ii}}^{r_{Io}}\frac{\cos(k_I z_I)(1-k_I r_I)dr_I d\theta_I dz_I}{\sqrt{r^2+r_I^2-2rr_I\cos(\theta-\theta_I)+(z-z_I)^2}} \tag{4.54}$$

### 4.2.1 Magnetic Flux Density for Linear Permanent Magnet Coupling

Magnetic flux density is determined by substituting (4.37) into (4.28). This gives [96]:

$$\begin{aligned}\mathbf{B}^{I}(r,\theta,z)=\frac{\mu_0}{4\pi}\{&\iiint_v\frac{\rho_m^I(z_I)\mathbf{R}(r,\theta,z,r_I,\theta_I,z_I)}{[r^2+r_I^2-2rr_I\cos(\theta-\theta_I)+(z-z_I)^2]^{3/2}}dv\\&+\iint_s\frac{\sigma_{mo}^I(z_I)\mathbf{R}(r,\theta,z,r_{Io},\theta_I,z_I)}{[r^2+r_{Io}^2-2rr_{Io}\cos(\theta-\theta_I)+(z-z_I)^2]^{3/2}}ds\\&+\iint_s\frac{\sigma_{mi}^I(z_I)\mathbf{R}(r,\theta,z,r_{Ii},\theta_I,z_I)}{[r^2+r_{Ii}^2-2rr_{Ii}\cos(\theta-\theta_I)+(z-z_I)^2]^{3/2}}ds\}\end{aligned} \tag{4.55}$$

where:

$$\mathbf{R}(r,\theta,z,r_I,\theta_I,z_I)=[r-r_I\cos(\theta-\theta_I)]\hat{\mathbf{r}}+[r_I\sin(\theta-\theta_I)]\hat{\boldsymbol{\theta}}+(z-z_I)\hat{\mathbf{z}} \tag{4.56}$$

Substituting (4.44)-(4.46) into (4.55) gives:

$$\begin{aligned}\mathbf{B}^I(r,\theta,z)=&-\frac{\mu_0 M_f}{4\pi\mu_r}\int_0^{2\pi}\int_{-L_I/2}^{L_I/2}\int_{r_{Ii}}^{r_{Io}}\frac{(1-k_I r_I)\cos(k_I z_I)\mathbf{R}(r,\theta,z,r_I,\theta_I,z_I)}{[r^2+r_I^2-2rr_I\cos(\theta-\theta_I)+(z-z_I)^2]^{3/2}}dr_I d\theta_I dz_I\\&+\frac{\mu_0 M_f}{4\pi}\int_{-L_I/2}^{L_I/2}\int_0^{2\pi}\frac{r_{Io}\cos(k_I z_I)\mathbf{R}(r,\theta,z,r_{Io},\theta_I,z_I)}{[r^2+r_{Io}^2-2rr_{Io}\cos(\theta-\theta_I)+(z-z_I)^2]^{3/2}}d\theta_I dz_I\\&-\frac{\mu_0 M_f}{4\pi}\int_{-L_I/2}^{L_I/2}\int_0^{2\pi}\frac{r_{Ii}\cos(k_I z_I)\mathbf{R}(r,\theta,z,r_{Ii},\theta_I,z_I)}{[r^2+r_{Ii}^2-2rr_{Ii}\cos(\theta-\theta_I)+(z-z_I)^2]^{3/2}}d\theta_I dz_I\end{aligned} \tag{4.57}$$

Substituting (4.56) into (4.57), one can calculate different components of the magnetic flux density:

$$\begin{aligned}B_r^I(r,\theta,z)=&-\frac{\mu_0 M_f}{4\pi\mu_r}\int_0^{2\pi}\int_{-L_I/2}^{L_I/2}\int_{r_{Ii}}^{r_{Io}}\frac{(1-k_I r_I)\cos(k_I z_I)[r-r_I\cos(\theta-\theta_I)]}{[r^2+r_I^2-2rr_I\cos(\theta-\theta_I)+(z-z_I)^2]^{3/2}}dr_I d\theta_I dz_I\\&+\frac{\mu_0 M_f}{4\pi}\int_{-L_I/2}^{L_I/2}\int_0^{2\pi}\frac{r_{Io}\cos(k_I z_I)[r-r_{Io}\cos(\theta-\theta_I)]}{[r^2+r_{Io}^2-2rr_{Io}\cos(\theta-\theta_I)+(z-z_I)^2]^{3/2}}d\theta_I dz_I\\&-\frac{\mu_0 M_f}{4\pi}\int_{-L_I/2}^{L_I/2}\int_0^{2\pi}\frac{r_{Ii}\cos(k_I z_I)[r-r_{Ii}\cos(\theta-\theta_I)]}{[r^2+r_{Ii}^2-2rr_{Ii}\cos(\theta-\theta_I)+(z-z_I)^2]^{3/2}}d\theta_I dz_I\end{aligned} \tag{4.58}$$

The radial integral term in (4.58) can be evaluated by using:

$$\begin{aligned}&\psi_1(r,\theta,z,r_I,\theta_I,z_I)=\int\frac{(1-k_I r_I)[r-r_I\cos(\theta-\theta_I)]}{[r^2+r_I^2-2rr_I\cos(\theta-\theta_I)+(z-z_I)^2]^{3/2}}dr_I=\\&\frac{rr_I-r^2\cos(\theta-\theta_I)-[k_I r+\cos(\theta-\theta_I)][(z-z_I)^2+r^2-rr_I\cos(\theta-\theta_I)]}{\mathrm{R}(r,\theta,z,r_I,\theta_I,z_I)[r^2-r^2\cos^2(\theta-\theta_I)+(z-z_I)^2]}\\&-\frac{k_I\cos(\theta-\theta_I)\{r_I[(z-z_I)^2-r^2\cos^2(\theta-\theta_I)+r^2]+r\cos(\theta-\theta_I)[(z-z_I)^2+r^2]\}}{\mathrm{R}(r,\theta,z,r_I,\theta_I,z_I)[r^2-r^2\cos^2(\theta-\theta_I)+(z-z_I)^2]}\\&+k_I\cos(\theta-\theta_I)\mathrm{Ln}[r_I-r\cos(\theta-\theta_I)+\mathrm{R}(r,\theta,z,r_I,\theta_I,z_I)]\end{aligned} \tag{4.59}$$

Therefore, all terms in (4.58) then reduce down to double integrals:

$$B_r^I(r,\theta,z) = -\frac{\mu_0 M_f}{4\pi\mu_r}\int_{-L_I/2}^{L_I/2}\int_0^{2\pi}\cos(k_I z_I)[\psi_1(r,\theta,z,r_{Io}) - \psi_1(r,\theta,z,r_{Ii})]d\theta_I dz_I$$
$$+\frac{\mu_0 M_f}{4\pi}\int_{-L_I/2}^{L_I/2}\int_0^{2\pi}\frac{r_{Io}\cos(k_I z_I)[r - r_{Io}\cos(\theta-\theta_I)]}{[r^2 + r_{Io}^2 - 2rr_{Io}\cos(\theta-\theta_I) + (z-z_I)^2]^{3/2}}d\theta_I dz_I \tag{4.60}$$
$$-\frac{\mu_0 M_f}{4\pi}\int_{-L_I/2}^{L_I/2}\int_0^{2\pi}\frac{r_{Ii}\cos(k_I z_I)[r - r_{Ii}\cos(\theta-\theta_I)]}{[r^2 + r_{Ii}^2 - 2rr_{Ii}\cos(\theta-\theta_I) + (z-z_I)^2]^{3/2}}d\theta_I dz_I$$

The $B_\theta$ component can be calculated as follow:

$$B_\theta^I(r,\theta,z) = -\frac{\mu_0 M_f}{4\pi\mu_r}\int_{-L_I/2}^{L_I/2}\int_0^{2\pi}\int_{r_{Ii}}^{r_{Io}}\frac{(1-k_I r_I)\cos(k_I z_I)[r_I\sin(\theta-\theta_I)]}{[r^2 + r_I^2 - 2rr_I\cos(\theta-\theta_I) + (z-z_I)^2]^{3/2}}dr_I d\theta_I dz_I$$
$$+\frac{\mu_0 M_f}{4\pi}\int_{-L_I/2}^{L_I/2}\int_0^{2\pi}\frac{r_{Io}\cos(k_I z_I)[r_{Io}\sin(\theta_a)]}{[r^2 + r_{Io}^2 - 2rr_{Io}\cos(\theta-\theta_I) + (z-z_I)^2]^{3/2}}d\theta_I dz_I \tag{4.61}$$
$$-\frac{\mu_0 M_f}{4\pi}\int_{-L_I/2}^{L_I/2}\int_0^{2\pi}\frac{r_{Ii}\cos(k_I z_I)[r_{Ii}\sin(\theta-\theta_I)]}{[r^2 + r_{Ii}^2 - 2rr_{Ii}\cos(\theta-\theta_I) + (z-z_I)^2]^{3/2}}d\theta_I dz_I$$

Using integral solution:

$$\psi_2(r,\theta,z,r_I,\theta_I,z_I) = \int\frac{(1-k_I r_I)r_I}{[r^2 + r_I^2 - 2rr_I\cos(\theta-\theta_I) + (z-z_I)^2]^{3/2}}dr_I =$$
$$\frac{k_I r_I[(z-z_I)^2 - 2r^2\cos^2(\theta-\theta_I)]}{\mathrm{R}(r,\theta,z,r_I,\theta_I,z_I)[r^2 - r^2\cos^2(\theta-\theta_I) + (z-z_I)^2]} \tag{4.62}$$
$$+\frac{[r^2 + (z-z_I)^2][kr\cos(\theta-\theta_I) - 1] + rr_I\cos(\theta-\theta_I)}{\mathrm{R}(r,\theta,z,r_I,\theta_I,z_I)[r^2 - r^2\cos^2(\theta-\theta_I) + (z-z_I)^2]}$$
$$-k\mathrm{Ln}[r_I - r\cos(\theta-\theta_I) + \mathrm{R}(r,\theta,z,r_I,\theta_I,z_I)]$$

Equation (4.61) reduces down to:

$$B_\theta^I = \frac{-\mu_0 M_f}{4\pi\mu_r}\int_{-L_I/2}^{L_I/2}\int_0^{2\pi}\cos(k_I z_I)\sin(\theta-\theta_I)[\psi_2(r,\theta,z,r_{Io},\theta_I,z_I) - \psi_2(r,\theta,z,r_{Ii},\theta_I,z_I)]d\theta_I dz_I$$
$$+\frac{\mu_0 M_f}{4\pi}\int_{-L_I/2}^{L_I/2}\int_0^{2\pi}\frac{r_{Io}\cos(k_I z_I)[r_{Io}\sin(\theta-\theta_I)]}{[r^2 + r_{Io}^2 - 2rr_{Io}\cos(\theta-\theta_I) + (z-z_I)^2]^{3/2}}d\theta_I dz_I \tag{4.63}$$
$$-\frac{\mu_0 M_f}{4\pi}\int_{-L_I/2}^{L_I/2}\int_0^{2\pi}\frac{r_{Ii}\cos(k_I z_I)[r_{Ii}\sin(\theta-\theta_I)]}{[r^2 + r_{Ii}^2 - 2rr_{Ii}\cos(\theta-\theta_I) + (z-z_I)^2]^{3/2}}d\theta_I dz_I$$

The axial component of the magnetic flux density can be calculated as:

$$B_z^I(r,\theta,z)=\frac{\mu_0 M_f}{4\pi\mu_r}\int_{-L_I/2}^{L_I/2}\int_0^{2\pi}\int_{r_{Ii}}^{r_{Io}}\frac{(1-k_I r_I)\cos(k_I z_I)(z-z_I)}{[r^2+r_I^2-2rr_I\cos(\theta-\theta_I)+(z-z_I)^2]^{3/2}}dr_I d\theta_I dz_I$$

$$+\frac{\mu_0 M_f}{4\pi}\int_{-L_I/2}^{L_I/2}\int_0^{2\pi}\frac{r_{Io}\cos(k_I z_I)(z-z_I)}{[r^2+r_{Io}^2-2rr_{Io}\cos(\theta-\theta_I)+(z-z_I)^2]^{3/2}}d\theta_I dz_I \qquad (4.64)$$

$$-\frac{\mu_0 M_f}{4\pi}\int_{-L_I/2}^{L_I/2}\int_0^{2\pi}\frac{r_{Ii}\cos(k_I z_I)(z-z_I)}{[r^2+r_{Ii}^2-2rr_{Ii}\cos(\theta-\theta_I)+(z-z_I)^2]^{3/2}}d\theta_I dz_I$$

By defining:

$$\psi_3(r,\theta,z,r_I,\theta_I,z_I)=\int\frac{(1-k_I r_I)}{[r^2+r_I^2-2rr_I\cos(\theta-\theta_I)+(z-z_I)^2]^{3/2}}dr_I =$$

$$\frac{k_I[r^2+(z-z_I)^2]+r_I[1-k_I r\cos(\theta-\theta_I)]-r\cos(\theta-\theta_I)}{\mathrm{R}(r,\theta,z,r_I,\theta_I,z_I)[r^2-r^2\cos^2(\theta-\theta_I)+(z-z_I)^2]} \qquad (4.65)$$

one can simplify the (4.64) to:

$$B_z^I=\frac{\mu_0 M_f}{4\pi\mu_r}\int_{-L_I/2}^{L_I/2}\int_0^{2\pi}\cos(k_I z_I)(z-z_I)[\psi_3(r,\theta,z,r_{Io},\theta_I,z_I)-\psi_3(r,\theta,z,r_{Ii},\theta_I,z_I)]d\theta_I dz_I$$

$$+\frac{\mu_0 M_f}{4\pi}\int_{-L_I/2}^{L_I/2}\int_0^{2\pi}\frac{r_{Io}\cos(k_I z_I)(z-z_I)}{[r^2+r_{Io}^2-2rr_{Io}\cos(\theta-\theta_I)+(z-z_I)^2]^{3/2}}d\theta_I dz_I \qquad (4.66)$$

$$-\frac{\mu_0 M_f}{4\pi}\int_{-L_I/2}^{L_I/2}\int_0^{2\pi}\frac{r_{Ii}\cos(k_I z_I)(z-z_I)}{[r^2+r_{Ii}^2-2rr_{Ii}\cos(\theta-\theta_I)+(z-z_I)^2]^{3/2}}d\theta_I dz_I$$

### 4.2.2 Force on Linear Coupling

The axial and cross-sectional parameters of the linear coupling are shown in Fig. 4-6. The indices I and II are assigned to the inner and outer translators, respectively. Letters *S* and *V* denote surface and volume.

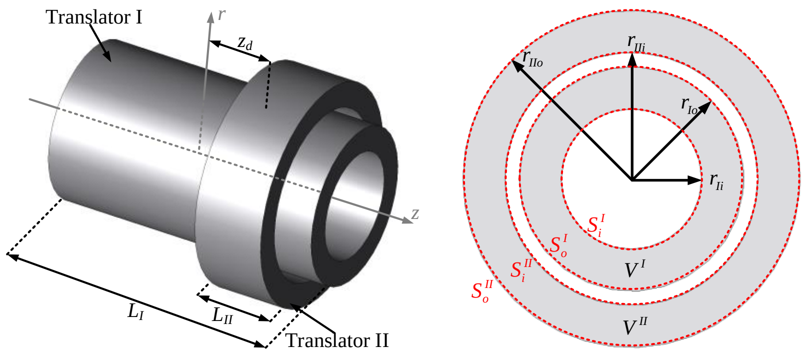


(a) (b)

Fig. 4-6. Linear coupling, a) axial parameters, and b) cross sectional parameters

Four surface and two volume charge functions must be considered for the force calculation. Four force functions can be defined: $F_{SS}(z_d)$, force between two charge cylinders located at $r = r_I$ and $r = r_{II}$; $F_{SV}(z_d)$, force between inner volume and outer charge cylinders; $F_{VS}(z_d)$, force between outer volume and inner charge cylinders; $F_{VV}(z_d)$, force between inner and outer volume charges. The axial shift between two cylinders is defined as $z_d$. The resultant force is the summation of these four components:

$$F(z_d) = F_{SS}(z_d) + F_{SV}(z_d) + F_{VS}(z_d) + F_{VV}(z_d) \tag{4.67}$$

The equation for each of these force functions will be defined in the next four sections.

Charge functions for the inner translator are defined by (4.44)-(4.46), and charge functions for the outer Halbach magnetic cylinder are written as:

$$\rho_m^{II}(z_{II} - z_d) = -\frac{M_f}{r_{II}\mu_r}(1 - k_{II} r_{II})\cos[k_{II}(z_{II} - z_d)] \tag{4.68}$$

$$\sigma_{mi}^{II}(z_{II} - z_d) = -M_f \cos[k_{II}(z_{II} - z_d)] \tag{4.69}$$

$$\sigma_{mo}^{II}(z_{II} - z_d) = M_f \cos[k_{II}(z_{II} - z_d)] \tag{4.70}$$

where:

$$k_{II} = \frac{2\pi p_{II}}{L_{II}} \tag{4.71}$$

where $L_{II}$ and $p_{II}$ are the axial length and the number of pole-pairs of the outer Halbach translator, respectively. In order to create a constant force, the number of pole-pairs within the active length of the coupling must be the same for both inner and outer cylinders. Therefore:

$$k_{II} = k_I = k \tag{4.72}$$

#### 4.2.2.1 General Surface Force Components

The energy between the surface of cylinder I, $S^I$, and the surface of cylinder II, $S^{II}$, can be calculated as [95]:

$$W_{SS}(z_d) = \mu_0 \int_{-L_{II}/2}^{L_{II}/2} \int_0^{2\pi} \phi_S^I(r_{II}, \theta_{II}, z_{II}) \sigma_m^{II}(z_{II} - z_d) r_{II} d\theta_{II} dz_{II} \tag{4.73}$$

The force is computed from:

$$F_{SS}(z_d) = \left. \frac{\partial W_{SS}(z_d)}{\partial z_d} \right|_{\phi_s^I = \text{constant}} \tag{4.74}$$

Substituting (4.73) into (4.74) one can obtain:

$$F_{SS}(z_d) = \mu_0 \int_{-L_{II}/2}^{L_{II}/2} \int_0^{2\pi} \phi_S^I(r_{II}, \theta_{II}, z_{II}) \frac{\partial \sigma_m^{II}(z_{II} - z_d)}{\partial z_d} r_{II} d\theta_{II} dz_{II} \tag{4.75}$$

Considering (4.69) and (4.70) the surface charge density on cylinder II is:

$$\sigma_m^{II}(z_{II} - z_d) = \pm M_f \cos[k(z_{II} - z_d)] \tag{4.76}$$

where positive and negative signs are for the outer and inner surfaces of the cylinder II, respectively.

From (4.52) the magnetic scalar potential field on cylinder II at $(r, \theta, z) = (r_{II}, \theta_{II}, z_{II})$ created by a charge cylinder located at $r_I$ is given by:

$$\phi_S^I(r_{II}, \theta_{II}, z_{II}) = \pm \frac{M_f}{4\pi} \int_{-L_I/2}^{L_I/2} \int_0^{2\pi} \frac{r_I \cos(kz_I) d\theta_I dz_I}{\sqrt{r_{II}^2 + r_I^2 - 2r_{II} r_I \cos(\theta_{II} - \theta_I) + (z_{II} - z_I)^2}} \tag{4.77}$$

Depending on which surface is being considered, $r_I$ is equal to $r_{Ii}$ or $r_{Io}$. Positive and negative signs refer to the outer and inner surfaces of the cylinder I, respectively.

Substituting (4.76) and (4.77) into (4.75) one can obtain:

$$F_{SS}(z_d) = \pm \frac{k\mu_0 M_f^2}{4\pi} \int_{-L_{II}/2}^{L_{II}/2} \int_0^{2\pi} \int_{-L_I/2}^{L_I/2} \int_0^{2\pi} \frac{r_I \cos(kz_I) \sin[k(z_{II} - z_d)]}{\sqrt{r_{II}^2 + r_I^2 - 2r_{II} r_I \cos(\theta_{II} - \theta_I) + (z_{II} - z_I)^2}} r_{II} d\theta_I dz_I d\theta_{II} dz_{II} \tag{4.78}$$

By defining:

$$\theta_a = \theta_{II} - \theta_I \tag{4.79}$$

and noting:

$$d\theta_a = -d\theta_I \tag{4.80}$$

Equation (4.78) becomes:

$$F_{SS}(z_d) = \pm \frac{k\mu_0 M_f^2}{4\pi} \int_{-L_{II}/2}^{L_{II}/2} \int_0^{2\pi} \int_{-L_I/2}^{L_I/2} \int_0^{2\pi} \frac{r_I \cos(kz_I) \sin[k(z_{II} - z_d)]}{\sqrt{r_{II}^2 + r_I^2 - 2r_{II} r_I \cos(\theta_a) + (z_{II} - z_I)^2}} r_{II} d\theta_a dz_I d\theta_{II} dz_{II} \tag{4.81}$$

As the integral is not a function of $\theta_{II}$, (4.81) reduces to:

$$F_{SS}(z_d) = \pm \frac{k\mu_0 M_f^2}{2} \int_{-L_{II}/2}^{L_{II}/2} \int_{-L_I/2}^{L_I/2} \int_0^{2\pi} \frac{r_I r_{II} \cos(kz_I) \sin[k(z_{II} - z_d)]}{\sqrt{r_{II}^2 + r_I^2 - 2r_{II} r_I \cos(\theta_a) + (z_{II} - z_I)^2}} d\theta_a dz_I dz_{II} \tag{4.82}$$

where the negative sign is used when considering ($r_I$, $r_{II}$) = ($r_{Ii}$, $r_{IIo}$) or ($r_I$, $r_{II}$) = ($r_{Io}$, $r_{IIi}$) and the positive sign is used when ($r_I$, $r_{II}$) = ($r_{Ii}$, $r_{IIi}$) or ($r_I$, $r_{II}$) = ($r_{Io}$, $r_{IIo}$) as defined in Fig. 4-6 (b).

#### 4.2.2.2 Surface and Volume Force Components

The energy content of the volume charge region of $V^{II}$ and the surface charge region of $S^I$ is calculated as:

$$W_{SV}(z_d) = \mu_0 \int_{r_{IIi}}^{r_{IIo}} \int_{-L_{II}/2}^{L_{II}/2} \int_{0}^{2\pi} \phi_S^I(r_{II}, \theta_{II}, z_{II}) \rho_m^{II}(z_{II} - z_d) r_{II} d\theta_{II} dz_{II} dr_{II} \tag{4.83}$$

Force is calculated as:

$$F_{SV}(z_d) = \mu_0 \int_{r_{IIi}}^{r_{IIo}} \int_{-L_{II}/2}^{L_{II}/2} \int_{0}^{2\pi} \phi_S^I(r_{II}, \theta_{II}, z_{II}) \frac{\partial \rho_m^{II}(z_{II} - z_d)}{\partial z_d} r_{II} d\theta_{II} dz_{II} dr_{II} \tag{4.84}$$

Substituting (4.52) and (4.68) into (4.84) gives:

$$\begin{aligned} F_{SV}(z_d) = \pm \frac{k\mu_0 M_f^2}{4\pi\mu_r} \int_{r_{IIi}}^{r_{IIo}} \int_{-L_{II}/2}^{L_{II}/2} \int_{0}^{2\pi} \int_{-L_I/2}^{L_I/2} \int_{0}^{2\pi} \\ \frac{\cos(kz_I)\sin[k(z_{II} - z_d)](1 + kr_{II})}{\sqrt{r_{II}^2 + r_I^2 - 2r_{II}r_I \cos(\theta_{II} - \theta_I) + (z_{II} - z_I)^2}} r_I d\theta_I dz_I d\theta_{II} dz_{II} dr_{II} \end{aligned} \tag{4.85}$$

Using definitions (4.79)-(4.80), one obtains:

$$\begin{aligned} F_{SV}(z_d) = \pm \frac{k\mu_0 M_f^2}{4\pi\mu_r} \int_{r_{IIi}}^{r_{IIo}} \int_{-L_{II}/2}^{L_{II}/2} \int_{0}^{2\pi} \int_{-L_I/2}^{L_I/2} \int_{0}^{2\pi} \\ \frac{\cos(kz_I)\sin[k(z_{II} - z_d)](1 + kr_{II})r_I}{\sqrt{r_{II}^2 + r_I^2 - 2r_{II}r_I \cos(\theta_a) + (z_{II} - z_I)^2}} d\theta_a dz_I d\theta_{II} dz_{II} dr_{II} \end{aligned} \tag{4.86}$$

As the integrand is not a function of $\theta_{II}$, (4.86) simplifies to:

$$F_{SV}(z_d) = \pm \frac{k\mu_0 M_f^2}{2\mu_r} \int_{r_{IIi}}^{r_{IIo}} \int_{-L_{II}/2}^{L_{II}/2} \int_{-L_I/2}^{L_I/2} \int_0^{2\pi} \frac{\cos(kz_I)\sin[k(z_{II}-z_d)](1+kr_{II})r_I}{\sqrt{r_{II}^2 + r_I^2 - 2r_{II}r_I\cos(\theta_a) + (z_{II}-z_I)^2}} d\theta_a dz_I dz_{II} dr_{II} \tag{4.87}$$

Using the integral solution:

$$\begin{aligned}\psi_4(r_I, z_I, r_{II}, z_{II}, \theta_a) &= \int \frac{1+kr_{II}}{\sqrt{r_{II}^2 + r_I^2 - 2r_{II}r_I\cos(\theta_a) + (z_{II}-z_I)^2}} dr_{II} = \\ & [1+kr_I\cos(\theta_a)]\,\mathrm{Ln}\left[r_{II} - r_I\cos(\theta_a) + \mathrm{R}(r_I, r_{II}, \theta_a, z_I, z_{II})\right] + k\,\mathrm{R}(r_I, r_{II}, \theta_a, z_I, z_{II})\end{aligned} \tag{4.88}$$

allows (4.87) to be simplified to:

$$\begin{aligned}F_{SV}(z_d) = \pm \frac{k\mu_0 M_f^2}{2\mu_r} \int_{-L_{II}/2}^{L_{II}/2} \int_{-L_I/2}^{L_I/2} \int_0^{2\pi} \cos(kz_I)\sin[k(z_{II}-z_d)] \\ [\psi_4(r_I, z_I, r_{IIo}, z_{II}, \theta_a) - \psi_4(r_I, z_I, r_{IIi}, z_{II}, \theta_a)] r_I d\theta_a dz_I dz_{II}\end{aligned} \tag{4.89}$$

where the negative sign is used when considering $r_I = r_{Io}$ and the positive sign is for $r_I = r_{Ii}$.

Similarly, the energy content of the volume charge region of $V^I$ and surface charge region of $S^{II}$ is calculated as:

$$W_{VS}(z_d) = \mu_0 \int_{-L_{II}/2}^{L_{II}/2} \int_0^{2\pi} \phi_V^I(r_I, r_{II}, \theta_{II}, z_{II}) \sigma_m^{II}(z_{II} - z_d) r_{II} d\theta_{II} dz_{II} \tag{4.90}$$

Then the volume-surface force can be calculated by evaluating:

$$F_{VS}(z_d) = \mu_0 \int_{-L_{II}/2}^{L_{II}/2} \int_0^{2\pi} \phi_V^I(r_I, r_{II}, \theta_{II}, z_{II}) \frac{\partial \sigma_m^{II}}{\partial z_d} r_{II} d\theta_{II} dz_{II} \tag{4.91}$$

Substituting (4.54) and (4.69)-(4.70) into (4.91) gives:

$$F_{VS}(z_d) = \pm \frac{k\mu_0 M_f^2}{4\pi\mu_r} \int_{-L_{II}/2}^{L_{II}/2} \int_0^{2\pi} \int_{-L_I/2}^{L_I/2} \int_0^{2\pi} \int_{r_{Ii}}^{r_{Io}} \frac{\cos(kz_I)\sin[k(z_{II}-z_d)](1-kr_I)r_{II}}{\sqrt{r_{II}^2 + r_I^2 - 2r_{II}r_I\cos(\theta_{II}-\theta_I) + (z_{II}-z_I)^2}} dr_I d\theta_I dz_I d\theta_{II} dz_{II} \tag{4.92}$$

Using definitions (4.79)-(4.80), one can obtain:

$$F_{VS}(z_d) = \pm \frac{k\mu_0 M_f^2}{4\pi\mu_r} \int_{-L_{II}/2}^{L_{II}/2} \int_0^{2\pi} \int_{-L_I/2}^{L_I/2} \int_0^{2\pi} \int_{r_{Ii}}^{r_{Io}} \frac{\cos(kz_I)\sin[k(z_{II}-z_d)](1-kr_I)r_{II}}{\sqrt{r_{II}^2 + r_I^2 - 2r_{II}r_I\cos(\theta_a) + (z_{II}-z_I)^2}} dr_I d\theta_a dz_I d\theta_{II} dz_{II} \tag{4.93}$$

As the integrand is not a function of $\theta_{II}$, (4.93) simplifies to:

$$F_{VS}(z_d) = \pm \frac{k\mu_0 M_f^2}{2\mu_r} \int_{-L_{II}/2}^{L_{II}/2} \int_{-L_I/2}^{L_I/2} \int_0^{2\pi} \int_{r_{Ii}}^{r_{Io}} \frac{\cos(kz_I)\sin[k(z_{II}-z_d)](1-kr_I)r_{II}}{\sqrt{r_{II}^2 + r_I^2 - 2r_{II}r_I\cos(\theta_a) + (z_{II}-z_I)^2}} dr_I d\theta_a dz_I dz_{II} \tag{4.94}$$

by defining:

$$\psi_5(r_I, z_I, r_{II}, z_{II}, \theta_a) = \int \frac{(1-kr_I)}{\sqrt{r_{II}^2 + r_I^2 - 2r_{II}r_I\cos(\theta_a) + (z_{II}-z_I)^2}} dr_I = \\ [1-kr_{II}\cos(\theta_a)]\,\mathrm{Ln}[r_I - r_{II}\cos(\theta_a) + \mathrm{R}(r_I, r_{II}, \theta_a, z_I, z_{II})] - k\,\mathrm{R}(r_I, r_{II}, \theta_a, z_I, z_{II}) \tag{4.95}$$

Simplifies (4.94) to:

$$F_{VS}(z_d) = \pm \frac{k\mu_0 M_f^2}{2\mu_r} \int_{-L_{II}/2}^{L_{II}/2} \int_{-L_I/2}^{L_I/2} \int_0^{2\pi} \cos(kz_I)\sin[k(z_{II}-z_d)] [\psi_5(r_{Io}, z_I, r_{II}, z_{II}, \theta_a) - \psi_5(r_{Ii}, z_I, r_{II}, z_{II}, \theta_a)] r_{II} d\theta_a dz_I dz_{II} \tag{4.96}$$

where the negative sign is used when considering $S_o^{II}$ and the positive sign is for $S_i^{II}$.

#### 4.2.2.3 Volume Force Components

Energy content of the volume charge regions of $V^I$ and $V^{II}$ is calculated as:

$$W_{VV}(z_d)=\mu_0\int_{r_{IIi}}^{r_{IIo}}\int_{-L_{II}/2}^{L_{II}/2}\int_{0}^{2\pi}\phi_V^I(r_{II},\theta_{II},z_{II})\rho_m^{II}(z_{II}-z_d)r_{II}d\theta_{II}dz_{II}dr_{II} \tag{4.97}$$

Force is calculated as:

$$F_{VV}(z_d)=\mu_0\int_{r_{IIi}}^{r_{IIo}}\int_{-L_{II}/2}^{L_{II}/2}\int_{0}^{2\pi}\phi_V^I(r_{II},\theta_{II},z_{II})\frac{\partial\rho_m^{II}}{\partial z_d}r_{II}d\theta_{II}dz_{II}dr_{II} \tag{4.98}$$

Substituting (4.54) and (4.68) into (4.98) gives:

$$\begin{aligned}F_{VV}(z_d)=\frac{k\mu_0M_f^2}{4\pi\mu_r^2}\int_{r_{IIi}}^{r_{IIo}}\int_{-L_{II}/2}^{L_{II}/2}\int_{0}^{2\pi}\int_{0}^{2\pi}\int_{-L_I/2}^{L_I/2}\int_{r_{Ii}}^{r_{Io}}\cos(kz_I)\sin[k(z_{II}-z_d)]\\ \frac{(1+kr_{II})(1-kr_I)dr_Idz_Id\theta_Id\theta_{II}dz_{II}dr_{II}}{\sqrt{r_{II}^2+r_I^2-2r_{II}r_I\cos(\theta_{II}-\theta_I)+(z_{II}-z_I)^2}}\end{aligned} \tag{4.99}$$

Changing the angular variables based on (4.79)-(4.80) enables (4.99) to become:

$$\begin{aligned}F_{VV}(z_d)=\frac{k\mu_0M_f^2}{4\pi\mu_r^2}\int_{r_{IIi}}^{r_{IIo}}\int_{-L_{II}/2}^{L_{II}/2}\int_{0}^{2\pi}\int_{0}^{2\pi}\int_{-L_I/2}^{L_I/2}\int_{r_{Ii}}^{r_{Io}}\cos(kz_I)\sin[k(z_{II}-z_d)]\\ \frac{(1+kr_{II})(1-kr_I)dr_Idz_Id\theta_ad\theta_{II}dz_{II}dr_{II}}{\sqrt{r_{II}^2+r_I^2-2r_{II}r_I\cos(\theta_a)+(z_{II}-z_I)^2}}\end{aligned} \tag{4.100}$$

As the integrand is not a function of $\theta_{II}$, (4.100) reduces to:

$$\begin{aligned}F_{VV}(z_d)=\frac{k\mu_0M_f^2}{2\mu_r^2}\int_{r_{IIi}}^{r_{IIo}}\int_{-L_{II}/2}^{L_{II}/2}\int_{-L_I/2}^{L_I/2}\int_{0}^{2\pi}\int_{r_{Ii}}^{r_{Io}}\cos(kz_I)\sin[k(z_{II}-z_d)]\\ \frac{(1+kr_{II})(1-kr_I)dr_Id\theta_adz_Idz_{II}dr_{II}}{\sqrt{r_{II}^2+r_I^2-2r_{II}r_I\cos(\theta_a)+(z_{II}-z_I)^2}}\end{aligned} \tag{4.101}$$

Using the definition (4.95), (4.101) becomes:

$$\begin{aligned}F_{VV}(z_d)=\frac{k\mu_0M_f^2}{2\mu_r^2}\int_{r_{IIi}}^{r_{IIo}}\int_{-L_{II}/2}^{L_{II}/2}\int_{-L_I/2}^{L_I/2}\int_{0}^{2\pi}\cos(kz_I)\sin[k(z_{II}-z_d)]\\ [\psi_5(r_{Io},r_{II})-\psi_5(r_{Ii},r_{II})](1+kr_{II})d\theta_adz_Idz_{II}dr_{II}\end{aligned} \tag{4.102}$$

The quadruple integral was evaluated using Matlab function integralN.

Substituting (4.82), (4.89), (4.96), (4.102) into (4.67), the complete force equation is:

$$
\begin{aligned}
F(z_d) = \pm \frac{k\mu_0 M_f^2}{2} \int_{-L_{II}/2}^{L_{II}/2} \int_{-L_I/2}^{L_I/2} \int_{0}^{2\pi} \cos(kz_I)\sin[k(z_{II}-z_d)] \cdot \{ \\
\frac{r_I r_{II}}{\sqrt{r_{II}^2 + r_I^2 - 2r_{II} r_I \cos(\theta_a) + (z_{II}-z_I)^2}} \\
+[\psi_4(r_I, z_I, r_{IIo}, z_{II}, \theta_a) - \psi_4(r_I, z_I, r_{IIi}, z_{II}, \theta_a)] r_I \\
+[\psi_5(r_{Io}, z_I, r_{II}, z_{II}, \theta_a) - \psi_5(r_{Ii}, z_I, r_{II}, z_{II}, \theta_a)] r_{II} \} d\theta_a dz_I dz_{II} \\
+ \frac{k\mu_0 M_f^2}{2\mu_r^2} \int_{r_{IIi}}^{r_{IIo}} \int_{-L_{II}/2}^{L_{II}/2} \int_{-L_I/2}^{L_I/2} \int_{0}^{2\pi} \cos(kz_I)\sin[k(z_{II}-z_d)] \\
[\psi_5(r_{Io}, r_{II}) - \psi_5(r_{Ii}, r_{II})](1+kr_{II}) d\theta_a dz_I dz_{II} dr_{II}
\end{aligned}
\tag{4.103}
$$

Force is maximum when:

$$
kz_d = \frac{\pi}{2} \tag{4.104}
$$

substituting (4.71) into (4.104) gives

$$
z_d = \frac{L_{II}}{4p_{II}} \tag{4.105}
$$

### 4.2.3 Validation Using Finite Element Analysis

In order to verify the analytic results, a 3D FEA model of a Halbach LPMC was considered. Fig. 4-7 shows the geometry of this linear coupling and the corresponding mesh plot. Total number of about 1.3 million mesh element was generated for this model. A summary of the design parameters is given in Table 4-I, which has been chosen to match the analytic model. Both translators have the same number of pole-pairs in the active length, but the inner translator has twice the length of the outer cylinder.

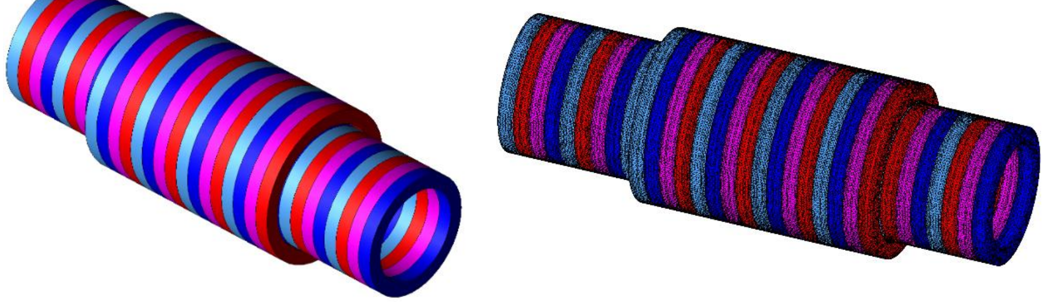

(a) (b)

Fig. 4-7. a) 3D FEA model of a Halbach linear coupling b) the mesh.

Table 4-I. Summary of geometric and material parameters

| Parameter | | Value | Unit |
|---|---|---|---|
| Inner translator | Inner radius, $r_{Ii}$ | 10 | mm |
| | Outer radius, $r_{Io}$ | 13 | mm |
| | Axial length, $L_I$ | 96 | mm |
| | Number of pole-pairs, $p_I$ | 8 | - |
| | Airgap length, $g$ | 0.4 | mm |
| Outer translator | Inner radius, $r_{IIi}$ | 13.4 | mm |
| | Outer radius, $r_{IIo}$ | 16.4 | mm |
| | Axial length, $L_{II}$ | 48 | mm |
| | Number of pole-pairs, $p_{II}$ | 4 | - |
| Material | NdFeB magnet, $B_r$, NMX-40CH | 1.25 | T |

The calculated radial and axial flux densities over a line above the surface of the inner translator, while surrounded by air, is shown in Fig. 4-8. This figure shows a comparison between the analytic method and FEA. The percentage of error is about 1.5 percent at peak. The calculated force using FEA and analytical model is compared in Fig. 4-9, which shows a perfect match at peak.

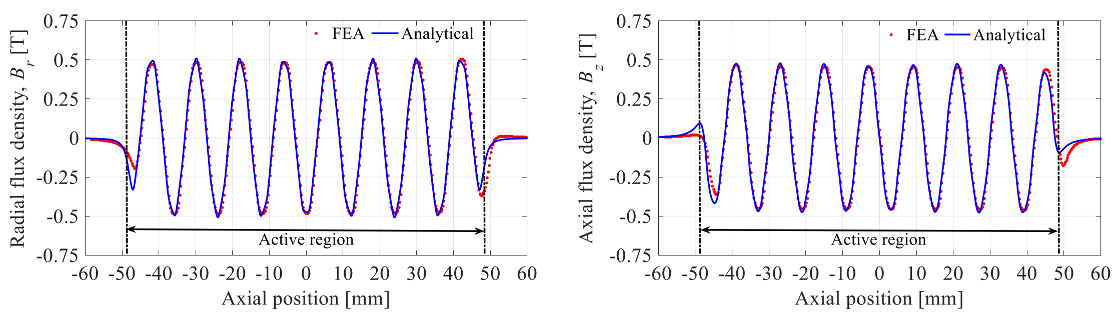


(a) (b)

Fig. 4-8. FEA and analytically calculated magnetic flux density a) radial b) axial

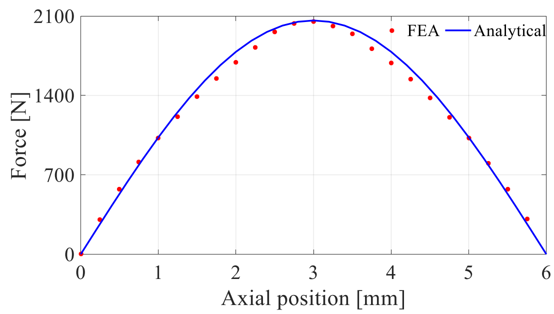

Fig. 4-9. FEA and analytically calculated force

### 4.2.4 Parameter Analysis

In order to understand the effect of different geometric parameters on the performance of the LPMC, a parametric sweep analysis was performed in this section. The geometric parameters are defined as shown in Fig. 4-10. The pole-pitch, $\tau_p$, between the inner and outer translators were kept equal. Three scaling-ratios are considered for a given $r_{IIo}$:

$$\Gamma_{oo} = \frac{r_{Io}}{r_{IIo}} \tag{4.106}$$

$$\Gamma_{io} = \frac{r_{Ii}}{r_{Io}} \tag{4.107}$$

$$\Gamma_{po} = \frac{\tau_p}{r_{IIo}} \tag{4.108}$$

where $\tau_p$ is the pole-pitch of the Halbach array as defined in Fig. 4-10.

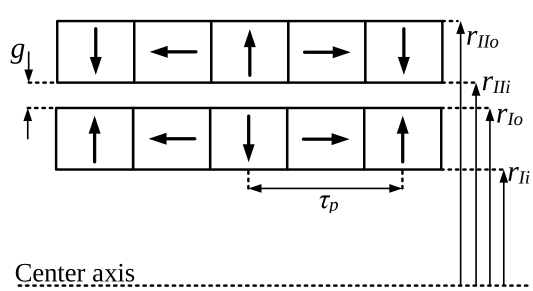

Fig. 4-10. A 2D cut-view of a Halbach cylinder

The parametric analysis in this section is based on the approach presented in [25]. The ratio of $\tau_p/r_{IIo}$ was fixed at arbitrary value of 0.3 and the volumetric and mass force densities as a function of $r_{Ii}/r_{Io}$ and $r_{Io}/r_{IIo}$ were calculated. The outer cylinder radius and airgap length were also fixed at $r_{IIo}$ = 30 mm and $g$ = 1 mm, respectively. Fig. 4-11 shows the results of this parametric sweep. The volumetric and mass force densities are defined as:

$$FV = \frac{F}{\pi r_{IIo}^2 L_{II}} \quad \text{[kN/L]} \tag{4.109}$$

$$FM = \frac{F}{\pi (r_{IIo}^2 - r_{IIi}^2 + r_{Io}^2 - r_{Ii}^2) L_{II} D} \quad \text{[kN/kg]} \tag{4.110}$$

where $D$ is the mass density of the magnet materials.

Fig. 4-11(a) shows that the maximum volumetric force density of 32.03 kN/L occurs at $(\Gamma_{oo}, \Gamma_{io})$ = (0.75, 0.2), and Fig. 4-11(b) shows that the maximum mass force density of 6.62 kN/kg is achieved at $(\Gamma_{oo}, \Gamma_{io})$ = (0.85, 0.83).

A similar analyses were performed for different values of $r_{IIo}$. Table 4-II shows the values of geometric ratios (4.106)-(4.107) at maximum mass force density for different values of $r_{IIo}$. Studying this table shows that the maximum mass force density occurs when:

$$r_{Io} \simeq \frac{r_{Ii} + r_{IIo}}{2} \tag{4.111}$$

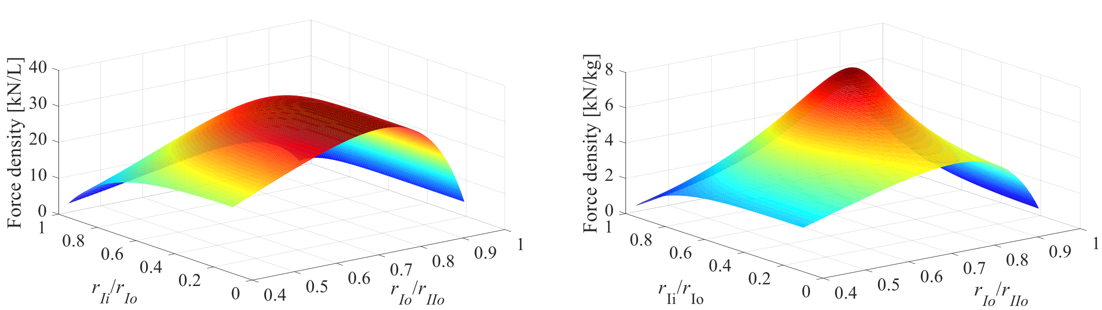


(a) (b)

Fig. 4-11. a) Volumetric force density, and b) mass force density as a function of $r_{Ii}/r_{Io}$ and $r_{Io}/r_{IIo}$, when $r_{IIo}$ = 30 mm and $\tau_p/r_{IIo}$ = 0.3.

Table 4-II. Summary of the ratios value for different values of $r_{IIo}$, while $\tau_p/r_{IIo}$ = 0.3.

| $r_{IIo}$ [mm] | $r_{Io}$ [mm] | $r_{Ii}$ [mm] | $(r_{Ii} + r_{IIo})/2$ [mm] | $\Gamma_{oo}$ | $\Gamma_{io}$ | FM [kN/kg] | FV [kN/L] |
|---|---|---|---|---|---|---|---|
| 30 | 25.5 | 21.16 | 25.58 | 0.85 | 0.83 | 6.62 | 32.03 |
| 40 | 34.4 | 28.89 | 34.44 | 0.86 | 0.84 | 2.71 | 13.18 |
| 50 | 43 | 36.12 | 43.06 | 0.86 | 0.84 | 2.85 | 13.94 |
| 60 | 52.2 | 44.37 | 52.18 | 0.87 | 0.85 | 3.94 | 19.29 |
| 70 | 60.9 | 51.76 | 60.88 | 0.87 | 0.85 | 3.46 | 16.98 |
| 80 | 69.6 | 59.16 | 69.58 | 0.87 | 0.85 | 3.08 | 15.15 |
| 90 | 78.3 | 65.55 | 78.27 | 0.87 | 0.85 | 2.78 | 13.68 |
| 100 | 87 | 73.95 | 86.97 | 0.87 | 0.85 | 2.53 | 12.46 |

The maximum volumetric force density when $r_{IIo}$ = 30 mm happens at $r_{Ii}/r_{Io}$ = 0.2. This value corresponds to a design with a high magnet mass and consequently low mass force density results. Mass force density for different designs within this parametric analysis space is plotted against the volumetric force density in Fig. 4-12. This figure shows that in order to select a good design, one should make a compromise between cost and performance. Therefore, a ratio of $r_{Ii}/r_{Io}$ = 0.7 was selected to achieve a design with a relatively high volumetric and mass force density. Volumetric and mass force densities as a function of $r_{Ii}/r_{Io}$ for three different values of $r_{Io}/r_{IIo}$ are shown in Fig. 4-13 for the case when $r_{IIo}$ = 30 mm. As can be seen the volumetric force density curves are almost parallel to each other, which implies that the ratio of $r_{Io}/r_{IIo}$ is independent of the other two parameters [25]. Therefore, $r_{Ii}/r_{Io}$ = 0.7 was selected for the next step of the parametric analysis.

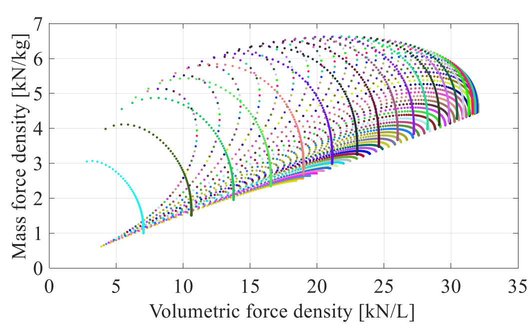


Fig. 4-12. Volumetric force density versus mass force density for different configurations within the design space, when $r_{IIo}$ = 30 mm and $\tau_p/r_{IIo}$ = 0.3.

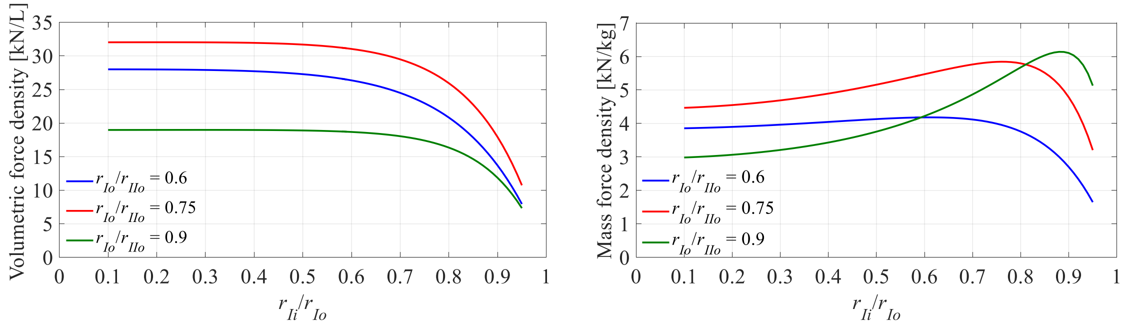


(a) (b)

Fig. 4-13. a) Volumetric and b) Mass force density as a function of $r_{Ii}/r_{Io}$ for three different value of $r_{Io}/r_{IIo}$, when $r_{IIo}$ = 30 mm and $\tau_p/r_{IIo}$ = 0.3.

By choosing $r_{Ii}/r_{Io}$ = 0.7, and using all other parameters the same as the initial values of the first step of the parametric analysis, the volumetric force density and mass force density as function of $\tau_p/r_{IIo}$ and $r_{Io}/r_{IIo}$ are plotted in Fig. 4-14. There is an optimal combination of ratios that results in a maximum force density, $(\Gamma_{oo}, \Gamma_{po})$ = (0.78, 0.24). The maximum force density is 30.33 kN/L. The corresponding mass force density for this design is 6.15 kN/kg. This shows that using this approach a design with relatively good volumetric force density is achieved while the mass force density is also maintained.

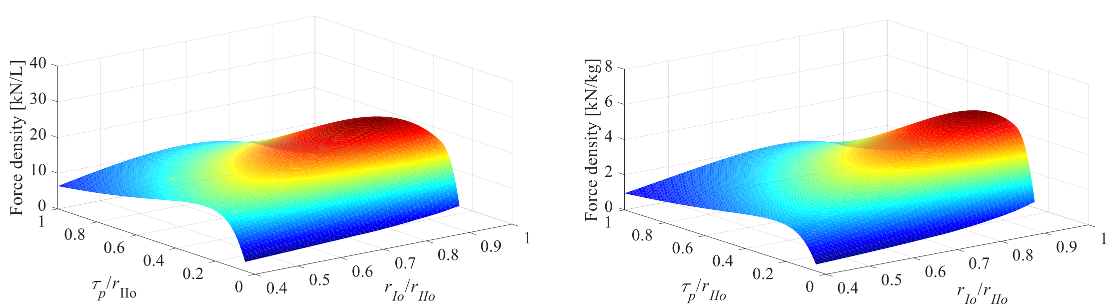


(a) (b)

Fig. 4-14. a) Volumetric force density, and b) mass force density as a function of $\tau_p/r_{IIo}$ and $r_{Io}/r_{IIo}$, when $r_{IIo}$ = 30 mm and $r_{Ii}/r_{Io}$ = 0.7.

The mass force densities as a function of $\tau_p$ and $r_{Ii}$ when relationship (4.111) was satisfied for two different values of $r_{IIo}$ are shown in Fig. 4-15. A maximum mass force density of 9.3 kN/kg was achieved for design with $r_{IIo}$ = 30 mm. The corresponding parameter values were $(\tau_p, r_{Ii})$ = (4 mm, 25 mm). The value of these parameter at maximum mass force density when $r_{IIo}$ = 100 mm are ($\tau_p$, $r_{Ii}$) = (4 mm, 95 mm). The maximum mass force density is almost the same.

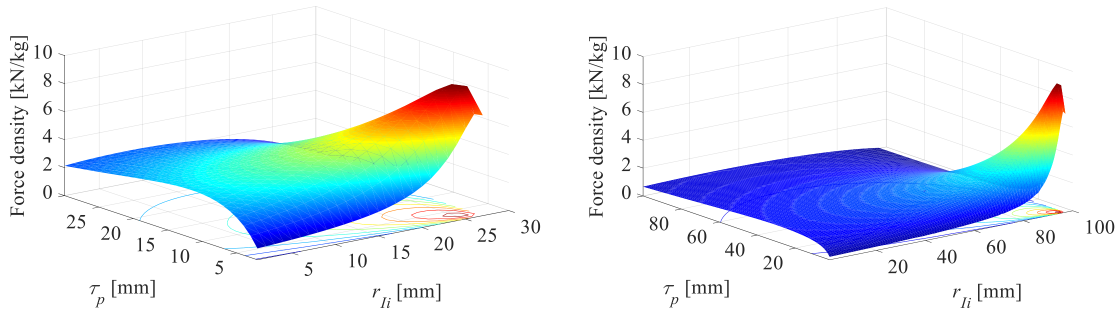


(a) (b)

Fig. 4-15. Mass force density while geometric parameters satisfy (4.111) for a) $r_{IIo}$ = 30 mm and b) $r_{IIo}$ = 100.

Plot of maximum mass force densities as a function of $\tau_p$ and $r_{IIo}$ is shown in Fig. 4-16. As can be seen, 9.3 kN/kg is the maximum achievable mass force density for different values of the $r_{IIo}$. Mass force densities as a function of $r_{Ii}$ for different values of the $r_{IIo}$ is shown in Fig. 4-17.

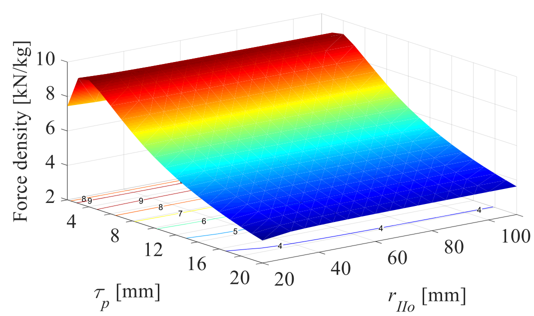


Fig. 4-16. Maximum mass force density for different values of $r_{IIo}$.

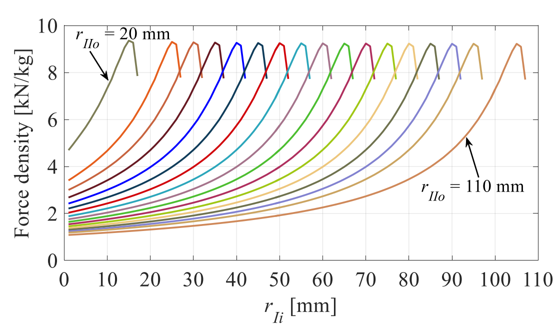


Fig. 4-17. Maximum mass force density for different values of $r_{IIo}$ as a function of $r_{Ii}$.

## 4.3 Analytical Based Model for a Halbach Magnetic Lead Screw

The principle of operation of the MLS was explain in section 4.2. Understanding the scaling and geometric limits of the MLS can provide information on the upper torque/force density limit for non-superconducting linear-to-rotary magnetic devices.

The design of the MLS is challenging because a full 3D finite element analysis model is needed in order to account for both the simultaneous linear-to-rotary motion. If the translator length is long, then the simulation model becomes excessively large and this makes conducting geometric parameter analysis particularly time-consuming. The reliance on 2D and 3D FEA to conduct the MLS sizing analysis has been used by a number of authors, for instance [47], [51], [53], but only a limited design space was simulated using FEA. Wang *et al.* [46] Pakdelian *et al.* [59] and Ling *et al.* [97] have relied on a 2D current sheet analytic model of the MLS to help with the design analysis. However, the 2D current sheet approach neglects the axial edge effects and also neglects the relative permeability within the magnet material. An axial edge effect correction factor can be used to minimize the 2D modelling error [85], however the approach is still approximate. The analytical-based model explained in section 4.2 is built upon in order to develope the 3D MLS analytical model.

A 2D sketch of one period of a Halbach array for a MLS is shown in Fig. 4-18. The magnetization vector form for MLS has the same component basis as the linear coupling. The magnetization components are depicted in Fig. 4-19. The only difference is that these components displaced along the $z$ direction as the angular position, $\theta$, changes.

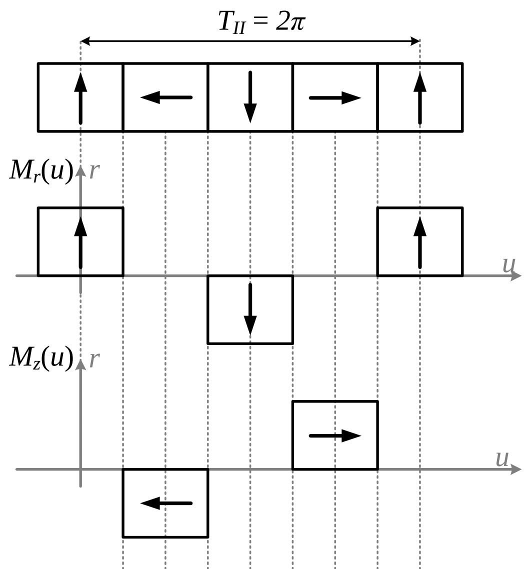


Fig. 4-18. One period of the Halbach array

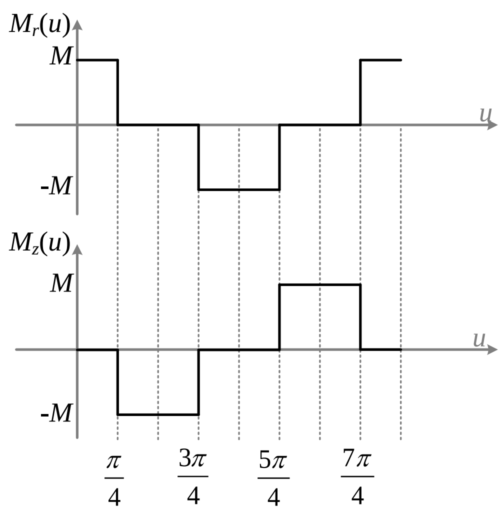


Fig. 4-19. Magnetization plots of the Halbach array

The vector representation of this Halbach array is:

$$\mathrm{M} = M_r(z_I, \theta_I)\hat{\mathrm{r}} + M_z(z_I, \theta_I)\hat{\mathrm{z}} \tag{4.112}$$

and its corresponding Fourier series is:

$$\mathbf{M} = \sum_{n=1}^{\infty} a_n \cos[n(k_I z_I + \theta_I)]\, \hat{\mathbf{r}} + \sum_{n=1}^{\infty} b_n \sin[n(k_I z_I + \theta_I)]\, \hat{\mathbf{z}} \tag{4.113}$$

By defining:

$$u = k_I z_I + \theta_I \tag{4.114}$$

The Fourier series coeficients of (4.113) are:

$$a_n = \frac{4}{T_m} \int_0^{T_m/2} M_r(u)\cos(nu)du \tag{4.115}$$

$$b_n = \frac{4}{T_m} \int_0^{T_m/2} M_z(u)\sin(nu)du \tag{4.116}$$

where $T_m$ is the Halbach array period and defined as:

$$T_m = 2\pi \tag{4.117}$$

Comparing equations (4.115) and (4.116) with (4.3) and (4.4), the Fourier series coefficients for different angular position along the *z* axis will be the same. This is intuitive, because the magnetization plots for different angular positions have the same shape and are only shifted along the *z* direction. Noting the step change magnetizing values in Fig. 4-19 and using half-wave symmetry, (4.115) and (4.116) become:

$$a_n = \frac{4}{2\pi} \int_0^{\pi} M\cos(nu)du \tag{4.118}$$

$$a_n = \frac{2M}{n\pi}[\sin(nu)\big|_0^{\pi/4} - \sin(nu)\big|_{3\pi/4}^{\pi}] = \frac{2M}{n\pi}[\sin(\frac{n\pi}{4}) - \sin(n\pi) + \sin(\frac{3n\pi}{4})] \tag{4.119}$$

Using the trigonometric identity of (4.9) equation (4.119) becomes:

$$a_n = \frac{2M}{n\pi}[2\sin(\frac{n\pi}{2})\cos(\frac{n\pi}{4})] \tag{4.120}$$

or

$$a_n = \begin{cases} \dfrac{4M}{n\pi}[\sin(\dfrac{n\pi}{2})\cos(\dfrac{n\pi}{4})] & , n \text{ odd} \\ 0 & , n \text{ even} \end{cases} \tag{4.121}$$

and

$$b_n = \frac{-4}{2\pi}[\int_{\pi/4}^{3\pi/4} M\sin(nu)du] \tag{4.122}$$

$$b_n = \frac{2M}{n\pi}[\cos(nu)|_{\pi/4}^{3\pi/4}] = \frac{2M}{n\pi}[\cos(\frac{3n\pi}{4}) - \cos(\frac{n\pi}{4})] \tag{4.123}$$

Using the trigonometric identity (4.13) equation (4.123) becomes:

$$b_n = \frac{-2M}{n\pi}[2\sin(\frac{n\pi}{2})\sin(\frac{n\pi}{4})] \tag{4.124}$$

or

$$b_n = \begin{cases} -\dfrac{4M}{n\pi}[\sin(\dfrac{n\pi}{2})\sin(\dfrac{n\pi}{4})] & , n \text{ odd} \\ 0 & , n \text{ even} \end{cases} \tag{4.125}$$

Note equations (4.121) and (4.125) have the same form as (4.11) and (4.15). Substituting (4.121) and (4.125) into (4.113) gives:

$$\begin{aligned} \mathbf{M} = & \frac{4M}{\pi}\sum_{n=1}^{\infty}\frac{1}{2n-1}\sin[\frac{(2n-1)\pi}{4}]\cos[(2n-1)(k_I z_I + \theta_I)]\,\hat{\mathbf{r}} \\ & -\frac{4M}{\pi}\sum_{n=1}^{\infty}\frac{1}{2n-1}\cos[\frac{(2n-1)\pi}{4}]\sin[(2n-1)(k_I z_I + \theta_I)]\,\hat{\mathbf{z}} \end{aligned} \tag{4.126}$$

For the first harmonic ($n$ = 1), from (4.121) and (4.125) one can obtain:

$$|a_1| = |b_1| = 0.9003M \tag{4.127}$$

which is the same value as the linear coupling in (4.18).

The geometry of the inner part of the Halbach MLS in cylindrical coordinate system is shown in Fig. 4-20. Cylindrical surfaces $S_o^I$ and $S_i^I$ are located at $r$ = $r_{Io}$ and $r$ = $r_{Ii}$ respectively, and a volume $V^I$ is defined in between these two surfaces.

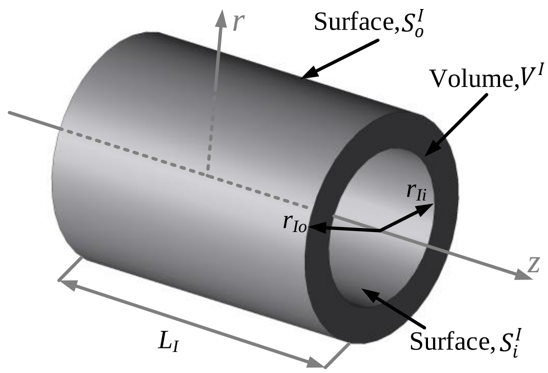


Fig. 4-20. Geometry definition for inner part of the MLS

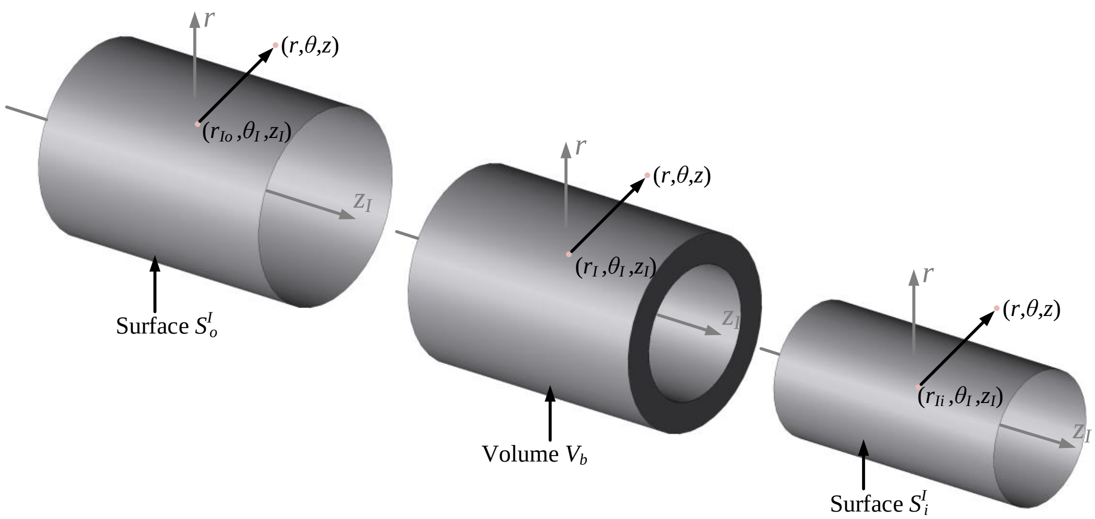


Fig. 4-21. Point charge and related coordinate parameters

A point charge is defined as shown in Fig. 4-21. In order to calculate the magnetic field of this Halbach cylinder at an arbitrary point of ($r$, $\theta$, $z$), two surface charge densities of $\sigma_{mo}^I$ and $\sigma_{mi}^I$ and one volume charge density of $\rho_m^I$ are defined for surface $S_o^I$, surface $S_i^I$ and volume $V^I$, respectively. Volume and surface charges are defined as follow:

$$\rho_m^I(z_I,\theta_I) = -\frac{\nabla\cdot\mathbf{M}}{\mu_r}, \text{ in volume } V^I \tag{4.128}$$

$$\sigma_{mo}^{I}(z_I,\theta_I) = +\hat{\boldsymbol{r}}\cdot\mathbf{M}, \text{ on surface } S_o^I \tag{4.129}$$

$$\sigma_{mi}^{I}(z_I,\theta_I) = -\hat{\boldsymbol{r}}\cdot\mathbf{M}, \text{ on surface } S_i^I \tag{4.130}$$

where using (4.38) one can obtain:

$$\nabla\cdot\mathbf{M} = \frac{1}{r_I}\sum_{n=1}^{\infty} a_n \cos[n(k_I z_I + \theta_I)] + k_I \sum_{n=1}^{\infty} n b_n \cos[n(k_I z_I + \theta_I)] \tag{4.131}$$

or

$$\nabla\cdot\mathbf{M} = \sum_{n=1}^{\infty}(\frac{1}{r_I}a_n + k_I n b_n)\cos[n(k_I z_I + \theta_I)] \tag{4.132}$$

Therefore (4.132) into (4.128) gives:

$$\rho_m^I(z_I,\theta_I) = -\sum_{n=1}^{\infty}(\frac{1}{\mu_r r_I}a_n + \frac{k_I}{\mu_r} n b_n)\cos[n(k_I z_I + \theta_I)] \tag{4.133}$$

and (4.113) into (4.129) and (4.130) gives:

$$\sigma_{mo}^{I}(z_I,\theta_I) = \sum_{n=1}^{\infty} a_n \cos[n(k_I z_I + \theta_I)], \text{ on surface } S_o^I \tag{4.134}$$

$$\sigma_{mi}^{I}(z_I,\theta_I) = -\sum_{n=1}^{\infty} a_n \cos[n(k_I z_I + \theta_I)], \text{ on surface } S_i^I \tag{4.135}$$

Considering just the fundamental component (4.133) to (4.135) become:

$$\rho_m^I(z_I,\theta_I) = -(\frac{1}{\mu_r r_I} - \frac{k_I}{\mu_r})M_f \cos(k_I z_I + \theta_I) \tag{4.136}$$

$$\sigma_{mo}^{I}(z_I,\theta_I) = M_f \cos(k_I z_I + \theta_I) \tag{4.137}$$

$$\sigma_{mi}^{I}(z_I,\theta_I) = -M_f \cos(k_I z_I + \theta_I) \tag{4.138}$$

where $M_f$ is the fundamental magnitude of magnetization defined by (4.19)

The magnetic scalar potential at an arbitrary point is defined as follow:

$$\phi^I(r,\theta,z) = \frac{1}{4\pi}\int_0^{2\pi}\int_{-L_I/2}^{L_I/2}\int_{r_{Ii}}^{r_{Io}} \frac{\rho_m^I(z_I,\theta_I)}{\mathrm{R}(r,\theta,z,r_I,\theta_I,z_I)} r_I dr_I d\theta_I dz_I + \frac{1}{4\pi}\int_{-L_I/2}^{L_I/2}\int_0^{2\pi} \frac{\sigma_{mo}^I(z_I,\theta_I)}{\mathrm{R}(r,\theta,z,r_{Io},\theta_I,z_I)} r_{Io} d\theta_I dz_I + \frac{1}{4\pi}\int_{-L_I/2}^{L_I/2}\int_0^{2\pi} \frac{\sigma_{mi}^I(z_I,\theta_I)}{\mathrm{R}(r,\theta,z,r_{Ii},\theta_I,z_I)} r_{Ii} d\theta_I dz_I \quad (4.139)$$

Substituting (4.136)-(4.138) into (4.139) gives:

$$\phi^I(r,\theta,z) = \frac{M_f}{4\pi}\int_{-L_I/2}^{L_I/2}\int_0^{2\pi} \frac{\cos(k_I z_I+\theta_I)}{\mathrm{R}(r,\theta,z,r_{Io},\theta_I,z_I)} r_{Io} d\theta_I dz_I - \frac{M_f}{4\pi}\int_{-L_I/2}^{L_I/2}\int_0^{2\pi} \frac{\cos(k_I z_I+\theta_I)}{\mathrm{R}(r,\theta,z,r_{Ii},\theta_I,z_I)} r_{Ii} d\theta_I dz_I - \frac{M_f}{4\pi\mu_r}\int_{-L_I/2}^{L_I/2}\int_0^{2\pi}\int_{r_{Ii}}^{r_{Io}} \frac{\cos(k_I z_I+\theta_I)}{\mathrm{R}(r,\theta,z,r_I,\theta_I,z_I)} (1-k_I r_I) dr_I d\theta_I dz_I \quad (4.140)$$

which is the same as (4.47) except the charges are dependent on $z_I$ and $\theta_I$.

Based on the (4.48) magnetic scalar potential can be separated into three terms for surfaces $S_o^I$ and $S_i^I$ and volume $V^I$ as follow:

$$\phi^I(r,\theta,z) = \phi_{So}^I(r,\theta,z) + \phi_{Si}^I(r,\theta,z) + \phi_V^I(r,\theta,z) \quad (4.141)$$

where

$$\phi_{So}^I(r,\theta,z) = \frac{M_f}{4\pi}\int_{-L_I/2}^{L_I/2}\int_0^{2\pi} \frac{\cos(k_I z_I+\theta_I)}{\mathrm{R}(r,\theta,z,r_{Io},\theta_I,z_I)} r_{Io} d\theta_I dz_I \quad (4.142)$$

$$\phi_{Si}^I(r,\theta,z) = -\frac{M_f}{4\pi}\int_{-L_I/2}^{L_I/2}\int_0^{2\pi} \frac{\cos(k_I z_I+\theta_I)}{\mathrm{R}(r,\theta,z,r_{Ii},\theta_I,z_I)} r_{Ii} d\theta_I dz_I \quad (4.143)$$

$$\phi_V^I(r,\theta,z) = -\frac{M_f}{4\pi\mu_r}\int_0^{2\pi}\int_{-L_I/2}^{L_I/2}\int_{r_{Ii}}^{r_{Io}} \frac{\cos(k_I z_I + \theta_I)}{\mathrm{R}(r,\theta,z,r_I,\theta_I,z_I)}(1-k_I r_I)\,dr_I\,d\theta_I\,dz_I \tag{4.144}$$

Replacing the R function in (4.142)-(4.144) gives:

$$\phi_{So}^I(r,\theta,z) = \frac{M_f}{4\pi}\int_{-L_I/2}^{L_I/2}\int_0^{2\pi} \frac{r_{Io}\cos(k_I z_I + \theta_I)}{\sqrt{r^2 + r_{Io}^2 - 2rr_{Io}\cos(\theta-\theta_I) + (z-z_I)^2}}\,d\theta_I\,dz_I \tag{4.145}$$

$$\phi_{Si}^I(r,\theta,z) = -\frac{M_f}{4\pi}\int_{-L_I/2}^{L_I/2}\int_0^{2\pi} \frac{r_{Ii}\cos(k_I z_I + \theta_I)}{\sqrt{r^2 + r_{Ii}^2 - 2rr_{Ii}\cos(\theta-\theta_I) + (z-z_I)^2}}\,d\theta_I\,dz_I \tag{4.146}$$

$$\phi_V^I(r,\theta,z) = -\frac{M_f}{4\pi\mu_r}\int_0^{2\pi}\int_{-L_I/2}^{L_I/2}\int_{r_{Ii}}^{r_{Io}} \frac{\cos(k_I z_I + \theta_I)(1-k_I r_I)}{\sqrt{r^2 + r_I^2 - 2rr_I\cos(\theta-\theta_I) + (z-z_I)^2}}\,dr_I\,d\theta_I\,dz_I \tag{4.147}$$

### 4.3.1 Magnetic Flux Density for the Magnetic Lead Screw

Magnetic flux density can be determined by substituting (4.139) into (4.28) this gives:

$$\begin{aligned}\mathbf{B}^I(r,\theta,z) = \frac{\mu_0}{4\pi}\{&\iiint_v \frac{\rho_m^I(z_I,\theta_I)\mathbf{R}(r,\theta,z,r_I,\theta_I,z_I)}{[r^2 + r_I^2 - 2rr_I\cos(\theta-\theta_I) + (z-z_I)^2]^{3/2}}\,dv \\ &+ \iint_s \frac{\sigma_{mo}^I(z_I,\theta_I)\mathbf{R}(r,\theta,z,r_{Io},\theta_I,z_I)}{[r^2 + r_{Io}^2 - 2rr_{Io}\cos(\theta-\theta_I) + (z-z_I)^2]^{3/2}}\,ds \\ &+ \iint_s \frac{\sigma_{mi}^I(z_I,\theta_I)\mathbf{R}(r,\theta,z,r_{Ii},\theta_I,z_I)}{[r^2 + r_{Ii}^2 - 2rr_{Ii}\cos(\theta-\theta_I) + (z-z_I)^2]^{3/2}}\,ds\}\end{aligned} \tag{4.148}$$

Substituting (4.136)-(4.138) into (4.148) gives:

$$\begin{aligned}\mathbf{B}^I(r,\theta,z) = &-\frac{\mu_0 M_f}{4\pi\mu_r}\int_0^{2\pi}\int_{-L_I/2}^{L_I/2}\int_{r_{Ii}}^{r_{Io}} \frac{(1-k_I r_I)\cos(k_I z_I + \theta_I)\mathbf{R}(r,\theta,z,r_I,\theta_I,z_I)}{[r^2 + r_I^2 - 2rr_I\cos(\theta-\theta_I) + (z-z_I)^2]^{3/2}}\,dr_I\,d\theta_I\,dz_I \\ &+ \frac{\mu_0 M_f}{4\pi}\int_{-L_I/2}^{L_I/2}\int_0^{2\pi} \frac{r_{Io}\cos(k_I z_I + \theta_I)\mathbf{R}(r,\theta,z,r_{Io},\theta_I,z_I)}{[r^2 + r_{Io}^2 - 2rr_{Io}\cos(\theta-\theta_I) + (z-z_I)^2]^{3/2}}\,d\theta_I\,dz_I \\ &- \frac{\mu_0 M_f}{4\pi}\int_{-L_I/2}^{L_I/2}\int_0^{2\pi} \frac{r_{Ii}\cos(k_I z_I + \theta_I)\mathbf{R}(r,\theta,z,r_{Ii},\theta_I,z_I)}{[r^2 + r_{Ii}^2 - 2rr_{Ii}\cos(\theta-\theta_I) + (z-z_I)^2]^{3/2}}\,d\theta_I\,dz_I\end{aligned} \tag{4.149}$$

Substituting **R** from (4.56) into (4.149) one can calculate different components of the magnetic flux density:

$$B_r^I(r,\theta,z) = -\frac{\mu_0 M_f}{4\pi\mu_r}\int_0^{2\pi}\int_{-L_I/2}^{L_I/2}\int_{r_{Ii}}^{r_{Io}} \frac{(1-k_I r_I)\cos(k_I z_I+\theta_I)[r-r_I\cos(\theta-\theta_I)]}{[r^2+r_I^2-2rr_I\cos(\theta-\theta_I)+(z-z_I)^2]^{3/2}} dr_I d\theta_I dz_I$$
$$+\frac{\mu_0 M_f}{4\pi}\int_{-L_I/2}^{L_I/2}\int_0^{2\pi} \frac{r_{Io}\cos(k_I z_I+\theta_I)[r-r_{Io}\cos(\theta-\theta_I)]}{[r^2+r_{Io}^2-2rr_{Io}\cos(\theta-\theta_I)+(z-z_I)^2]^{3/2}} d\theta_I dz_I \quad (4.150)$$
$$-\frac{\mu_0 M_f}{4\pi}\int_{-L_I/2}^{L_I/2}\int_0^{2\pi} \frac{r_{Ii}\cos(k_I z_I+\theta_I)[r-r_{Ii}\cos(\theta-\theta_I)]}{[r^2+r_{Ii}^2-2rr_{Ii}\cos(\theta-\theta_I)+(z-z_I)^2]^{3/2}} d\theta_I dz_I$$

Using the definition (4.59), (4.150) becomes:

$$B_r^I(r,\theta,z) = -\frac{\mu_0 M_f}{4\pi\mu_r}\int_{-L_I/2}^{L_I/2}\int_0^{2\pi} \cos(k_I z_I+\theta_I)[\psi_1(r_{Io},\theta_I,z_I)-\psi_1(r_{Ii},\theta_I,z_I)] d\theta_I dz_I$$
$$+\frac{\mu_0 M_f}{4\pi}\int_{-L_I/2}^{L_I/2}\int_0^{2\pi} \frac{r_{Io}\cos(k_I z_I+\theta_I)[r-r_{Io}\cos(\theta-\theta_I)]}{[r^2+r_{Io}^2-2rr_{Io}\cos(\theta-\theta_I)+(z-z_I)^2]^{3/2}} d\theta_I dz_I \quad (4.151)$$
$$-\frac{\mu_0 M_f}{4\pi}\int_{-L_I/2}^{L_I/2}\int_0^{2\pi} \frac{r_{Ii}\cos(k_I z_I+\theta_I)[r-r_{Ii}\cos(\theta-\theta_I)]}{[r^2+r_{Ii}^2-2rr_{Ii}\cos(\theta-\theta_I)+(z-z_I)^2]^{3/2}} d\theta_I dz_I$$

The $B_\theta$ component can be calculated as follow:

$$B_\theta^I(r,\theta,z) = -\frac{\mu_0 M_f}{4\pi\mu_r}\int_0^{2\pi}\int_{-L_I/2}^{L_I/2}\int_{r_{Ii}}^{r_{Io}} \frac{(1-k_I r_I)\cos(k_I z_I+\theta_I)[r_I\sin(\theta-\theta_I)]}{[r^2+r_I^2-2rr_I\cos(\theta-\theta_I)+(z-z_I)^2]^{3/2}} dr_I d\theta_I dz_I$$
$$+\frac{\mu_0 M_f}{4\pi}\int_{-L_I/2}^{L_I/2}\int_0^{2\pi} \frac{r_{Io}\cos(k_I z_I+\theta_I)[r_{Io}\sin(\theta-\theta_I)]}{[r^2+r_{Io}^2-2rr_{Io}\cos(\theta-\theta_I)+(z-z_I)^2]^{3/2}} d\theta_I dz_I \quad (4.152)$$
$$-\frac{\mu_0 M_f}{4\pi}\int_{-L_I/2}^{L_I/2}\int_0^{2\pi} \frac{r_{Ii}\cos(k_I z_I+\theta_I)[r_{Ii}\sin(\theta-\theta_I)]}{[r^2+r_{Ii}^2-2rr_{Ii}\cos(\theta-\theta_I)+(z-z_I)^2]^{3/2}} d\theta_I dz_I$$

Using the integral solution (4.62), (4.152) becomes:

$$B_\theta^I(r,\theta,z) = -\frac{\mu_0 M_f}{4\pi\mu_r}\int_{-L_I/2}^{L_I/2}\int_0^{2\pi} \cos(k_I z_I+\theta_I)\sin(\theta-\theta_I)[\psi_2(\theta_I,z_I,r_{Io})-\psi_2(\theta_I,z_I,r_{Ii})] d\theta_I dz_I$$
$$+\frac{\mu_0 M_f}{4\pi}\int_{-L_I/2}^{L_I/2}\int_0^{2\pi} \frac{r_{Io}\cos(k_I z_I+\theta_I)[r_{Io}\sin(\theta-\theta_I)]}{[r^2+r_{Io}^2-2rr_{Io}\cos(\theta-\theta_I)+(z-z_I)^2]^{3/2}} d\theta_I dz_I \quad (4.153)$$
$$-\frac{\mu_0 M_f}{4\pi}\int_{-L_I/2}^{L_I/2}\int_0^{2\pi} \frac{r_{Ii}\cos(k_I z_I+\theta_I)[r_{Ii}\sin(\theta-\theta_I)]}{[r^2+r_{Ii}^2-2rr_{Ii}\cos(\theta-\theta_I)+(z-z_I)^2]^{3/2}} d\theta_I dz_I$$

The axial component of the magnetic flux density can be calculated as:

$$B_z^I\left(r,\theta,z\right) = -\frac{\mu_0 M_f}{4\pi\mu_r}\int_0^{2\pi}\int_{-L_I/2}^{L_I/2}\int_{r_{Ii}}^{r_{Io}} \frac{(1-k_I r_I)\cos(k_I z_I+\theta_I)(z-z_I)}{[r^2+r_I^2-2rr_I\cos(\theta-\theta_I)+(z-z_I)^2]^{3/2}}\,dr_I\,d\theta_I\,dz_I$$
$$+\frac{\mu_0 M_f}{4\pi}\int_{-L_I/2}^{L_I/2}\int_0^{2\pi}\frac{r_{Io}\cos(k_I z_I+\theta_I)(z-z_I)}{[r^2+r_{Io}^2-2rr_{Io}\cos(\theta-\theta_I)+(z-z_I)^2]^{3/2}}\,d\theta_I\,dz_I \tag{4.154}$$
$$-\frac{\mu_0 M_f}{4\pi}\int_{-L_I/2}^{L_I/2}\int_0^{2\pi}\frac{r_{Ii}\cos(k_I z_I+\theta_I)(z-z_I)}{[r^2+r_{Ii}^2-2rr_{Ii}\cos(\theta-\theta_I)+(z-z_I)^2]^{3/2}}\,d\theta_I\,dz_I$$

Using the definition (4.65), (4.154) becomes:

$$B_z^I\left(r,\theta,z\right) = -\frac{\mu_0 M_f}{4\pi\mu_r}\int_{-L_I/2}^{L_I/2}\int_0^{2\pi}\cos(k_I z_I+\theta_I)(z-z_I)[\psi_3(r_{Io},\theta_I,z_I)-\psi_3(r_{Ii},\theta_I,z_I)]\,d\theta_I\,dz_I$$
$$+\frac{\mu_0 M_f}{4\pi}\int_{-L_I/2}^{L_I/2}\int_0^{2\pi}\frac{r_{Io}\cos(k_I z_I+\theta_I)(z-z_I)}{[r^2+r_{Io}^2-2rr_{Io}\cos(\theta-\theta_I)+(z-z_I)^2]^{3/2}}\,d\theta_I\,dz_I \tag{4.155}$$
$$-\frac{\mu_0 M_f}{4\pi}\int_{-L_I/2}^{L_I/2}\int_0^{2\pi}\frac{r_{Ii}\cos(k_I z_I+\theta_I)(z-z_I)}{[r^2+r_{Ii}^2-2rr_{Ii}\cos(\theta-\theta_I)+(z-z_I)^2]^{3/2}}\,d\theta_I\,dz_I$$

### 4.3.2 Force on Magnetic Lead Screw

The axial and cross-sectional parameters of the MLS are shown in Fig. 4-22. The indices I and II are assigned to the inner and outer translators respectively. Letters *S* and *V* denote surface and volume.

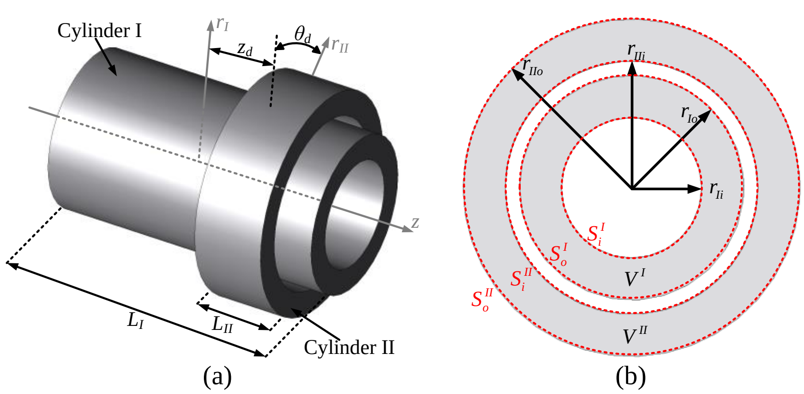


Fig. 4-22. Magnetic lead screw, a) axial parameters, and b) cross sectional parameters

Four surface and two volume charge functions must be considered for the force calculation. Due to interaction of these six components force can be defined as follow:

$$F(z_d,\theta_d) = F_{SS}(z_d,\theta_d)+F_{SV}(z_d,\theta_d)+F_{VV}(z_d,\theta_d) \tag{4.156}$$

where $F_{SS}(z_d, \theta_d)$ is the force between two charge cylinders located at $r = r_I$ and $r = r_{II}$; $F_{SV}(z_d, \theta_d)$ is the force between inner volume and outer charge cylinders, $F_{VS}(z_d, \theta_d)$ is the force between outer volume and inner charge cylinders and $F_{VV}(z_d, \theta_d)$ is the force between inner and outer volume charges. The axial and rotational shift between two cylinders are denoted as $z_d$ and $\theta_d$, respectively. Charge functions for the inner translator are defined by (4.136)-(4.138), and charge functions for the outer Halbach magnetic cylinder are written as:

$$\rho_m^{II}(z_{II} - z_d, \theta_{II} - \theta_d) = -(\frac{1}{\mu_r r_{II}} + \frac{k_{II}}{\mu_r})M_f \cos[k_{II}(z_{II} - z_d) + (\theta_{II} - \theta_d)] \quad (4.157)$$

$$\sigma_{mo}^{II}(z_{II} - z_d, \theta_{II} - \theta_d) = M_f \cos[k_{II}(z_{II} - z_d) + (\theta_{II} - \theta_d)] \quad (4.158)$$

$$\sigma_{mi}^{II}(z_{II} - z_d, \theta_{II} - \theta_d) = -M_f \cos[k_{II}(z_{II} - z_d) + (\theta_{II} - \theta_d)] \quad (4.159)$$

where

$$k_{II} = \frac{2\pi p_{II}}{L_{II}} \quad (4.160)$$

where $L_{II}$ and $p_{II}$ are the axial length and the number of pole-pairs of the outer Halbach array, respectively. Like with the LPMC, as the number of pole-pairs within the active length of the MLS is the same for both inner and outer cylinders, then:

$$k_{II} = k_I = k \quad (4.161)$$

#### 4.3.2.1 General Surface Force Components

The energy between a surface of cylinder I, $S^I$, and a surface of cylinder II, $S^{II}$, can be calculated as [95]:

$$W_{SS}(z_d,\theta_d)=\mu_0\int_{-L_{II}/2}^{L_{II}/2}\int_0^{2\pi}\phi_S^I(r_{II},\theta_{II},z_{II})\sigma_m^{II}(z_{II}-z_d,\theta_{II}-\theta_d)r_{II}d\theta_{II}dz_{II} \tag{4.162}$$

The force is computed from:

$$F_{SS}(z_d,\theta_d)=\left.\frac{\partial W_{SS}(r_I,r_{II})}{\partial z_{II}}\right|_{\phi^I=\text{constant}} \tag{4.163}$$

Therefore:

$$F_{SS}(z_d,\theta_d)=\mu_0\int_{-L_{II}/2}^{L_{II}/2}\int_0^{2\pi}\phi_S^I(r_{II},\theta_{II},z_{II})\frac{\partial\sigma_m^{II}}{\partial z_d}r_{II}d\theta_{II}dz_{II} \tag{4.164}$$

Form (4.158) and (4.159) the surface charge density on cylinder II is:

$$\sigma_m^{II}(z_{II}-z_d,\theta_{II}-\theta_d)=\pm M_f\cos[k_{II}(z_{II}-z_d)+(\theta_{II}-\theta_d)] \tag{4.165}$$

where positive and negative signs are for the outer and inner surfaces of the cylinder II respectively.

From (4.145) the magnetic scalar potential field on cylinder II at ($r$, $\theta$, $z$) = ($r_{II}$, $\theta_{II}$, $z_{II}$) created by a charge cylinder located at $r_I$ is given by:

$$\phi_S^I(r_{II},\theta_{II},z_{II})=\pm\frac{M_f}{4\pi}\int_{-L_I/2}^{L_I/2}\int_0^{2\pi}\frac{r_I\cos(k_Iz_I+\theta_I)}{\sqrt{r_{II}^2+r_I^2-2r_{II}r_I\cos(\theta_{II}-\theta_I)+(z_{II}-z_I)^2}}d\theta_Idz_I \tag{4.166}$$

Depending on which surface is being considered $r_I$ can be $r_{Ii}$ or $r_{Io}$. Positive and negative signs refer to the outer and inner surfaces of the cylinder I, respectively.

Substituting (4.165) and (4.166) into (4.164) gives:

$$\begin{aligned}F_{SS}(z_d,\theta_d)=\pm\frac{k\mu_0M_f^2}{4\pi}&\int_{-L_{II}/2}^{L_{II}/2}\int_0^{2\pi}\int_{-L_I/2}^{L_I/2}\int_0^{2\pi}\\&\frac{r_Ir_{II}\sin[k(z_{II}-z_d)+(\theta_{II}-\theta_d)]\cos(kz_I+\theta_I)}{\sqrt{r_{II}^2+r_I^2-2r_{II}r_I\cos(\theta_{II}-\theta_I)+(z_{II}-z_I)^2}}d\theta_Idz_Id\theta_{II}dz_{II}\end{aligned} \tag{4.167}$$

Changing the angular variables based on the (4.79)-(4.80), (4.167) becomes:

$$F_{SS}(z_d,\theta_d)=\pm\frac{k\mu_0 M_f^2}{4\pi}\int_{-L_{II}/2}^{L_{II}/2}\int_0^{2\pi}\int_{-L_I/2}^{L_I/2}\int_0^{2\pi} \frac{r_I r_{II}\sin[k(z_{II}-z_d)+(\theta_{II}-\theta_d)]\cos[kz_I+(\theta_{II}-\theta_a)]}{\sqrt{r_{II}^2+r_I^2-2r_{II}r_I\cos(\theta_a)+(z_{II}-z_I)^2}}d\theta_a dz_I d\theta_{II} dz_{II} \tag{4.168}$$

Using the trigonometric identity:

$$\cos\alpha\sin\beta=\frac{1}{2}[\sin(\alpha+\beta)-\sin(\alpha-\beta)] \tag{4.169}$$

Numerator of the (4.168) becomes:

$$\begin{aligned}&\cos[kz_I+(\theta_{II}-\theta_a)]\sin[k(z_{II}-z_d)+(\theta_{II}-\theta_d)]=\\&\frac{1}{2}\{\sin[k(z_{II}+z_I-z_d)+2\theta_{II}-\theta_d-\theta_a]-\sin[k(z_I-z_{II}+z_d)-\theta_a+\theta_d]\}\end{aligned} \tag{4.170}$$

Integration over one period of a sine function is zero. Therefore, only the second term of (4.170) results in non-zero force. Equation (4.168) becomes:

$$F_{SS}(z_d,\theta_d)=\pm\frac{k\mu_0 M_f^2}{8\pi}\int_{-L_{II}/2}^{L_{II}/2}\int_0^{2\pi}\int_{-L_I/2}^{L_I/2}\int_0^{2\pi} \frac{r_I r_{II}\sin[k(z_I-z_{II}+z_d)-\theta_a+\theta_d]}{\sqrt{r_{II}^2+r_I^2-2r_{II}r_I\cos(\theta_a)+(z_{II}-z_I)^2}}d\theta_a dz_I d\theta_{II} dz_{II} \tag{4.171}$$

As the integral is not a function of $\theta_{II}$, (4.171) reduces to:

$$F_{SS}(z_d,\theta_d)=\pm\frac{k\mu_0 M_f^2}{4}\int_{-L_{II}/2}^{L_{II}/2}\int_{-L_I/2}^{L_I/2}\int_0^{2\pi} \frac{r_I r_{II}\sin[k(z_I-z_{II}+z_d)-\theta_a+\theta_d]}{\sqrt{r_{II}^2+r_I^2-2r_{II}r_I\cos(\theta_a)+(z_{II}-z_I)^2}}d\theta_a dz_I dz_{II} \tag{4.172}$$

where the negative sign is used when considering $(r_I, r_{II}) = (r_{Ii}, r_{IIo})$ or $(r_I, r_{II}) = (r_{Io}, r_{IIi})$ and the positive sign is used when $(r_I, r_{II}) = (r_{Ii}, r_{IIi})$ or $(r_I, r_{II}) = (r_{Io}, r_{IIo})$.

#### 4.3.2.2 Surface and Volume Force Components

The energy content of the volume charge region $V^{II}$ and surface charge region $S^{I}$ can be calculated as:

$$W_{SV}(z_d,\theta_d)=\mu_0\int_{r_{IIi}}^{r_{IIo}}\int_{-L_{II}/2}^{L_{II}/2}\int_0^{2\pi}\phi_S^I(r_{II},\theta_{II},z_{II})\rho_m^{II}(z_{II}-z_d,\theta_{II}-\theta_d)r_{II}d\theta_{II}dz_{II}dr_{II} \tag{4.173}$$

Force is calculated as:

$$F_{SV}(r_I,r_{II})=\mu_0\int_{r_{IIi}}^{r_{IIo}}\int_{-L_{II}/2}^{L_{II}/2}\int_0^{2\pi}\phi_S^I(r_{II},\theta_{II},z_{II})\frac{\partial\rho_m^{II}}{\partial z_{II}}r_{II}d\theta_{II}dz_{II}dr_{II} \tag{4.174}$$

Substituting (4.157) and (4.166) into (4.174) gives:

$$\begin{aligned}F_{SV}(z_d,\theta_d)=\pm\frac{k\mu_0M_f^2}{4\pi\mu_r}\int_{r_{IIi}}^{r_{IIo}}\int_{-L_{II}/2}^{L_{II}/2}\int_0^{2\pi}\int_{-L_I/2}^{L_I/2}\int_0^{2\pi}\\ \frac{\cos(kz_I+\theta_I)\sin[k(z_{II}-z_d)+(\theta_{II}-\theta_d)](1+kr_{II})}{\sqrt{r_{II}^2+r_I^2-2r_{II}r_I\cos(\theta_{II}-\theta_I)+(z_{II}-z_I)^2}}r_Id\theta_Idz_Id\theta_{II}dz_{II}dr_{II}\end{aligned} \tag{4.175}$$

Using definitions (4.79)-(4.80) for the angular variables, the equation (4.175) becomes:

$$\begin{aligned}F_{SV}(z_d,\theta_d)=\pm\frac{k\mu_0M_f^2}{4\pi\mu_r}\int_{r_{IIi}}^{r_{IIo}}\int_{-L_{II}/2}^{L_{II}/2}\int_0^{2\pi}\int_{-L_I/2}^{L_I/2}\int_0^{2\pi}\\ \frac{\cos[kz_I+(\theta_{II}-\theta_a)]\sin[k(z_{II}-z_d)+(\theta_{II}-\theta_d)](1+kr_{II})}{\sqrt{r_{II}^2+r_I^2-2r_{II}r_I\cos(\theta_a)+(z_{II}-z_I)^2}}r_Id\theta_adz_Id\theta_{II}dz_{II}dr_{II}\end{aligned} \tag{4.176}$$

Using Trigonometric identity of (4.170), the only non-zero component is as follow:

$$\begin{aligned}F_{SV}(z_d,\theta_d)=\pm\frac{k\mu_0M_f^2}{8\pi\mu_r}\int_{r_{IIi}}^{r_{IIo}}\int_{-L_{II}/2}^{L_{II}/2}\int_0^{2\pi}\int_{-L_I/2}^{L_I/2}\int_0^{2\pi}\\ \frac{\sin[k(z_I-z_{II}+z_d)-\theta_a+\theta_d](1+kr_{II})}{\sqrt{r_{II}^2+r_I^2-2r_{II}r_I\cos(\theta_a)+(z_{II}-z_I)^2}}r_Id\theta_adz_Id\theta_{II}dz_{II}dr_{II}\end{aligned} \tag{4.177}$$

As the integrand is not a function of $\theta_{II}$, (4.177) simplifies to:

$$F_{SV}(z_d,\theta_d)=\pm\frac{k\mu_0 M_f^2}{4\mu_r}\int_{r_{IIi}}^{r_{IIo}}\int_{-L_{II}/2}^{L_{II}/2}\int_{-L_I/2}^{L_I/2}\int_0^{2\pi}$$
$$\frac{\sin[k(z_I-z_{II}+z_d)-\theta_a+\theta_d](1+kr_{II})}{\sqrt{r_{II}^2+r_I^2-2r_{II}r_I\cos(\theta_a)+(z_{II}-z_I)^2}}r_I d\theta_a dz_I dz_{II} dr_{II} \tag{4.178}$$

using the definition (4.88), (4.178) becomes:

$$F_{SV}(z_d,\theta_d)=\pm\frac{k\mu_0 M_f^2}{4\mu_r}\int_{-L_{II}/2}^{L_{II}/2}\int_{-L_I/2}^{L_I/2}\int_0^{2\pi}$$
$$[\psi_4(r_I,r_{IIo})-\psi_4(r_I,r_{IIi})]\sin[k(z_I-z_{II}+z_d)-\theta_a+\theta_d]r_I d\theta_a dz_I dz_{II} \tag{4.179}$$

where the negative sign is used when considering $r_I = r_{Io}$ and the positive sign is for $r_I = r_{Ii}$.

Similarly, energy content of the volume charge region of $V^I$ and surface charge region of $S^{II}$ is calculated as:

$$W_{VS}(z_d,\theta_d)=\mu_0\int_{-L_{II}/2}^{L_{II}/2}\int_0^{2\pi}\phi_V^I(r_{II},\theta_{II},z_{II})\sigma_m^{II}(z_{II}-z_d,\theta_{II}-\theta_d)r_{II}d\theta_{II}dz_{II} \tag{4.180}$$

Then the force can be calculated as:

$$F_{VS}(z_d,\theta_d)=\mu_0\int_{-L_{II}/2}^{L_{II}/2}\int_0^{2\pi}\phi_V^I(r_{II},\theta_{II},z_{II})\frac{\partial\sigma_m^{II}}{\partial z_{II}}r_{II}d\theta_{II}dz_{II} \tag{4.181}$$

Substituting (4.147) and (4.165) into (4.181) gives:

$$F_{VS}(z_d,\theta_d)=\pm\frac{k\mu_0 M_f^2}{4\pi\mu_r}\int_{-L_{II}/2}^{L_{II}/2}\int_0^{2\pi}\int_{-L_I/2}^{L_I/2}\int_0^{2\pi}\int_{r_{Ii}}^{r_{Io}}$$
$$\frac{\cos(kz_I+\theta_I)\sin[k(z_{II}-z_d)+(\theta_{II}-\theta_d)](1-kr_I)}{\sqrt{r_{II}^2+r_I^2-2r_{II}r_I\cos(\theta_{II}-\theta_I)+(z_{II}-z_I)^2}}r_{II}dr_I d\theta_I dz_I d\theta_{II} dz_{II} \tag{4.182}$$

Using definitions (4.79)-(4.80) for the angular variables, the equation (4.182) becomes:

$$F_{VS}(z_d,\theta_d)=\pm\frac{k\mu_0 M_f^2}{4\pi\mu_r}\int_{-L_{II}/2}^{L_{II}/2}\int_0^{2\pi}\int_{-L_I/2}^{L_I/2}\int_0^{2\pi}\int_{r_{Ii}}^{r_{Io}}$$
$$\frac{\cos[kz_I+(\theta_{II}-\theta_a)]\sin[k(z_{II}-z_d)+(\theta_{II}-\theta_d)](1-kr_I)}{\sqrt{r_{II}^2+r_I^2-2r_{II}r_I\cos(\theta_a)+(z_{II}-z_I)^2}}r_{II}dr_Id\theta_Idz_Id\theta_{II}dz_{II} \tag{4.183}$$

Using Trigonometric identity of (4.170), the only non-zero component is as follow:

$$F_{VS}(z_d,\theta_d)=\pm\frac{k\mu_0 M_f^2}{8\pi\mu_r}\int_{-L_{II}/2}^{L_{II}/2}\int_0^{2\pi}\int_{-L_I/2}^{L_I/2}\int_0^{2\pi}\int_{r_{Ii}}^{r_{Io}}$$
$$\frac{\sin[k(z_I-z_{II}+z_d)-\theta_a+\theta_d](1-kr_I)}{\sqrt{r_{II}^2+r_I^2-2r_{II}r_I\cos(\theta_a)+(z_{II}-z_I)^2}}r_{II}dr_Id\theta_Idz_Id\theta_{II}dz_{II} \tag{4.184}$$

As the integrand is not a function of $\theta_{II}$, (4.184) simplifies to:

$$F_{VS}(z_d,\theta_d)=\pm\frac{k\mu_0 M_f^2}{4\mu_r}\int_{r_{Ii}}^{r_{Io}}\int_{-L_{II}/2}^{L_{II}/2}\int_{-L_I/2}^{L_I/2}\int_0^{2\pi}$$
$$\frac{\sin[k(z_I-z_{II}+z_d)-\theta_a+\theta_d](1-kr_I)}{\sqrt{r_{II}^2+r_I^2-2r_{II}r_I\cos(\theta_a)+(z_{II}-z_I)^2}}r_{II}d\theta_Idz_Idz_{II}dr_I \tag{4.185}$$

Using definition (4.95), (4.185) simplifies to:

$$F_{VS}(z_d,\theta_d)=\pm\frac{k\mu_0 M_f^2}{4\mu_r}\int_{-L_{II}/2}^{L_{II}/2}\int_{-L_I/2}^{L_I/2}\int_0^{2\pi}[\psi_5(r_{Io},r_{II})-\psi_5(r_{Ii},r_{II})]$$
$$\sin[k(z_I-z_{II}+z_d)-\theta_a+\theta_d](1-kr_I)r_{II}d\theta_Idz_Idz_{II} \tag{4.186}$$

where negative sign is when considering $S_o^{II}$ and the positive sign is for $S_i^{II}$.

#### 4.3.2.3 Volume Force Components

Energy content of the volume charge regions of $V^I$ and $V^{II}$ can be calculated as:

$$W_{VV}(z_d,\theta_d)=\mu_0\int_{r_{IIi}}^{r_{IIo}}\int_{-L_{II}/2}^{L_{II}/2}\int_0^{2\pi}\phi_V^I(r_{II},\theta_{II},z_{II})\rho_m^{II}(z_{II}-z_d,\theta_{II}-\theta_d)r_{II}d\theta_{II}dz_{II}dr_{II} \tag{4.187}$$

The Force then is calculated as:

$$F_{VV}(z_d,\theta_d)=\mu_0\int_{r_{IIi}}^{r_{IIo}}\int_{-L_{II}/2}^{L_{II}/2}\int_0^{2\pi}\phi_V^I(r_{II},\theta_{II},z_{II})\frac{\partial\rho_m^{II}}{\partial z_{II}}r_{II}\,d\theta_{II}\,dz_{II}\,dr_{II} \tag{4.188}$$

Substituting (4.147) and (4.157) into (4.188) gives:

$$\begin{aligned}F_{VV}(z_d,\theta_d)&=+\frac{k\mu_0M_f^2}{4\pi\mu_r^2}\int_{r_{IIi}}^{r_{IIo}}\int_{-L_{II}/2}^{L_{II}/2}\int_0^{2\pi}\int_0^{2\pi}\int_{-L_I/2}^{L_I/2}\int_{r_{Ii}}^{r_{Io}}\\&\frac{\cos(kz_I+\theta_I)\sin[k(z_{II}-z_d)+(\theta_{II}-\theta_d)](1+kr_{II})(1-kr_I)}{\sqrt{r_{II}^2+r_I^2-2r_{II}r_I\cos(\theta_{II}-\theta_I)+(z_{II}-z_I)^2}}dr_I\,d\theta_I\,dz_I\,d\theta_{II}\,dz_{II}\,dr_{II}\end{aligned} \tag{4.189}$$

Changing the angular variables based on (4.79) gives:

$$\begin{aligned}F_{VV}(z_d,\theta_d)&=+\frac{k\mu_0M_f^2}{4\pi\mu_r^2}\int_{r_{IIi}}^{r_{IIo}}\int_{-L_{II}/2}^{L_{II}/2}\int_0^{2\pi}\int_0^{2\pi}\int_{-L_I/2}^{L_I/2}\int_{r_{Ii}}^{r_{Io}}\frac{(1+kr_{II})(1-kr_I)}{\sqrt{r_{II}^2+r_I^2-2r_{II}r_I\cos(\theta_a)+(z_{II}-z_I)^2}}\\&\cos[kz_I+(\theta_{II}-\theta_a)]\sin[k(z_{II}-z_d)+(\theta_{II}-\theta_d)]dr_I\,d\theta_a\,dz_I\,d\theta_{II}\,dz_{II}\,dr_{II}\end{aligned} \tag{4.190}$$

Using the trigonometric identity of (4.170) one can obtain:

$$\begin{aligned}F_{VV}(z_d,\theta_d)&=+\frac{k\mu_0M_f^2}{8\pi\mu_r^2}\int_{r_{IIi}}^{r_{IIo}}\int_{-L_{II}/2}^{L_{II}/2}\int_0^{2\pi}\int_0^{2\pi}\int_{-L_I/2}^{L_I/2}\int_{r_{Ii}}^{r_{Io}}\\&\frac{\sin[k(z_I-z_{II}+z_d)-\theta_a+\theta_d](1+kr_{II})(1-kr_I)}{\sqrt{r_{II}^2+r_I^2-2r_{II}r_I\cos(\theta_a)+(z_{II}-z_I)^2}}dr_I\,d\theta_a\,dz_I\,d\theta_{II}\,dz_{II}\,dr_{II}\end{aligned} \tag{4.191}$$

As the integrand is not a function of $\theta_{II}$, (4.191) reduces to:

$$\begin{aligned}F_{VV}(z_d,\theta_d)&=+\frac{k\mu_0M_f^2}{4\mu_r^2}\int_{r_{Ii}}^{r_{Io}}\int_{r_{IIi}}^{r_{IIo}}\int_{-L_{II}/2}^{L_{II}/2}\int_{-L_I/2}^{L_I/2}\int_0^{2\pi}\\&\frac{\sin[k(z_I-z_{II}+z_d)-\theta_a+\theta_d](1+kr_{II})(1-kr_I)}{\sqrt{r_{II}^2+r_I^2-2r_{II}r_I\cos(\theta_a)+(z_{II}-z_I)^2}}d\theta_a\,dz_I\,dz_{II}\,dr_{II}\,dr_I\end{aligned} \tag{4.192}$$

Using definition (4.95), (4.192) becomes:

$$\begin{aligned}F_{VV}(z_d,\theta_d)&=+\frac{k\mu_0M_f^2}{4\mu_r^2}\int_{r_{IIi}}^{r_{IIo}}\int_{-L_{II}/2}^{L_{II}/2}\int_{-L_I/2}^{L_I/2}\int_0^{2\pi}\sin[k(z_I-z_{II}+z_d)-\theta_a+\theta_d]\\&[\psi_5(r_{Io},r_{II})-\psi_5(r_{Ii},r_{II})](1+kr_{II})\,d\theta_a\,dz_I\,dz_{II}\,dr_{II}\end{aligned} \tag{4.193}$$

### 4.3.3 Validation Using Finite Element Analysis

In order to verify the analytic results a 3D FEA model of a Halbach MLS was considered. Fig. 4-23 shows the geometry and the generated mesh using JMAG FEA software for this MLS. This model included a total number of about 1.9 million mesh elements. A summary of the design parameters is given in Table 4-III, which has been chosen to match the analytic model. Both translator have the same number of pole-pairs in the active length, but the inner translator has twice the length of the outer cylinder.

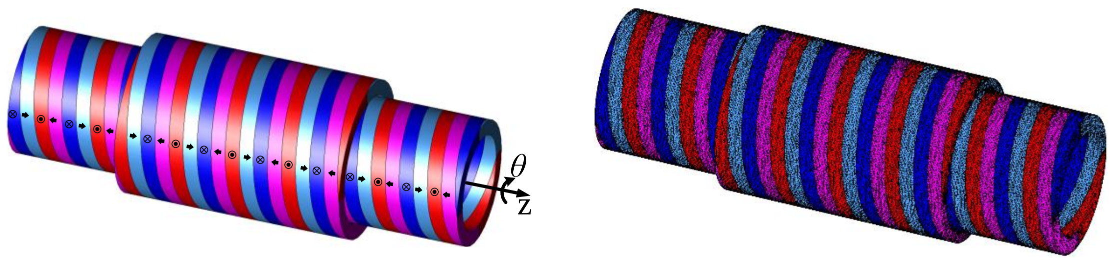


(a) (b)

Fig. 4-23. 3D FEA model of a Halbach MLS

Table 4-III. Summary of geometric and material parameters

| Parameter | | Value | Unit |
|---|---|---|---|
| Inner translator | Inner radius, $r_{Ii}$ | 10 | mm |
| | Outer radius, $r_{Io}$ | 13 | mm |
| | Axial length, $L_I$ | 96 | mm |
| | Number of pole-pairs, $p_I$ | 8 | - |
| | Airgap length, $g$ | 0.4 | mm |
| Outer translator | Inner radius, $r_{IIi}$ | 13.4 | mm |
| | Outer radius, $r_{IIo}$ | 16.4 | mm |
| | Axial length, $L_{II}$ | 48 | mm |
| | Number of pole-pairs, $p_{II}$ | 4 | - |
| Material | NdFeB magnet, $B_r$, NMX-40CH | 1.25 | T |

The calculated radial and axial flux densities using FEA and analytical methods over a line 1mm above the surface of the inner translator, while it was surrounded by air are compared in Fig. 4-24. About 1.2 percent error was calculated. The calculated force using FEA and analytical model is compared in Fig. 4-25 which shows a very good match. The percentage of error is about 1.5 percent at peak.

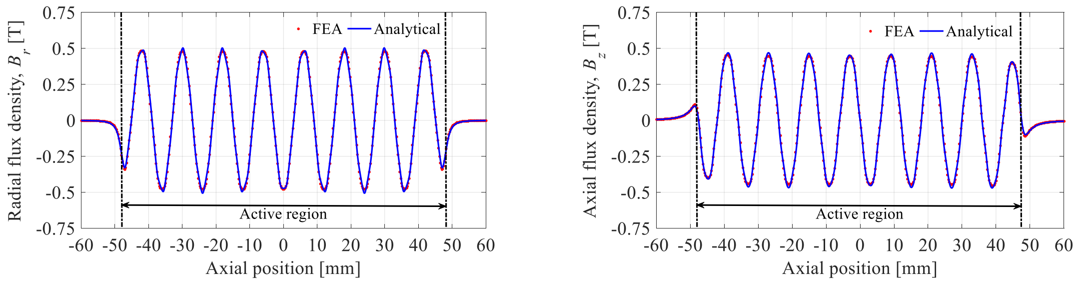


(a) (b)

Fig. 4-24. FEA and analytically calculated flux density a) radial b) axial

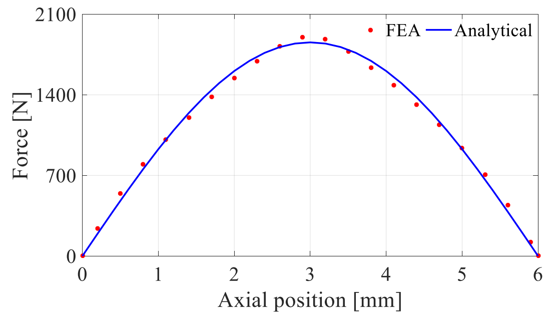


Fig. 4-25. Calculated force using FEA and analytical model

It was observed that LPMC and MLS has the same force capabilities. In order to verify this, two design with different geometric parameters, which are given in Table 4-IV, were considered. Fig. 4-26 shows a comparison of FEA force calculation between LPMC and MLS for Case 1 for different number of pole-pairs. As can be seen LPMC and MLS force is almost the same for LPMC and MLS. Fig. 4-27 shows the same plots for the Case 2 design. Therefore, parametric analysis of the MLS is expected to conclude the same upper bound as the upper bound for the LPMC.

Table 4-IV. Summary of the Fixed Parameter Values for Two Different Cases

| Parameter | | Value | | Unit |
|---|---|---|---|---|
| | | Case 1 | Case 2 | |
| Inner cylinder | Inner radius, $r_{Ii}$ | 9 | 23 | mm |
| | Outer radius, $r_{Io}$ | 18 | 36.5 | mm |
| Outer cylinder | Inner radius, $r_{IIi}$ | 19 | 37.5 | mm |
| | Outer radius, $r_{IIo}$ | 30 | 50 | mm |
| Airgap length, $g$ | | 1 | 1 | mm |
| Pole-pitch, $\tau_p$ | | 9 | 13 | mm |

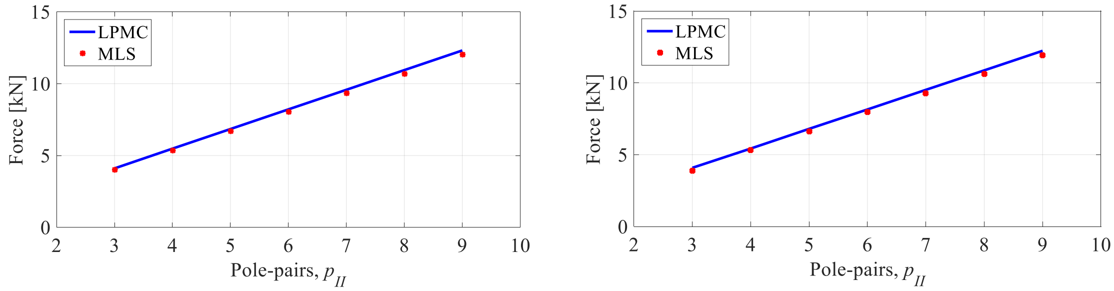


(a) (b)

Fig. 4-26. Case1: calculated force of LPMC and MLS a) using FEA and b) using analytical model

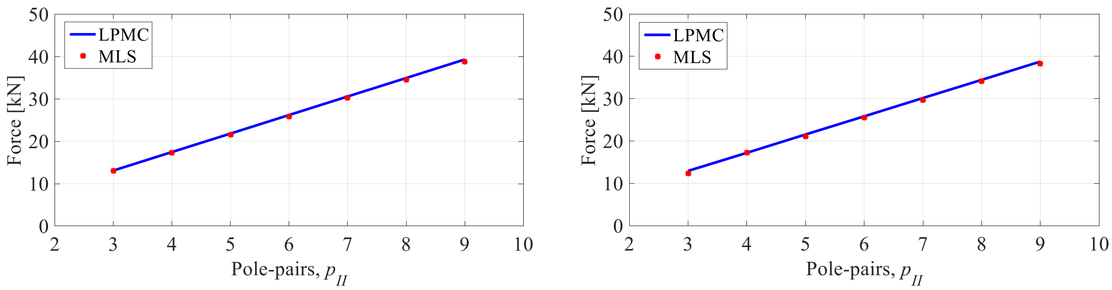


(a) (b)

Fig. 4-27. Case 2: calculated force of LPMC and MLS a) using FEA and b) using analytical model

# 5 Conclusions, Research Contributions and Future Works

## 5.1 Conclusions

A new magnetically geared lead screw has been proposed. The working principles have been demonstrated for the first time. It was shown that for long stroke length applications, the proposed MGLS offers lower force per kg of magnet material in comparison to other magnetic linear actuators. The testing results of the assembled MGLS showed that skewing the steel rings of the translator caused construction problems such as tolerance issues and cost. Therefore, a second version of the MGLS has been proposed, which does not require the skewing of the translator rings. The simple structure of this new MGLS version offers the same performance, while at the same time reduces the cost of manufacturing. The second version has been constructed and tested. The experimental testing verified the operating principle of the MGLS and showed that a considerable amount of friction exists within the structure of the proposed MGLS. As the gear ratio was designed to be 837.7:1, this resulted in the torque being low and made it difficult for the MGLS to overcome the friction losses.

An axial flux magnetic gear has been analyzed and successfully assembled and tested. A peak torque of 553.2 Nm was measured, which resulted in an active region torque density of 152.3 Nm/L. Whilst this is 12 % lower than the calculated value it is significantly higher than prior tested axial MGs. The MG power loss was shown to not increase with load. Therefore, good efficiency was demonstrated at the high torque, low-speed operating condition that were tested.  It was also shown that the torque ripple does not depend on the load and this therefore resulted in a high torque ripple at low load conditions.

A new type of axial flux magnetically geared machine was proposed. The proposed machine consisted of a radial-flux stator placed around the high-speed rotor of the axial flux MG. The stator of the proposed machine shares the high-speed rotor with the axial magnetic gear. Therefore, there is no need for a separate rotor. This also enables the stator to provide additional flux into the magnetic gear in order to boost torque during transients. The axial flux magnetically geared machine was successfully assembled and tested. The peak measured torque and corresponding active region torque density of 473 Nm and 94.4 Nm/L were achieved.

An analytical-based model was developed for a linear permanent magnet coupling and magnetic lead screw. The accuracy of these models were confirmed using finite element analysis results. As this analytical-based model significantly reduces the calculation time, it can be used for parametric analyses and optimization purposes. It also helps to provide a better understanding of the force density limits and design parameters that leads to higher force density when using linear motion magnetic devices.

## 5.2 List of Research Contributions

- A new type of MGLS was proposed [98].
- A new type of MGLS without translator skewing was proposed [99].
- A patent on the new MGLS was published [100].
- A new type of axial flux magnetically geared motor was proposed [78].
- The performance of the MGLS was experimentally verified and practical issues were identified [101].
- The axial flux magnetic gear was experimentally tested [102].

- The performance the axial flux magnetically geared motor was experimentally verified [103].
- An analytical-based model was developed for a linear magnetic coupling [104].
- An analytical-based model was developed for a magnetic lead screw [105]

## 5.3 Further Works

- The MGLS need to be re-designed using different pole-pair combination that reduces the gear ratio. This will help to get a design with higher torque.
- Mechanical design of the MGLS needs to be reconsidered to reduce the friction inside the structure.
- The use of a Halbach PM configuration has been shown to effectively increase the force/torque capability of magnetic devices. The MGLS could take advantage of this configuration to achieve higher force and torque densities.
- Huge axial force within the axial magnetic gear makes the assembly process challenging. The use of magnetomechanical deflection analyses will help to provide a better understanding of these forces.
- Further analysis of the axial flux magnetically geared machine need to be undertaken in terms of modeling the stator geometry, so as to reduce the torque ripple.
- The analytical-based model can be used with optimization algorithms to improve the geometry of magnetic devices.

## References


[1] O. Gomis-Bellmunt and L. F Campanile, *Design Rules for Actuators in Active Mechanical Systems*. London: Springer, 2010.

[2] L. Lucaccini, R. Wisshaupt, H. Groth, and J. Lyman, “Evaluation of the Heidelberg pneumatic prosthesis,” *Bull Prosthet Res*, vol. 5, no. 10, pp. 58–115, 1966.

[3] L. J. Love, R. F. Lind, and J. F. Jansen, “Mesofluidic actuation for articulated finger and hand prosthetics,” in *Proceedings of the 2009 IEEE/RSJ international conference on Intelligent robots and systems*, St. Louis, MO, USA, 2009, pp. 2586–2591.

[4] W. Durfee, J. Xia, and E. Hsiao-Wecksler, “Tiny hydraulics for powered orthotics,” in *2011 IEEE International Conference on Rehabilitation Robotics*, 2011, pp. 1–6.

[5] J. M. Hollerbach, I. W. Hunter, and J. Ballantyne, “A comparative analysis of actuator technologies for robotics,” in *The robotics review 2*, O. Khatib, J. J. Craig, and T. Lozano-Pérez, Eds. MIT Press, 1992, pp. 299–342.

[6] L. Day and I. McNeil, *Biographical dictionary of the history of technology*. London: Routledge, 2002.

[7] J. Xia and W. K. Durfee, “Analysis of Small-Scale Hydraulic Actuation Systems,” *J. Mech. Des.*, vol. 135.

[8] J. E. Huber, N. A. Fleck, and M. F. Ashby, “The selection of mechanical actuators based on performance indices,” *Proc. R. Soc. Lond. Ser. Math. Phys. Eng. Sci.*, vol. 453, no. 1965, p. 2185, Oct. 1997.

[9] W. K. Durfee and Z. Sun, *Fluid Power System Dynamics*. Center for Compact and Efficient Fluid Power (CCEFP), 2009.

[10] A. Privat-Deschanel, *Deschanel Elementary Treatise on Natural Philosophy*, 5th ed. London: Blackie and Son’s, 1880.

[11] *Aviation Maintenance Technician Handbook - Airframe*, vol. 2. United States Department of Transportation, Federal Aviation Administration, 2012.

[12] E. Richer and Y. Hurmuzlu, “A High Performance Pneumatic Force Actuator System: Part I—Nonlinear Mathematical Model,” *J. Dyn. Syst. Meas. Control*, vol. 122, no. 3, pp. 416–425, Jun. 1999.

[13] I. Petrovic, “Ktesibios of Alexandria,” *The Encyclopedia of Ancient History*. Blackwell Publishing Ltd., 2013.

[14] G. Shelton, “Roller Screw Actuators: Benefits, Selection and Maintenance.” Exlar. Available online: https://exlar.com, 2010.

[15] “GSX30, ‘Exlar Full Catalog’. [Online]. Available: https://exlar.com.” .

[16] J. R. Brauer, *Magnetic Actuators and Sensors*, 2nd ed. John Wiley & Sons, Inc., 2006.

[17] P. E. Cavarec, H. B. Ahmed, and B. Multon, “New multi-rod linear actuator for direct-drive, wide mechanical bandpass applications,” *IEEE Trans. Ind. Appl.*, vol. 39, no. 4, pp. 961–970, Aug. 2003.

[18] E. R. Laithwaite, *A History of Linear Electric Motors*. Macmillan, 1987.

[19] J. Pons, *Emerging Actuator Technologies: A Micromechatronic Approach*. John Wiley & Sons Ltd., 2005.

[20] J. F. Eastham, “Novel synchronous machines: linear and disc,” *IEE Proc. B - Electr. Power Appl.*, vol. 137, no. 1, pp. 49–58, Jan. 1990.

[21] S. E. Abdollahi, M. Mirzayee, and M. Mirsalim, “Design and Analysis of a Double-Sided Linear Induction Motor for Transportation,” *IEEE Trans. Magn.*, vol. 51, no. 7, pp. 1–7, Jul. 2015.
[22] H. W. Lee, C. B. Park, and J. Lee, “Improvement of Thrust Force Properties of Linear Synchronous Motor for an Ultra-High-Speed Tube Train,” *IEEE Trans. Magn.*, vol. 47, no. 11, pp. 4629–4634, Nov. 2011.
[23] D. Wang, X. Wang, and X. F. Du, “Design and Comparison of a High Force Density Dual-Side Linear Switched Reluctance Motor for Long Rail Propulsion Application With Low Cost,” *IEEE Trans. Magn.*, vol. 53, no. 6, pp. 1–4, Jun. 2017.
[24] G. W. McLean, “Review of recent progress in linear motors,” *IEE Proc. B Electr. Power Appl.*, vol. 135, no. 6, pp. 380–416, Nov. 1988.
[25] J. Wang, G. W. Jewell, and D. Howe, “Design optimisation and comparison of tubular permanent magnet machine topologies,” *IEE Proc. - Electr. Power Appl.*, vol. 148, no. 5, pp. 456–464, Sep. 2001.
[26] J. Wang and D. Howe, “Tubular modular permanent-magnet machines equipped with quasi-Halbach magnetized magnets-part II: armature reaction and design optimization,” *IEEE Trans. Magn.*, vol. 41, no. 9, pp. 2479–2489, Sep. 2005.
[27] C. H. Lee, “Vernier Motor and Its Design,” *IEEE Trans. Power Appar. Syst.*, vol. 82, no. 66, pp. 343–349, Jun. 1963.
[28] Y. Du *et al.*, “Comparison of Linear Primary Permanent Magnet Vernier Machine and Linear Vernier Hybrid Machine,” *IEEE Trans. Magn.*, vol. 50, no. 11, pp. 1–4, Nov. 2014.
[29] Y. Fujimoto, T. Kominami, and H. Hamada, “Development and Analysis of a High Thrust Force Direct-Drive Linear Actuator,” *IEEE Trans. Ind. Electron.*, vol. 56, no. 5, pp. 1383–1392, May 2009.
[30] H. Faus, “Magnet gearing,” US2243555A, 1941.
[31] S. Kikuchi and K. Tsurumoto, “Design and characteristics of a new magnetic worm gear using permanent magnet,” *IEEE Trans. Magn.*, vol. 29, no. 6, pp. 2923–2925, Nov. 1993.
[32] C. C. Huang, M. C. Tsai, D. G. Dorrell, and B. J. Lin, “Development of a Magnetic Planetary Gearbox,” *IEEE Trans. Magn.*, vol. 44, no. 3, pp. 403–412, Mar. 2008.
[33] A. H. Neuland, *Apparatus for transmitting power.* Google Patents, 1916.
[34] G. A. Reese, *Magnetic gearing arrangement*. Google Patents, 1967.
[35] T. Martin, “Magnetic transmission,” US3378710A, 1968.
[36] K. Atallah and D. Howe, “A novel high-performance magnetic gear,” *IEEE Trans. Magn.*, vol. 37, no. 4, pp. 2844–2846, Jul. 2001.
[37] K. Atallah, S. D. Calverley, and D. Howe, “Design, analysis and realisation of a high-performance magnetic gear,” *IEE Proc. - Electr. Power Appl.*, vol. 151, no. 2, pp. 135–143, Mar. 2004.
[38] S. Mezani, K. Atallah, and D. Howe, “A high-performance axial-field magnetic gear,” *J. Appl. Phys.*, vol. 99, no. 8, p. 08R303, Apr. 2006.
[39] J. Rens, K. Atallah, S. D. Calverley, and D. Howe, “A Novel Magnetic Harmonic Gear,” *IEEE Trans. Ind. Appl.*, vol. 46, no. 1, pp. 206–212, Feb. 2010.
[40] F. T. Jorgensen, T. O. Andersen, and P. O. Rasmussen, “The Cycloid Permanent Magnetic Gear,” *IEEE Trans. Ind. Appl.*, vol. 44, no. 6, pp. 1659–1665, Dec. 2008.

[41] K. Atallah, J. Wang, and D. Howe, “A high-performance linear magnetic gear,” *J. Appl. Phys.*, vol. 97, no. 10, 2005.
[42] K. Atallah, J. Wang, S. Mezani, and D. Howe, “A Novel High-Performance Linear Magnetic Gear,” *IEEJ Trans. Ind. Appl.*, vol. 126, no. 10, pp. 1352–1356, 2006.
[43] R. C. Holehouse, K. Atallah, and J. Wang, “Design and Realization of a Linear Magnetic Gear,” *IEEE Trans. Magn.*, vol. 47, no. 10, pp. 4171–4174, Oct. 2011.
[44] W. Li, K. T. Chau, and J. Z. Jiang, “Application of Linear Magnetic Gears for Pseudo-Direct-Drive Oceanic Wave Energy Harvesting,” *IEEE Trans. Magn.*, vol. 47, no. 10, pp. 2624–2627, Oct. 2011.
[45] W. Li, Shuang Gao, Diyun Wu, and X. Zhang, “Design of a linear magnetic-geared free-piston generator for series hybrid electric vehicles,” in *2010 IEEE Vehicle Power and Propulsion Conference*, 2010, pp. 1–6.
[46] J. Wang, K. Atallah, and W. Wang, “Analysis of a Magnetic Screw for High Force Density Linear Electromagnetic Actuators,” *IEEE Trans. Magn.*, vol. 47, no. 10, pp. 4477–4480, Oct. 2011.
[47] R. K. Holm, N. I. Berg, M. Walkusch, P. O. Rasmussen, and R. H. Hansen, “Design of a Magnetic Lead Screw for Wave Energy Conversion,” *IEEE Trans. Ind. Appl.*, vol. 49, no. 6, pp. 2699–2708, Dec. 2013.
[48] N. I. Berg, R. K. Holm, and P. O. Rasmussen, “Theoretical and Experimental Loss and Efficiency Studies of a Magnetic Lead Screw,” *IEEE Trans. Ind. Appl.*, vol. 51, no. 2, pp. 1438–1445, Apr. 2015.
[49] N. I. Berg, R. K. Holm, and P. O. Rasmussen, “Design and test of a novel magnetic lead screw for active suspension system in a vehicle,” in *Electrical Machines (ICEM), 2014 International Conference on*, 2014, pp. 470–477.
[50] N. I. Berg, A. Becsei Christiansen, R. K. Holm, and P. O. Rasmussen, “Design and test of a reluctance based magnetic lead screw PTO system for a wave energy converter,” in *2017 IEEE International Electric Machines and Drives Conference (IEMDC)*, 2017, pp. 1–8.
[51] K. Lu and W. Wu, “Electromagnetic Lead Screw for Potential Wave Energy Application,” *IEEE Trans. Magn.*, vol. 50, no. 11, pp. 1–4, Nov. 2014.
[52] S. Pakdelian, Y. B. Deshpande, and H. A. Toliyat, “Design of an Electric Machine Integrated with Trans-Rotary Magnetic Gear,” *IEEE Trans. Energy Convers.*, vol. 30, no. 3, pp. 1180–1191, Sep. 2015.
[53] J. Ji, Z. Ling, J. Wang, W. Zhao, G. Liu, and T. Zeng, “Design and Analysis of a Halbach Magnetized Magnetic Screw for Artificial Heart,” *IEEE Trans. Magn.*, vol. 51, no. 11, pp. 1–4, Nov. 2015.
[54] “Maxim #288-321, ‘Grainger Catalog 401’. [Online]. Available: https://www.grainger.com.” .
[55] “Speedaire #5VMV2, ‘Grainger Catalog 401’. [Online]. Available: https://www.grainger.com.” .
[56] Jiabin Wang and D. Howe, “Design optimization of radially magnetized, iron-cored, tubular permanent-magnet machines and drive systems,” *IEEE Trans. Magn.*, vol. 40, no. 5, pp. 3262–3277, Sep. 2004.

[57] W. Li, K. T. Chau, and J. Li, “Simulation of a Tubular Linear Magnetic Gear Using HTS Bulks for Field Modulation,” *IEEE Trans. Appl. Supercond.*, vol. 21, no. 3, pp. 1167–1170, Jun. 2011.

[58] N. Bianchi, S. Bolognani, D. D. Corte, and F. Tonel, “Tubular linear permanent magnet motors: an overall comparison,” *IEEE Trans. Ind. Appl.*, vol. 39, no. 2, pp. 466–475, Apr. 2003.

[59] S. Pakdelian, N. W. Frank, and H. A. Toliyat, “Magnetic Design Aspects of the Trans-Rotary Magnetic Gear,” *IEEE Trans. Energy Convers.*, vol. 30, no. 1, pp. 41–50, Mar. 2015.

[60] K. Lu, Y. Xia, W. Wu, and L. Zhang, “New Helical-Shape Magnetic Pole Design for Magnetic Lead Screw Enabling Structure Simplification,” *IEEE Trans. Magn.*, vol. 51, no. 11, pp. 1–4, Nov. 2015.

[61] American Gear Manufacturers Association. and American National Standards Institute., *Gear nomenclature, definitions of terms with symbols : AGMA standard. ANSI/AGMA 1012-G05*. Alexandria, Va. : American Gear Manufacturers Association, 2005.

[62] M. Zhao and J. Ji, “Dynamic Analysis of Wind Turbine Gearbox Components,” *Energies*, vol. 9, no. 2, 2016.

[63] A. Ragheb and M. Ragheb, “Wind turbine gearbox technologies,” in *2010 1st International Nuclear & Renewable Energy Conference (INREC)*, 2010, pp. 1–8.

[64] P. O. Rasmussen, T. O. Andersen, F. T. Jorgensen, and O. Nielsen, “Development of a high-performance magnetic gear,” *IEEE Trans. Ind. Appl.*, vol. 41, no. 3, pp. 764–770, Jun. 2005.

[65] C. Tong, Z. Song, P. Zheng, J. Bai, and Q. Zhao, “Research on electromagnetic performance of an axial magnetic-field-modulated brushless double-rotor machine for hybrid electric vehicles,” in *2014 17th International Conference on Electrical Machines and Systems (ICEMS)*, 2014, pp. 2896–2902.

[66] F. Caricchi, F. Crescimbini, O. Honorati, A. Di Napoli, and E. Santini, “Compact wheel direct drive for EVs,” *IEEE Ind. Appl. Mag.*, vol. 2, no. 6, pp. 25–32, Dec. 1996.

[67] R. J. Wang, L. Brönn, S. Gerber, and P. M. Tlali, “Design and evaluation of a disc-type magnetically geared PM wind generator,” in *4th International Conference on Power Engineering, Energy and Electrical Drives*, 2013, pp. 1259–1264.

[68] Z. Q. Zhu and D. Howe, “Influence of design parameters on cogging torque in permanent magnet machines,” *IEEE Trans. Energy Convers.*, vol. 15, no. 4, pp. 407–412, Dec. 2000.

[69] M. Johnson, M. C. Gardner, and H. A. Toliyat, “Design and Analysis of an Axial Flux Magnetically Geared Generator,” *IEEE Trans. Ind. Appl.*, vol. 53, no. 1, pp. 97–105, Feb. 2017.

[70] N. Niguchi, K. Hirata, A. Zaini, and S. Nagai, “Proposal of an axial-type magnetic-geared motor,” in *2012 XXth International Conference on Electrical Machines*, 2012, pp. 738–743.

[71] W. N. Fu and S. L. Ho, “A Quantitative Comparative Analysis of a Novel Flux-Modulated Permanent-Magnet Motor for Low-Speed Drive,” *IEEE Trans. Magn.*, vol. 46, no. 1, pp. 127–134, Jan. 2010.

[72] H. Zaytoon, A. S. Abdel-Khalik, A. M. Massoud, and S. Ahmed, "An axial magnetic gearbox with an electric power output port," in *2014 IEEE Applied Power Electronics Conference and Exposition - APEC 2014*, 2014, pp. 2621–2627.
[73] M. F. H. Khatab, Z. Q. Zhu, H. Y. Li, and Y. Liu, "Optimal design of a novel axial flux magnetically geared PM machine," in *2017 Twelfth International Conference on Ecological Vehicles and Renewable Energies (EVER)*, 2017, pp. 1–8.
[74] T. J. Woolmer and M. D. McCulloch, "Analysis of the Yokeless And Segmented Armature Machine," in *2007 IEEE International Electric Machines & Drives Conference*, 2007, vol. 1, pp. 704–708.
[75] H. Yang, B. Kim, Y. Park, W. Lim, and S. Cha, "Analysis of planetary gear hybrid powertrain system part 2: Output split system," *Int. J. Automot. Technol.*, vol. 10, no. 3, pp. 381–390, Jun. 2009.
[76] V. M. Acharya, M. Calvin, and J. Z. Bird, "A low torque ripple flux focusing axial magnetic gear," in *7th IET International Conference on Power Electronics, Machines and Drives (PEMD 2014)*, 2014, pp. 1–6.
[77] V. M. Acharya, "Design of a flux focusing axial magnetic gear," University of North Carolina at Charlotte, 2013.
[78] M. B. Kouhshahi, J. Z. Bird, V. Acharya, K. Li, M. Calvin, and W. Williams, "An axial flux-focusing magnetically geared motor," in *2017 IEEE Energy Conversion Congress and Exposition (ECCE)*, 2017, pp. 307–313.
[79] N. Bianchi and M. Dai Pre, "Use of the star of slots in designing fractional-slot single-layer synchronous motors," *IEE Proc. - Electr. Power Appl.*, vol. 153, no. 3, pp. 459–466, May 2006.
[80] T. A. Lipo, *Analysis of Synchronous Machines*, 2nd edition. CRC Press, 2012.
[81] B. Dolisy, T. Lubin, S. Mezani, and J. Leveque, "Three-Dimensional Analytical Model for an Axial-Field Magnetic Coupling," *Prog. Electromagn. Res. M*, vol. 35, pp. 173–182, 2014.
[82] G. Xiong and S. A. Nasar, "Analysis of fields and forces in a permanent magnet linear synchronous machine based on the concept of magnetic charge," *IEEE Trans. Magn.*, vol. 25, no. 3, pp. 2713–2719, May 1989.
[83] D. L. Trumper, Won-Jong Kim, and M. E. Williams, "Design and analysis framework for linear permanent magnet machines," in *Proceedings of 1994 IEEE Industry Applications Society Annual Meeting*, 1994, vol. 2, pp. 216–223 vol.1.
[84] Z. J. Liu, A. Vourdas, and K. J. Binns, "Magnetic field and eddy current losses in linear and rotating permanent magnet machines with a large number of poles," *IEE Proc. - Sci. Meas. Technol.*, vol. 138, no. 6, pp. 289–294, Nov. 1991.
[85] Jiabin Wang, G. W. Jewell, and D. Howe, "A general framework for the analysis and design of tubular linear permanent magnet machines," *IEEE Trans. Magn.*, vol. 35, no. 3, pp. 1986–2000, May 1999.
[86] K. J. Meessen, B. L. J. Gysen, J. J. H. Paulides, and E. A. Lomonova, "Three-Dimensional Magnetic Field Modeling of a Cylindrical Halbach Array," *IEEE Trans. Magn.*, vol. 46, no. 6, pp. 1733–1736, Jun. 2010.
[87] J. Kim, J. Choi, M. Koo, H. Shin, and S. Lee, "Characteristic Analysis of Tubular-Type Permanent-Magnet Linear Magnetic Coupling Based on Analytical Magnetic Field Calculations," *IEEE Trans. Appl. Supercond.*, vol. 26, no. 4, pp. 1–5, Jun. 2016.

[88] D. Månsson, “On the Optimization of Halbach Arrays as Energy Storage Media,” *Prog. Electromagn. Res. B*, vol. 62, no. 1, pp. 277–288, 2015.
[89] B. E. Paden, C. Chen, and O. J. Fiske, “Magnetic spring and actuators with multiple equilibrium positions,” US7265470B1, 2007.
[90] J. Mallinson, “One-sided fluxes -- A magnetic curiosity?,” *IEEE Trans. Magn.*, vol. 9, no. 4, pp. 678–682, Dec. 1973.
[91] K. Halbach, “Design of permanent multipole magnets with oriented rare earth cobalt material,” *Nucl. Instrum. Methods*, vol. 169, no. 1, pp. 1–10, Feb. 1980.
[92] D. L. Trumper, M. E. Williams, and T. H. Nguyen, “Magnet arrays for synchronous machines,” in *Conference Record of the 1993 IEEE Industry Applications Conference Twenty-Eighth IAS Annual Meeting*, 1993, pp. 9–18 vol.1.
[93] Z. P. Xia, Z. Q. Zhu, and D. Howe, “Analytical magnetic field analysis of Halbach magnetized permanent-magnet machines,” *IEEE Trans. Magn.*, vol. 40, no. 4, pp. 1864–1872, Jul. 2004.
[94] E. P. Furlani, *Permanent magnet and electromechnaical devices materials, analysis, and applications*. San Diego: Academic Press, 2001.
[95] O. D. Jefimenko, *Electricity and Magnetism: An Introduction to the Theory of Electric and Magnetic Fields*, 2nd ed. Electret Scientific, 1989.
[96] H. L. Rakotoarison, J. -. Yonnet, and B. Delinchant, “Using Coulombian Approach for Modeling Scalar Potential and Magnetic Field of a Permanent Magnet With Radial Polarization,” *IEEE Trans. Magn.*, vol. 43, no. 4, pp. 1261–1264, Apr. 2007.
[97] Z. Ling, J. Ji, J. Wang, and W. Zhao, “Design Optimization and Test of a Radially Magnetized Magnetic Screw With Discretized PMs,” *IEEE Trans. Ind. Electron.*, vol. 65, no. 9, pp. 7536–7547, Sep. 2018.
[98] M. B. Kouhshahi and J. Z. Bird, “Analysis of a magnetically geared lead screw,” in *2016 IEEE Energy Conversion Congress and Exposition (ECCE)*, 2016, pp. 1–5.
[99] M. B. Kouhshahi, J. Z. Bird, A. Jannsen, J. Kadel, and W. Williams, “A Magnetically Geared Lead Screw Without Translator Skewing,” in *2018 IEEE Energy Conversion Congress and Exposition (ECCE)*, 2018, pp. 4994–4999.
[100] J. Bird and M. Bahrami Kouhshahi, “Magnetically geared lead screw,” 20180183310, 28-Jun-2018.
[101] M. Bahrami Kouhshahi, J. Bird, J. Kadel, and W. Williams, “Designing and experimentally testing a magnetically geared lead screw,” *IEEE Trans. Ind. Appl.*, (Submitted).
[102] M. Bahrami Kouhshahi, V. M. Acharya, M. Calvin, J. Z. Bird, and W. Williams, “Designing and Experimentally Testing of a Flux Focusing Axial Magnetic Gear for an Ocean Generator Application,” *Submitt. IET Electr. Power Appl.*, 2018.
[103] M. Bahrami Kouhshahi *et al.*, “An Axial Flux-Focusing Magnetically Geared Motor,” *Submitt. IEEE Trans. Ind. Appl.*, 2018.
[104] M. Bahrami Kouhshahi and J. Bird, “Calculating the Force Density Limit of a Linear Magnetic Couplings,” in *LDIA2019*, (Submitted), 2019.
[105] M. Bahrami Kouhshahi and J. Bird, “Using a Magnetic Charge Fourier Series to Studying the Force Density of Magnetic Lead Screws,” in *COMPUMAG2019*, (Submitted), 2019.